Title

High-Resolution NMR of Quadrupolar Nuclei in the Solid State

Author

Gann, Sheryl L

Publication Date

1995-11-01

LBL-38346

ERNEST ORLANDO LAWRENCE
BERKELEY NATIONAL LABORATORY

High-Resolution NMR of Quadrupolar Nuclei in the Solid State

Sheryl L. Gann

Materials Sciences Division

November 1995

Ph.D. Thesis

LBL-38346

High-Resolution NMR of Quadrupolar Nuclei in the Solid State

Sheryl Lee Gann
Ph.D. Thesis

Department of Chemistry
University of California, Berkeley

and

Materials Sciences Division
Ernest Orlando Lawrence Berkeley National Laboratory
University of California
Berkeley, CA 94720

November 1995

This work was supported by the Director, Office of Energy Research, Office of Basic Energy Sciences, Materials Sciences Division, of the U.S. Department of Energy under Contract No. DE-AC03-76SF00098.

High-Resolution NMR of Quadrupolar Nuclei in the Solid State

by

Sheryl Lee Gann

B.S. (University of Nevada, Reno) 1990

A dissertation submitted in partial satisfaction of the
requirements for the degree of
DOCTOR OF PHILOSOPHY
in
CHEMISTRY
in the
GRADUATE DIVISION
of the
UNIVERSITY of CALIFORNIA, BERKELEY

Committee in Charge:
Professor Alexander Pines, Chair
Professor Jefferey A. Reimer
Professor David E. Wemmer

DISCLAIMER

High-Resolution NMR of Quadrupolar Nuclei in the Solid State

by

Sheryl Lee Gann

Abstract

High-Resolution NMR of Quadrupolar Nuclei in the Solid State

by

Sheryl Lee Gann

Doctor of Philosophy in Chemistry

University of California at Berkeley

Professor Alexander Pines, Chair

This dissertation describes recent developments in solid state nuclear magnetic resonance (NMR), for the most part involving the use of dynamic-angle spinning (DAS) NMR to study quadrupolar nuclei. Chapter 1 introduces some of the basic concepts and theory that will be referred to in later chapters, such as the density operator, product operators, rotations, coherence transfer pathways, phase cycling, and the various nuclear spin interactions, including the quadrupolar interaction. Chapter 2 describes the theory behind motional averaging experiments, including DAS, which is a technique where a sample is spun sequentially about two axis oriented at different angles with respect to the external magnetic field such that the chemical shift and quadrupolar anisotropy are averaged to zero. Work done on various rubidium-87 salts is presented as a demonstration of DAS. Chapter 3 explains how to remove sidebands from DAS and magic-angle spinning (MAS) experiments, which result from the time-dependence of the Hamiltonian under sample spinning conditions, using rotor-synchronized π-pulses. Data from these experiments, known as DAH-180 and MAH-180, respectively, are presented for both rubidium and lead salts. In

addition, the applicability of this technique to double rotation (DOR) experiments is discussed. Chapter 4 concerns the addition of cross-polarization to DAS (CPDAS). The theory behind spin locking and cross polarizing quadrupolar nuclei is explained and a method of avoiding the resulting problems by performing cross polarization at 0° (parallel) with respect to the magnetic field is presented. Experimental results are shown for a sodium-23 compound, sodium pyruvate, and for oxygen-17 labeled L-alanine. In Chapter 5, a method for broadening the Hartmann-Hahn matching condition under MAS, called variable effective field cross-polarization (VEFCP), is presented, along with experimental work on adamantane and polycarbonate.

Table of Contents

List of Figures

List of Tables

Acknowledgements

There are many people who deserve thanks for helping me through graduate school. In particular, I would like to thank Wrenn Wooten, Jay Baltisberger, Phil Grandinetti, Margaret Eastman, Jay Shore, Susan De Paul, and of course Alex, Dione, and the rest of the Pinenuts.

Chapter 1
Introduction

Nuclear magnetic resonance (NMR) is a highly useful spectroscopic technique that has proved essential in the determination of structure and dynamics of many diverse classes of compounds. This thesis will focus primarily on the application of NMR to quadrupolar nuclei in the solid state, and in particular, using the technique of dynamic-angle spinning (DAS) NMR. This introductory chapter will begin by introducing concepts and theories that will be referred to in later chapters. The reader interested in a more detailed theoretical treatments is referred to any number of texts on NMR [1-5].

1.1 The Density Operator

It is quite useful to describe nuclear spin dynamics in terms of the density operator, defined as follows. If, for a given ensemble, all spin systems are in the same state (a pure state), described by the normalized state function $|\psi(t)\rangle$ in an orthonormal basis $\{|r\rangle\}$ with coefficients $c_r(t)$, then the density operator $\rho(t)$ is defined by

$$\rho(t) = |\psi(t)\rangle\langle\psi(t)| = \sum_r \sum_s c_r(t) c_s^*(t) |r\rangle\langle s| . \tag{1.1}$$

If, on the other hand, all spin systems in the ensemble are not in the same state (a mixed state), the density operator is given by the ensemble average (denoted by the bar) as

$$\rho(t) = |\psi(t)\rangle\langle\psi(t)| = \sum_r \sum_s \overline{c_r(t) c_s^*(t)} |r\rangle\langle s| . \tag{1.2}$$

The equation of motion of the density operator can be derived from the Schrödinger equation with Hamiltonian $H(t)$,

$$\frac{d}{dt}|\psi(t)\rangle = -iH(t)|\psi(t)\rangle . \tag{1.3}$$

Using this equation we can derive the Liouville-von Neumann equation,

$$\frac{d}{dt}\rho(t) = -i[H(t),\rho(t)]. \tag{1.4}$$

The solution to this differential equation is

$$\rho(t) = U(t)\rho(0)U(t)^{-1};\ U(t) = T\exp\left(-i\int_0^t H(t')dt'\right) \tag{1.5}$$

where T is the Dyson time-ordering operator. By a suitable transformation into a different reference frame, the Hamiltonian can often be made to be time independent and the evolution of density matrix can then be calculated quite simply as

$$\rho(t) = \exp(-iHt)\rho(0)\exp(iHt). \tag{1.6}$$

The expectation values of an observable can be expressed in terms of the density operator as follows. For an operator O, the expectation value $\langle O\rangle$ is

$$\overline{\langle\psi(t)|O|\psi(t)\rangle} \tag{1.7}$$

where again the bar indicates an ensemble average. Expanding the wave function in terms of its orthonormal base we can express $\langle O\rangle$ as

$$\langle O\rangle = \sum_r\sum_s \overline{c_r^*(t)c_s(t)}\langle r|O|s\rangle = \sum_r\sum_s \langle s|\rho(t)|r\rangle\langle r|O|s\rangle = \mathrm{Tr}\{O\rho(t)\}. \tag{1.8}$$

The function Tr indicates a trace defined by

$$\mathrm{Tr}\{O\} = \sum_r \langle r|O|r\rangle . \tag{1.9}$$

The density operator $\rho(t)$ as defined depends on both spin and space variables of the entire quantum mechanical system. However, it is usually correct to reduce the number of variable in the system and use only a limited set of opera-

tors $\{Q\}$ that act on the spin states of the system, grouping the remaining degrees of freedom together and designating them as the lattice. In such a situation, the density operator is redefined as the reduced spin density operator

$$\sigma(t) = \mathrm{Tr}_{lattice}\{\rho(t)\} \tag{1.10}$$

where $\mathrm{Tr}_{lattice}$ refers to a partial trace over the lattice variables. The expectation value of the operator Q is given by

$$\langle Q \rangle = \mathrm{Tr}_{spin}\{Q\sigma(t)\} \tag{1.11}$$

and the equation of motion from eqn (1.4) is now

$$\frac{d}{dt}\sigma(t) = -i\left[H_{spin}, \sigma(t)\right] - \hat{\hat{\Gamma}}\left[\sigma(t) - \sigma_0\right]. \tag{1.12}$$

The Hamiltonian, H_{spin}, acts on the spin variables and is obtained from the full Hamiltonian by averaging over the lattice coordinates

$$H_{spin} = \sum_{lattice} \mathrm{Tr}_{lattice}\{H\}. \tag{1.13}$$

$\hat{\hat{\Gamma}}$ is the relaxation superoperator and accounts for effects of the lattice on the spin system, driving it to its equilibrium value of σ_0. Assuming that the external magnetic field defines the z-axis of the laboratory reference frame, the equilibrium density matrix, σ_0, can be shown to be given by

$$\sigma_0 = I_z. \tag{1.14}$$

Note that σ_0 is not necessarily equivalent to $\sigma(0)$. In this text, the relaxation superoperator and its effects are generally ignored except when otherwise indicated. This greatly simplifies solving eqn (1.12), resulting in a solution analogous to that seen in eqn (1.5).

$$\sigma(t) = U(t)\sigma(0)U(t)^{-1};\ U(t) = T\exp\left(-i\int_0^t H_{spin}(t')dt'\right). \tag{1.15}$$

It is often convenient to expand the density operator in terms of a set of base operators $\{B_s\}$. If the dimension of the Hilbert space defined by the base

functions is n, then the corresponding Liouville space is spanned by n^2 independent operators, and the density operator can thus be defined

$$\sigma(t) = \sum_{i=1}^{n^2} b_i(t) B_i \,. \tag{1.16}$$

The choice of a basis operator set depends on the particular problem being studied. Three different sets used in this thesis; the first is based on the angular momentum operators. For a spin $I = 1/2$, the operators are I_x, I_y, and I_z. For a system contain N spins, the operators can be calculated from

$$B_i = 2^{n-1} \prod_{j=1}^{N} I_{j\alpha}^{c_{ji}} \,, \tag{1.17}$$

where j identifies the j^{th} spin, α is x, y, or z, and c_{ji} is a coefficient which is one for n of the spins and zero for the remaining $N-n$ spins. In this text, in which the spin systems are assumed to be one-spin systems, the basis set would then be $\{E_0, I_x, I_y, I_z\}$, with E_0 being the identity operator. From this set, a second set of operators known as spherical operators can be defined consisting of $\{E_0, I_0, I_+, I_-\}$. These operator are defined as

$$I_0 = I_z \tag{1.18}$$

and

$$I_\pm = \pm \frac{1}{\sqrt{2}} \left(I_x \pm i I_y \right). \tag{1.19}$$

A third set of base operators used in this text is comprised of what are known as fictitious spin-1/2 operators [6-8]. These operators describe a spin with $I > 1/2$ but behave for the most part like the spin-1/2 operators given above. This set can be defined by

$$I_z^{rs} = \frac{1}{2} \left(|r\rangle\langle r| - |s\rangle\langle s| \right), \tag{1.20}$$

$$I_x^{rs} = \frac{1}{2}\left(|r\rangle\langle s| + |s\rangle\langle r|\right), \tag{1.21}$$

and

$$I_y^{rs} = \frac{i}{2}\left(-|r\rangle\langle s| + |s\rangle\langle r|\right). \tag{1.22}$$

The commutation rules within a *rs* sub-manifold and between different sub-manifolds are given in Appendix A.1. This set will prove particularly useful when studying CPDAS in Chapter 4.

1.2 Rotations

This section will explain the fundamentals of rotations as pertaining to NMR. More detailed explanations can be found in references such as [9-11]. First, we will define the Euler angles which describe the relationship of one reference frame to another. In other words, the Euler angles define what rotations are needed to transform from the first frame to the second. For example, we usually want to know the relationship of the principal axis system (PAS) of a nuclear spin interaction tensor to that of the laboratory,

$$\text{Principal Axis System} \xrightarrow{(\alpha,\beta,\gamma)} \text{Laboratory}.$$

In the case of a sample spinning experiment such as magic-angle spinning (MAS), where the sample is spun at a frequency ω_r about an axis oriented at an angle θ with respect to the external magnetic field, we want to transform from the PAS to the reference frame of the rotor and then to the laboratory frame of reference,

$$\text{Principal Axis System} \xrightarrow{(\alpha,\beta,\gamma)} \text{Rotor} \xrightarrow{(\omega_r t,\theta,0)} \text{Laboratory}.$$

Fig. 1.1 shows how the Euler angles, α, β, and γ, define the necessary rotations to transform a frame of reference, *S*, with axes *X*, *Y*, and *Z*, to that of reference frame *S'''* with axis *x*, *y*, and *z*.

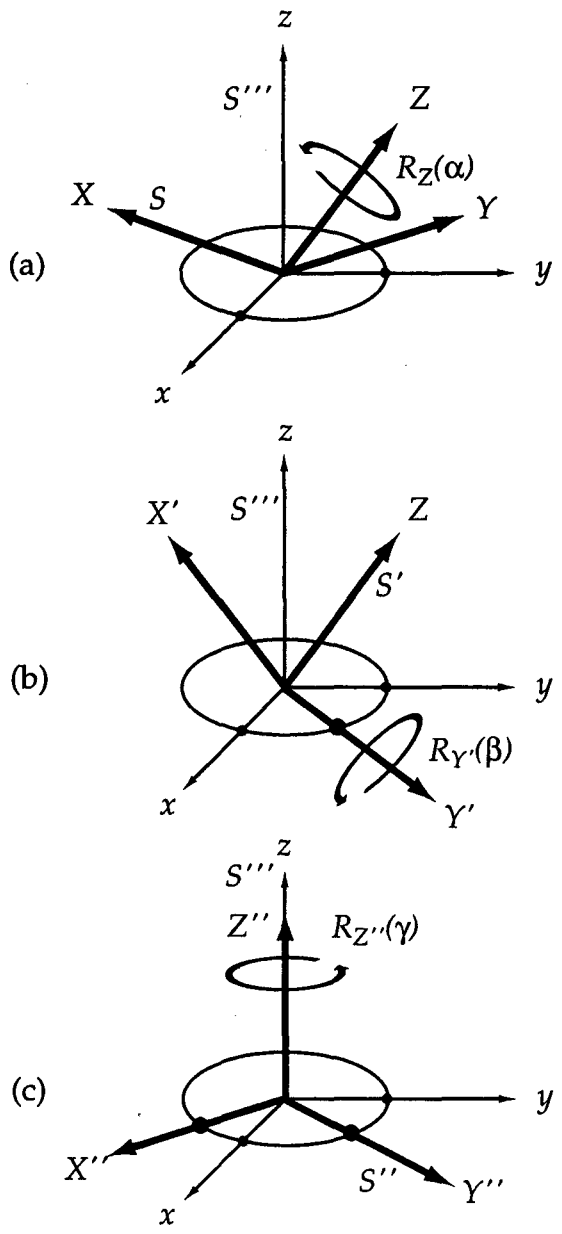

Figure 1.1 The Euler angles (α, β, γ) are the set of angles which bring the reference frame S (the PAS frame) with axes X, Y, and Z into coincidence with the reference frame S''' (the laboratory frame) with the axes x, y, and z. (a) A rotation $R_Z(\alpha)$ about Z by the angle α puts the Y axis into the xy plane. (b) A rotation $R_{Y'}(\beta)$ about the original Y axis now designated the Y' axis puts the X' (originally the X axis) into the xy plane. (c) Finally, a rotation $R_{Z''}(\gamma)$ about the Z'' axis (originally the Z axis and now coincident with the z axis) results in X'' being parallel to x, and Y'' being parallel to z.

Mathematically, we can express the rotation of tensor T of rank l, T_l, by the Euler angles α, β, and γ as

$$\hat{T}_{lm} = \sum_{m'=-l}^{l} D^{(l)}_{m'm}(\alpha,\beta,\gamma)T_{lm'}, \tag{1.23}$$

where $D^{(l)}_{nm}(\alpha,\beta,\gamma)$ is a Wigner rotation matrix element of rank l which is defined as

$$D^{(l)}_{mn}(\alpha,\beta,\gamma) = e^{-im\alpha} d^{(l)}_{mn}(\beta) e^{-in\gamma}. \tag{1.24}$$

The term $d^{(l)}_{mn}(\beta)$ is known as a reduced Wigner rotation matrix element of rank l. The reduced rotation matrix elements of rank $l = 2$ can be found in the Appendix A.2 in Table A.2 along with a method of calculating matrix elements of other ranks. Other methods of calculating reduced matrix elements can be found in the references given above and other text on angular momentum.

One important property of the Wigner rotation matrices is

$$D^{(l)}_{00}(\alpha,\beta,\gamma) = d^{(l)}_{00}(\beta) = P_l(\cos\beta), \tag{1.25}$$

where $P_l(\cos\theta)$ is the l^{th} order Legendre polynomial of $\cos\theta$. Of particular interest are the Legendre polynomials of rank $l = 2$ and $l = 4$ which are given by,

$$P_2(\cos\theta) = \frac{1}{2}\left(3\cos^2\theta - 1\right) \tag{1.26}$$

and

$$P_4(\cos\theta) = \frac{1}{8}\left(35\cos^4\theta - 30\cos^2\theta + 3\right). \tag{1.27}$$

These polynomials will prove important in the explanation of magic-angle and dynamic-angle spinning in Chapter 2.

1.3 Coherence Transfer Pathways

The concept of coherence transfer pathways is highly useful in the design of phase cycles and in the general understanding of the fate of the various orders

of coherences through the course of a NMR experiment [12,13]. The following description uses the terminology given by Ernst, *et al.* [**1**].

Each eigenstate $|r\rangle$ in high-field NMR has a magnetic quantum number M_r giving each coherence $|r\rangle\langle s|$ a coherence order of $p_{rs} = M_r - M_s$. During free precession p_{rs} is conserved; however rf pulses can introduce changes in coherence orders. We expand the density operator $\sigma(t)$ in the manner given in eqn (1.16) in term of operators classified by order p, where the base operator $\sigma^p(t)$ is defined by

$$\sigma^p(t) = \sum_{\substack{r,s \\ \text{restricted to} \\ p_{rs}=p}} c_{rs}(t)|r\rangle\langle s|. \tag{1.28}$$

In eqn (1.28), only those pairs of r and s are included in the sum that fulfill the condition $p_{rs} = p$. At the beginning of an NMR experiment, if the systems is in equilibrium, $p = 0$. If we observe the signal with quadrature detection, our signal is given by

$$S(t) = \mathrm{Tr}\{\sigma(t)I_+\} \tag{1.29}$$

and, as a result, only those coherence that follow a pathway such that they end with $p = -1$ will contribute to the observed signal. It is quite common to have multiple pulses in an NMR experiment, each pulse represented by a propagator U_i which describes its effects on the density matrix (eqn (1.5)). We can represent such evolution of the density matrix as

$$U_i\sigma^p\left(t_i^-\right)U_i^{-1} = \sum_j \sigma^{p_j}\left(t_i^+\right), \tag{1.30}$$

where t_- and t_+ are the times just before and after the application of the propagator. Noting that a rotation φ about the z-axis transforms the density matrix in the following manner,

$$e^{-i\varphi F_z}\sigma^p e^{i\varphi F_z} = \sigma^p e^{-ip\varphi}, \tag{1.31}$$

we can see that if the propagator U_i is shifted in phase by φ, then eqn (1.30) becomes,

$$U_i(\varphi_i)\sigma^p\left(t_i^-\right)U_i(\varphi_i)^{-1} = \sum_j \sigma^{p_j}\left(t_i^+\right)e^{-i\Delta p_i\varphi_i} \tag{1.32}$$

where

$$\Delta p_i = p_j\left(t_i^+\right) - p\left(t_i^-\right). \tag{1.33}$$

Therefore, each coherence component undergoing a coherence change from $p \to p_j$ acquires a phase

$$\sigma(\Delta p_i, \varphi_i) = \sigma(\Delta p_i, 0)e^{-i\Delta p_i\varphi_i} \tag{1.34}$$

and the overall signal of the experiment is

$$S(\varphi_i, t) = \sum_{\Delta p_i} S(\Delta p_i, \varphi_i = 0, t)e^{-i\Delta p_i\varphi_i}. \tag{1.35}$$

We can select a particular order of coherence $\Delta p'$ by summing the results of N_i experiments each with the phase of φ_i incremented such that

$$\varphi_i = \frac{k_i 2\pi}{N_i}, \quad k = 0,1,\ldots,N-1. \tag{1.36}$$

We can determine the signal through Fourier analysis [14] as

$$S(\Delta p', t) = \frac{1}{N}\sum_{k=0}^{N-1} S\left(k\frac{2\pi}{N}, t\right)e^{i\Delta p' k 2\pi/N} \tag{1.37}$$

where the only contributions to the signals are

$$\Delta p' \pm nN, \; n = 0, 1, 2,.... \tag{1.38}$$

We can obtain the weighting factor $\exp(-i\Delta p' k 2\pi/N)$ in eqn (1.37) by a variety of means; for example, by shifting the phase of the receiver by

$$\varphi_{rcvr} = -\Delta p' k 2\pi/N. \tag{1.39}$$

An example of using eqn (1.37) to calculate the selection of $\Delta p' = -2$ with a four-

step phase cycle is given in Table 1.1.

The calculation shown in Table 1.1 is tedious, especially for a multiple-pulse sequence and luckily unnecessary in order to calculate a phase cycle for the selection of a particular pathway. For a system with n pulses we can define each coherence transfer pathway as a vector

$$\mathbf{\Delta p} = \{\Delta p_1, \Delta p_2, \ldots, \Delta p_n\}. \tag{1.40}$$

Each component of the vector describes the change of coherence with each pulse, and the sum of the components is constant,

$$\sum_{i=1}^{n} \Delta p_i = -1 \tag{1.41}$$

since each pathway begins with $p = 0$ and must end with $p = -1$ to be observable. We can also define the phases of each of the n pulses as a vector

Table 1.1 Calculation of the signal of a four step phase cycle ($N = 4$) with selection of those coherence orders with a change of $\Delta p' = -2$. In the first column the notation $S(\Delta p)$ symbolizes $S(\Delta p_i, \varphi_i = 0, t)$. Columns two through four in each row represents the sum over each of the phases in the cycle (0°, 90°, 180°, 270°), with the total being multiplied by $S(\Delta p)$. The sum of each row divided by N is given in the last column. The only non-zero contributions after the phase cycle are those in the unshaded rows with $\Delta p' = -2 \pm nN$, $n = 0, 1, 2, \ldots$.

$S(\Delta p)$	$\varphi = 0$	$\varphi_i = \pi/2$	$\varphi_i = \pi$	$\varphi_i = 3\pi/2$	
$S(-3)$	$\times(1$	$+e^{+i3\pi/2}e^{-i\pi} = e^{+i\pi/2}$	$+e^{+i3\pi}e^{-i2\pi} = e^{+i\pi}$	$+e^{+i9\pi/2}e^{-i3\pi} = e^{+i3\pi/2})$	$= 0$
$+S(-2)$	$\times(1$	$+e^{+i\pi}e^{-i\pi} = e^{+i\cdot 0}$	$+e^{+i2\pi}e^{-i2\pi} = e^{+i\cdot 0}$	$+e^{+i3\pi}e^{-i3\pi} = e^{+i\cdot 0})$	$= 1$
$+S(-1)$	$\times(1$	$+e^{+i\pi/2}e^{-i\pi} = e^{-i\pi/2}$	$+e^{+i\pi}e^{-i2\pi} = e^{-i\pi}$	$+e^{+i3\pi/2}e^{-i3\pi} = e^{-i3\pi/2})$	$= 0$
$+S(0)$	$\times(1$	$+e^{+i\cdot 0}e^{-i\pi} = e^{-i\pi}$	$+e^{+i\cdot 0}e^{-i2\pi} = e^{-i2\pi}$	$+e^{+i\cdot 0}e^{-i3\pi} = e^{-i3\pi})$	$= 0$
$+S(+1)$	$\times(1$	$+e^{-i\pi/2}e^{-i\pi} = e^{-i3\pi/2}$	$+e^{-i\pi}e^{-i2\pi} = e^{-i3\pi}$	$+e^{-i3\pi/2}e^{-i3\pi} = e^{-i9\pi/2})$	$= 0$
$+S(+2)$	$\times(1$	$+e^{-i\pi}e^{-i\pi} = e^{-i2\pi}$	$+e^{-i2\pi}e^{-i2\pi} = e^{-i4\pi}$	$+e^{-i3\pi}e^{-i3\pi} = e^{-i6\pi})$	$= 1$
$+S(+3)$	$\times(1$	$+e^{-i3\pi/2}e^{-i\pi} = e^{-i5\pi/2}$	$+e^{-i3\pi}e^{-i2\pi} = e^{-i5\pi}$	$+e^{-i9\pi/2}e^{-i3\pi} = e^{-i15\pi/2})$	$= 0$

$$\boldsymbol{\varphi} = \{\varphi_1, \varphi_2, \ldots, \varphi_n\}. \tag{1.42}$$

In analogy to eqn (1.39), we can shift the phase of the receiver by

$$\varphi_{rcvr} = -\Delta\mathbf{p} \cdot \boldsymbol{\varphi} = -\sum_i \Delta p_i \varphi_i \tag{1.43}$$

to achieve the desired selection process.

As an example of using eqn (1.43) to calculate a phase cycle, consider the pulse sequence in Fig. 1.2. The pathway we wish to select is represented by $\Delta\mathbf{p}$ = {-1, +1, +1, -2}. Inserting the components of the vector into eqn (1.43) yields

$$\varphi_{rcvr} = \varphi_1 - \varphi_2 - \varphi_3 + 2\varphi_4. \tag{1.44}$$

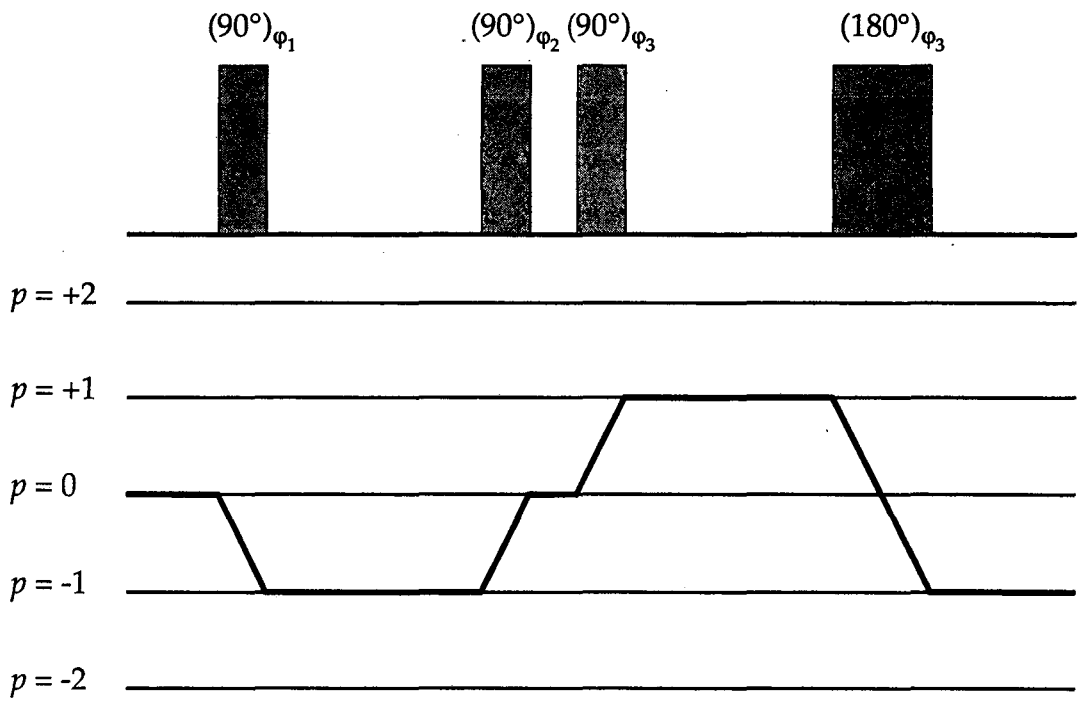

Figure 1.2 A typical coherence transfer path where the path $p = 0 \rightarrow -1 \rightarrow 0 \rightarrow +1 \rightarrow -1$, represented by the vector $\Delta\mathbf{p}$ = {-1, +1, +1, -2} is being selected. During free precession the order of coherence is preserved, while the application of pulses induce changes in the coherence order. Since this is assumed to be a one-spin system, rf pulses generate changes of coherence between the orders $p = 0$ and $p = \pm 1$.

Table 1.2 Phase cycle for selecting the pathway given in Fig. 1.2 described by the vector $\Delta \mathbf{p} = \{-1, +1, +1, -2\}$.

φ_1	φ_2	φ_3	φ_4	φ_{rcvr}	φ_1	φ_2	φ_3	φ_4	φ_{rcvr}
0°	0°	0°	0°	0°	0°	180°	0°	0°	180°
90°	0°	0°	0°	90°	90°	180°	0°	0°	270°
180°	0°	0°	0°	180°	180°	180°	0°	0°	0°
270°	0°	0°	0°	270°	270°	180°	0°	0°	90°
0°	0°	90°	0°	270°	0°	180°	90°	0°	90°
90°	0°	90°	0°	0°	90°	180°	90°	0°	180°
180°	0°	90°	0°	90°	180°	180°	90°	0°	270°
270°	0°	90°	0°	180°	270°	180°	90°	0°	0°
0°	0°	180°	0°	180°	0°	180°	180°	0°	0°
90°	0°	180°	0°	270°	90°	180°	180°	0°	90°
180°	0°	180°	0°	0°	180°	180°	180°	0°	180°
270°	0°	180°	0°	90°	270°	180°	180°	0°	270°
0°	0°	270°	0°	90°	0°	180°	270°	0°	270°
90°	0°	270°	0°	180°	90°	180°	270°	0°	0°
180°	0°	270°	0°	270°	180°	180°	270°	0°	90°
270°	0°	270°	0°	0°	270°	180°	270°	0°	180°

We can simplify phase cycles by realizing that is not necessary to phase cycle every pulse. For example, it is not necessary to phase cycle the final pulse since only the coherence $p = -1$ can be observed. The second pulse only needs to be phase cycled by 180° to select the $\Delta p = +1$ and exclude the $\Delta p = 0$ and $\Delta p = +2$ pathways, since, assuming a one-spin system, rotations are generated in the subspace defined by the operators I_z, I_+, and I_-, which have coherence orders of 0, +1, and –1, respectively; other values of p do not exist. The resulting phase cycle is 32 steps long and is given in Table 1.2.

1.4 Nuclear Spin Hamiltonians

A variety of spin interactions influence magnetic resonance and for detailed theoretical background the reader is referred to the many excellent books on magnetic resonance [1-5], angular momentum [9-11], and quantum mechanics [15-17]. Of the spin interactions discussed here, the Zeeman, electric quadrupole, chemical shift, dipolar, and rf interactions, only the electric quadrupole interac-

tion will be discussed in any detail as this thesis is primarily concerned with quadrupolar nuclei.

Static Perturbation Theory

In the following discussions, static perturbation theory is used to calculate the effects of the various nuclear spin Hamiltonians. Static perturbation theory is described in detail in any number of quantum mechanics text books and only the results will be given here. Perturbation theory is useful when we have a Hamiltonian that can be expressed as

$$H = H_0 + H_p \tag{1.45}$$

where $H_p \ll H_0$. The eigenvalues and eigenstates of H_0 are ε_n and $|n\rangle$, respectively, such that

$$H_0|n\rangle = \varepsilon_n|n\rangle . \tag{1.46}$$

We can expand the Hamiltonian H as

$$H = \sum_n \left(\varepsilon_n + E^{(1)} + E^{(2)} + \cdots\right)|n\rangle\langle n| \tag{1.47}$$

where $E^{(k)}$ are a series of correction terms to the eigenvalue ε_n. Only two of are of interest here, the first-order correction

$$E^{(1)} = \langle n|H_p|n\rangle \tag{1.48}$$

and the second-order correction

$$E^{(2)} = \sum_{m \neq n} \frac{\langle n|H_p|m\rangle\langle m|H_p|n\rangle}{\varepsilon_n - \varepsilon_m} . \tag{1.49}$$

Terms with $k > 2$ are assumed to be small enough to ignore. Only the secular part of H_p (the part that commutes with H_0) contributes to eqn (1.48), while only the nonsecular part of H_p contributes in eqn (1.49).

The Zeeman Interaction

In high-field NMR, the strongest spin interaction present is almost always the Zeeman interaction, the interaction of a magnetic dipole (the nucleus) with a magnetic field. The Zeeman Hamiltonian is given by

$$H_z = -\hbar\gamma B_0 I_z = -\hbar\omega_0 I_z, \tag{1.50}$$

where B_0 is the magnetic field, the direction of which defines the z-axis of the laboratory frame, and ω_0 is the Larmor frequency. Since this is the strongest interaction present, its eigenvectors and eigenvalues will be used as the basis set when using static perturbation theory to calculate the effects of other interactions. The Zeeman spin operator set in spherical operators (eqns (1.18) and (1.19)) is

$$I_0 = I_z \tag{1.51}$$

and

$$I_{\pm 1} = \pm\frac{\left(I_x \pm iI_y\right)}{\sqrt{2}}. \tag{1.52}$$

The matrix elements of this set are

$$\langle I\ m|I_z|I\ m\rangle = m \tag{1.53}$$

and

$$\langle I\ m|I_{\pm 1}|I\ m\pm 1\rangle = \mp\frac{1}{\sqrt{2}}\sqrt{(I\mp m)(I\pm m+1)}. \tag{1.54}$$

The Electric Quadrupole Interaction

When dealing with a nucleus with an angular momentum of greater than 1/2, the electrical interaction of the nucleus with its surrounding becomes important. For a spin-1/2 nucleus, the nuclear charge distribution is spherical and therefore reorientation of the nucleus has no effect on its energy. For a quad-

rupolar nucleus, this is not the case. Consider a nucleus with a charge distribution density $\varrho(\vec{r})$ interacting with a electric field potential $V(\vec{r})$. The classical interaction energy E_Q would then be

$$E_Q = \int_{Volume} \varrho(\vec{r}) V(\vec{r}) d^3\vec{r} \tag{1.55}$$

integrated over the volume of the nucleus. The electric field potential $V(\vec{r})$ depends upon the spatial orientation of all the electric charges which originate from the nuclei and electrons of the system of interest. Since a true analytical expression would be virtually impossible to obtain, the potential can be expressed as a Taylor series about the center of mass of the nucleus:

$$V(\vec{r}) = V(0) + \sum_{\alpha=x,y,z} \alpha \frac{\partial V}{\partial \alpha}\bigg|_{r=0} + \frac{1}{2!} \sum_{\substack{\alpha=x,y,z \\ \beta=x,y,z}} \alpha\beta \frac{\partial^2 V}{\partial\alpha\partial\beta}\bigg|_{r=0} + \cdots. \tag{1.56}$$

Substituting eqn (1.56) into eqn (1.55) yields

$$E_Q = ZeV(0) + \sum_{\alpha=x,y,z} P_\alpha \frac{\partial V}{\partial \alpha}\bigg|_{r=0} + \frac{1}{2!} \sum_{\substack{\alpha=x,y,z \\ \beta=x,y,z}} Q'_{\alpha\beta} \frac{\partial^2 V}{\partial\alpha\partial\beta}\bigg|_{r=0} + \cdots \tag{1.57}$$

In eqn (1.57) the total charge density of a nucleus with atomic number Z is Ze, the α component of the electric dipole moment P is

$$P_\alpha = \int_{Volume} \alpha \varrho(\vec{r}) d^3\vec{r}\,, \tag{1.58}$$

and the $\alpha\beta$ component of the electric quadrupole moment $Q'_{\alpha\beta}$ is

$$Q'_{\alpha\beta} = \int_{Volume} \alpha\beta \varrho(\vec{r}) d^3\vec{r}\,. \tag{1.59}$$

The term of interest here is the third term of eqn (1.57); the first term is a constant and independent of the orientation of the nucleus and the second term vanishes because the center of charge and the center of mass of the nucleus are assumed to coincide [2,18]. Higher order terms are assumed to be insignificant.

To simplify notation, the elements of the electric field gradient tensor are

defined as

$$V_{\alpha\beta} \equiv \left.\frac{\partial^2 V}{\partial\alpha\partial\beta}\right|_{r=0} \tag{1.60}$$

By an appropriate choice of a reference frame, designated the principal axis system (PAS) of the electric field gradient (EFG) and labeled by X, Y, and Z, the tensor in eqn (1.60) will contain only three diagonal components V_{XX}, V_{YY}, and V_{ZZ}, which are defined to fulfill the relationship,

$$|V_{ZZ}| \geq |V_{YY}| \geq |V_{XX}|. \tag{1.61}$$

The three components of the EFG in the PAS are used to define two other parameters, the field gradient of the EFG, eq,

$$eq = V_{ZZ}, \tag{1.62}$$

and the asymmetry parameter η_Q

$$\eta_Q = \frac{V_{XX} - V_{YY}}{V_{ZZ}}, \tag{1.63}$$

which describes the symmetry of the EFG. If the field gradient possesses cylindrical symmetry, then η_Q is equal to zero. As the symmetry deviates from cylindrical the value of η_Q increases to its maximum value of one. If $V_{XX} = V_{YY} = V_{ZZ}$, then the quadrupolar interaction vanishes.

To simplify further calculations, the following traceless tensor is introduced.

$$Q_{\alpha\beta} = \left(3Q'_{\alpha\beta} - \delta_{\alpha\beta}\sum_{i=x,y,z} Q'_{ii}\right) = \int_{Volume} \varrho(\vec{r})\left(3x_\alpha x_b - \delta_{\alpha\beta} r^2\right) d^3\vec{r} \tag{1.64}$$

By substituting eqn (1.64) into eqn (1.57) and taking note of Laplace's equation,

$$\nabla^2 V = V_{XX} + V_{YY} + V_{ZZ} = 0, \tag{1.65}$$

the quadrupolar interaction energy can be written as

$$E_Q = \frac{1}{6} \sum_{\alpha,\beta=x,y,z} Q_{\alpha\beta} V_{\alpha\beta} \,. \tag{1.66}$$

We must now discuss the quantum mechanical derivation of the quadrupolar Hamiltonian. The quantum mechanical equivalent of the charge density $\varrho(\vec{r})$ is the operator $\rho(\vec{r})$ defined by

$$\rho(\vec{r}) = \sum_i q_i \delta(\vec{r} - \vec{r}_i) \tag{1.67}$$

The vector $\vec{r}_i$ gives the position of the i^{th} nucleon in the nucleus with charge q_i. The quadrupole tensor operator $Q_{\alpha\beta}$ can be obtained by substituting eqn (1.67) into equation eqn (1.64) yielding

$$Q_{\alpha\beta} = \sum_i e\left(3\alpha_i\beta_i - \delta_{\alpha\beta} r_i^2\right). \tag{1.68}$$

The quantum mechanical Hamiltonian is then

$$H_Q = \frac{1}{6} \sum_{\alpha,\beta} Q_{\alpha\beta} V_{\alpha\beta} \tag{1.69}$$

The components of the electric field gradient $V_{\alpha\beta}$ represent expectation values of an EFG tensor operator.

We can express the above operators in terms of irreducible second-rank spherical tensors T^Q_{2m} and R^Q_{2m} where the five components of T^Q_{2m} are

$$T^Q_{20} = \frac{e}{2\sqrt{6}} \sum_j \left(3z_j^2 - r_j^2\right), \tag{1.70}$$

$$T^Q_{2\pm1} = \mp \frac{e}{2} \sum_j z_j \left(x_j \pm i y_j\right), \tag{1.71}$$

and

$$T^Q_{2\pm2} = \frac{e}{4} \sum_j \left(x_j \pm i y_j\right). \tag{1.72}$$

The five components of R^Q_{2m} are

$$R^Q_{20} = \sqrt{\frac{3}{2}} V_{zz}, \tag{1.73}$$

$$R^{Q}_{2\pm1} = \mp\left(V_{xz} - iV_{yz}\right), \tag{1.74}$$

and

$$R^{Q}_{2\pm2} = \frac{1}{2}\left(V_{xx} - V_{zz} \pm 2iV_{xy}\right). \tag{1.75}$$

The quantum mechanical Hamiltonian can be expressed in term of these irreducible spherical tensors as

$$H_Q = \sum_{m=-2}^{2}(-1)^m T^{Q}_{2m} R^{Q}_{2-m}\,. \tag{1.76}$$

We can now take advantage of the Wigner-Eckert theorem [10,11,15]. This theorem essentially states that all irreducible tensors of a given rank are proportional to one another. For a set of wave functions with quantum numbers J, M, α, J', M', and α', where α can represent a set of quantum numbers describing the system, the theorem can be expressed as

$$\langle \alpha JM|T_{lm}|\alpha' J'M'\rangle = \langle l\, m,\, J'\, M'|J\, M\rangle \langle \alpha J\|T_l\|\alpha' J'\rangle\,. \tag{1.77}$$

The quantity $\langle l\, m,\, J'\, M'|J\, M\rangle$ is a Clebsch-Gordon coefficient and contains the geometric information about the system. A discussion of Clebsch-Gordon coefficients and their properties can be found in texts on angular momentum and quantum mechanics such as reference [11]. The quantity $\langle \alpha\, J\|T_l\|\alpha'\, J'\rangle$ is called the reduced matrix element of T_l and is a constant which depends only upon α, J, α', J', and l. Therefore, it is independent of reorientation, depending only upon the physical properties of the system. By using the Wigner-Eckert theorem, we can relate T_{lm}'s that are a function of different variables:

$$\langle \alpha\, J\, M|T_{lm}(r)|\alpha'\, J'\, M'\rangle = \langle \alpha\, J\, M|T_{lm}(s)|\alpha'\, J'\, M'\rangle \frac{\langle \alpha\, J\|T_l(r)\|\alpha'\, J'\rangle}{\langle \alpha\, J\|T_l(s)\|\alpha'\, J'\rangle}. \tag{1.78}$$

The Clebsch-Gordon coefficient is eliminated since the values l, m, J, M, J', and M' are the same for both tensors. The reduced matrix elements depend upon the operator in question and form the proportionality constant describing the rela-

tionship between the two sets of tensors.

Using eqn (1.78) we can now show that

$$\left\langle \alpha I m \middle| Q_{\alpha\beta} \middle| \alpha I m' \right\rangle = \left\langle \alpha I m \middle| \frac{3}{2}\left(I_\alpha I_\beta + I_\beta I_\alpha\right) - \delta_{\alpha\beta} I^2 \middle| \alpha I m' \right\rangle C. \tag{1.79}$$

The value C is a constant and can be calculated by evaluating eqn (1.79) using the values $m = m' = I$ and $\alpha = \beta = z$.

$$\left\langle \alpha II \middle| \sum_i 3z_i^2 - r_i^2 \middle| \alpha II \right\rangle = \left\langle \alpha II \middle| 3I_z^2 - I^2 \middle| \alpha II \right\rangle C \tag{1.80}$$

We define the nuclear constant eQ, the quadrupolar moment, as the matrix element

$$eQ \equiv \left\langle II\alpha \middle| Q_{zz} \middle| II\alpha \right\rangle. \tag{1.81}$$

Equation (1.80) then becomes

$$eQ = CI(2I-1), \tag{1.82}$$

and, therefore, the constant C is then

$$C = \frac{eQ}{I(2I-1)}. \tag{1.83}$$

Two other constants are typically defined: the quadrupolar frequency ω_Q,

$$\omega_Q \equiv \frac{e^2 qQ}{2I(2I-1)\hbar}, \tag{1.84}$$

and the quadrupolar coupling constant, C_Q,

$$C_Q \equiv \frac{e^2 qQ}{h}. \tag{1.85}$$

The quadrupolar Hamiltonian in eqn (1.76) can now be written as

$$H_Q = \hbar\omega_Q \sum_{m=-2}^{2} (-1)^m A_{2-m}^Q T_{2m}^Q \tag{1.86}$$

where the components of T_{2m}^Q can now be expressed as

$$T_{20}^{Q} = \frac{1}{\sqrt{6}}\left(3I_z^2 - I^2\right), \tag{1.87}$$

$$T_{2\pm1}^{Q} = \frac{1}{\sqrt{2}}\left(I_z I_{\pm1} + I_{\pm1} I_z\right), \tag{1.88}$$

and

$$T_{2\pm2}^{Q} = I_{\pm1}^2. \tag{1.89}$$

The tensor A_{2m}^{Q} corresponds to the tensor R_{2m}^{Q} with components given in eqn (1.73) to eqn (1.75) but redefined, such that

$$A_{2m}^{Q} = \sum_{m'=-2}^{2} D_{m'm}^{(2)}(\alpha,\beta,\gamma)\rho_{2m'}^{Q} \tag{1.90}$$

where ρ_{2m}^{Q} are the components of the EFG in the principal axis system,

$$\rho_{20}^{Q} = \sqrt{\frac{3}{2}}, \tag{1.91}$$

$$\rho_{2\pm1}^{Q} = 0, \tag{1.92}$$

and

$$\rho_{2\pm2}^{Q} = \frac{1}{2}\frac{\left(V_{xx} - V_{yy}\right)}{V_{zz}} = \frac{1}{2}\eta_Q. \tag{1.93}$$

The angles α, β, and γ are the Euler angles which define the orientation of the PAS with respect to the laboratory frame of reference, the relationship between which is illustrated in Fig. 1.1.

Under high-field conditions the Hamiltonian in eqn (1.86) is to be a small perturbation upon the Zeeman Hamiltonian: $\omega_Q \ll \omega_0$. We can therefore use static perturbation theory as explained in eqns (1.45) through (1.49) to calculate the effects of the quadrupolar interaction on high-field NMR spectra. The first order correction is calculated using eqn (1.48),

$$E_m^{(1Q)} = \left\langle Im\middle|H_Q\middle|Im\right\rangle. \tag{1.94}$$

Since only the secular part of H_Q contributes to the first order correction we may

represent the Hamiltonian to first order as

$$H_Q = \hbar\omega_Q A_{20}^Q T_{20}^Q = \frac{\hbar\omega_Q}{\sqrt{6}} A_{20}^Q \left(3I_z^2 - I^2\right). \tag{1.95}$$

The first-order correction to the eigenvalue, $E_m^{(1Q)}$, is

$$E_m^{(1Q)} = \frac{\hbar\omega_Q}{\sqrt{6}} A_{20}^Q \left(3m^2 - I(I+1)\right). \tag{1.96}$$

We are interested in the case of half-odd integer nuclei and, in particular, the central $(1/2 \rightarrow -1/2)$ transition. We must therefore calculate the splitting in the energy levels of this transition. The splitting of a single quantum transition $(m \rightarrow m-1)$ can be calculated as

$$\Delta E_{m\rightarrow m-1}^{(1Q)} = \frac{3\hbar\omega_Q}{\sqrt{6}} A_{20}^Q (2m-1). \tag{1.97}$$

The splitting for the central transition is therefore

$$\Delta E_{1/2\rightarrow -1/2}^{(1Q)} = 0, \tag{1.98}$$

and we must calculate the second-order correction to the eigenvalue to see if it makes a significant contribution to the Hamiltonian. Using eqn (1.49), the second-order correction to the eigenvalue is

$$E_m^{(2Q)} = \sum_{n\neq m} \frac{\langle In|H_Q|Im\rangle\langle Im|H_Q|In\rangle}{\hbar\omega_0(n-m)}. \tag{1.99}$$

Inserting the Hamiltonian from eqn (1.86), we get

$$E_m^{(2Q)} = \frac{\hbar\omega_Q^2}{\omega_0} \sum_{n\neq m} \frac{\sum_{j=-2}^{2} \langle In|(-1)^j A_{2-j}^Q T_{2j}^Q|Im\rangle \sum_{j=-2}^{2} \langle Im|(-1)^j A_{2-j}^Q T_{2j}^Q|In\rangle}{(n-m)}. \tag{1.100}$$

Using eqn (1.100) and the values of the matrix elements of T_{2m}^Q (given in Appendix A.3), we can calculate $\Delta E_{1/2\rightarrow -1/2}^{(2Q)}$ as

$$\Delta E_{1/2\rightarrow -1/2}^{(2Q)} = \left(I(I+1) - 3/4\right)\frac{\hbar\omega_Q^2}{\omega_0}\left(2A_{21}^Q A_{2-1}^Q + A_{22}^Q A_{2-2}^Q\right). \tag{1.101}$$

In order to simplify this expression, we will combine the A_{2m}'s, forming new zero-, second-, and fourth-rank tensors. First, we will define the second order quadrupolar frequency, Ω_Q as

$$\Omega_Q = 2\big(I(I+1)-3/4\big)\frac{\omega_Q^2}{\omega_0}\sum_{m=1}^{2}\frac{A_{2m}^Q A_{2-m}^Q}{m}. \tag{1.102}$$

Substituting in the definition of A_{2m} found in eqn (1.90), we express the tensor product as

$$A_{2m}^Q A_{2-m}^Q = \sum_{k=-2}^{2}\sum_{k'=-2}^{2} D_{km}^{(2)}(R)\rho_{2k}^Q D_{k'-m}^{(2)}(R)\rho_{2k'}^Q, \tag{1.103}$$

where R represents the set of Euler angles α, β, and γ that describe the orientation of the EFG with respect to the laboratory reference frame. A product of two second-rank Wigner rotation matrices can be expressed as a sum of rotation matrices, yielding

$$D_{km}^{(2)}(R)D_{k'-m}^{(2)}(R) = \sum_{l=0,2,4}\big\langle 2\,m, 2-m|l\,0\big\rangle\big\langle 2\,k, 2\,k'|2\,k+k'\big\rangle D_{k+k'\,0}^{(l)}(R). \tag{1.104}$$

Defining $n = k + k'$, eqn (1.103) can be rewritten as

$$A_{2m}^Q A_{2-m}^Q = \sum_{l=0,2,4}\big\langle 2\,m, 2-m|l\,0\big\rangle\sum_{k=-2}^{2}\sum_{n=-4}^{4}\big\langle 2\,k, 2\,n-k|l\,n\big\rangle D_{n0}^{(l)}(R)\,\rho_{2k}^Q\,\rho_{2n-k}^Q. \tag{1.105}$$

We then define the tensors, a_{ln}^Q, such that

$$a_{ln}^Q = \sum_{k=-2}^{2}\big\langle 2\,k, 2\,n-k|l\,n\big\rangle\rho_{2k}^Q\rho_{2n-k}^Q. \tag{1.106}$$

The various components of a_{ln}^Q, given in Table 1.3, can be calculated by evaluating the Clebsch-Gordon coefficients and using eqns (1.91) through (1.93). Eqn (1.102) can then be expressed as

$$\Omega_Q = 2\big(I(I+1)-3/4\big)\frac{\omega_Q^2}{\omega_0}\sum_{l=0,2,4}\sum_{m=1}^{2}\left(\frac{\big\langle 2\,m, 2-m|l\,0\big\rangle}{m}\right)\sum_{n=-4}^{4}\left(D_{n0}^{(l)}(R)a_{ln}^Q\right) \tag{1.107}$$

The a_{ln}^Q's are used to define a second set of tensors, $\mathcal{A}_{l0}^Q$,

$$\mathcal{A}_{l0}^{Q} = 2\big(I(I+1)-3/4\big)\frac{\omega_Q^2}{\omega_0}\sum_{m=1}^{2}\left(\frac{\langle 2m, 2-m|l\,0\rangle}{m}\right)\sum_{n=-4}^{4}\left(D_{n0}^{(l)}(R)a_{ln}^{Q}\right). \qquad (1.108)$$

The l = 0, 2, and 4 components of $\mathcal{A}_{l0}^{Q}$ are given by

$$\mathcal{A}_{00}^{Q} = -\frac{1}{\sqrt{5}}\big(I(I+1)-3/4\big)\frac{\omega_Q^2}{\omega_0}a_{00}, \qquad (1.109)$$

$$\mathcal{A}_{20}^{Q} = 2\sqrt{\frac{2}{7}}\big(I(I+1)-3/4\big)\frac{\omega_Q^2}{\omega_0}\sum_{n=-2}^{2}D_{n0}^{(2)}(R)a_{2n}, \qquad (1.110)$$

and

$$\mathcal{A}_{40}^{Q} = \frac{9}{\sqrt{70}}\big(I(I+1)-3/4\big)\frac{\omega_Q^2}{\omega_0}\sum_{n=-4}^{4}D_{n0}^{(4)}(R)a_{4n}. \qquad (1.111)$$

Inserting eqns (1.109) through (1.111) into (1.107), the second-order quadrupolar frequency Ω_Q can then be expressed as

$$\Omega_Q = \sum_{l=0,2,4}\mathcal{A}_{l0}^{Q}. \qquad (1.112)$$

The Chemical Shift Interaction

We can express the chemical shift Hamiltonian as

Table 1.3 Values for a_{ln}^{Q} (eqn (1.106)). η_Q is the quadrupolar asymmetry parameter.

		n		
		0	±2	±4
l	0	$\frac{3}{2\sqrt{5}}\left(\frac{\eta_Q^2}{3}+1\right)$	—	—
	2	$\frac{3}{2}\sqrt{\frac{2}{7}}\left(\frac{\eta_Q^2}{3}-1\right)$	$\sqrt{\frac{3}{7}}\eta_Q$	—
	4	$\frac{9}{\sqrt{70}}\left(\frac{\eta_Q^2}{18}+1\right)$	$\frac{3}{2\sqrt{7}}\eta_Q$	$\frac{\eta_Q^2}{4}$

$$H_{CS} = \hbar\gamma \sum_{l=0,2} \sum_{m=-l}^{l} (-1)^m T_{lm}^{CS} R_{l-m}^{CS} \tag{1.113}$$

The chemical shift tensor will be indicated by δ^{CS} and in its principal axis frame (PAS) has the components δ_{XX}, δ_{YY}, and δ_{ZZ}. The trace of the chemical shift tensor is proportional to the isotropic chemical shift and is defined by

$$\delta_{iso}^{CS} = \frac{1}{3}\left(\delta_{XX}^{CS} + \delta_{YY}^{CS} + \delta_{ZZ}^{CS}\right), \tag{1.114}$$

the chemical shift anisotropy is defined by

$$\Delta\delta = \frac{3}{2}\left(\delta_{ZZ}^{CS} - \delta_{iso}^{CS}\right), \tag{1.115}$$

and the asymmetry parameter is given by

$$\eta_{CS} = \frac{\delta_{XX}^{CS} - \delta_{YY}^{CS}}{\delta_{ZZ}^{CS} - \delta_{iso}^{CS}}. \tag{1.116}$$

The components of T^{CS} are given by

$$T_{00}^{CS} = B_0 I_z, \tag{1.117}$$

$$T_{20}^{CS} = \sqrt{\frac{2}{3}} B_0 I_z \tag{1.118}$$

$$T_{2\pm1} = \frac{\sqrt{2}}{2} B_0 I_{\pm}, \tag{1.119}$$

and

$$T_{2\pm2} = 0. \tag{1.120}$$

The spatial tensor R^{CS} is related to the spatial tensor ρ^{CS}, defined relative to the PAS of the chemical shift interaction, as

$$R_{2m}^{CS} = \sum_{m'=-l}^{l} D_{m'm}^{(2)}(\alpha,\beta,\gamma)\rho_{2m'}^{CS} \tag{1.121}$$

where the components of ρ^{CS} are

$$\rho_{00}^{CS} = \delta_{iso}^{CS}, \tag{1.122}$$

$$\rho_{20}^{CS} = \sqrt{\frac{2}{3}}\Delta\delta, \tag{1.123}$$

$$\rho_{2\pm1}^{CS} = 0, \tag{1.124}$$

and

$$\rho_{2\pm2}^{CS} = \frac{\delta_{XX}^{CS} - \delta_{YY}^{CS}}{2}. \tag{1.125}$$

Using the above equations we can express the Hamiltonian as the sum of an isotropic component and an anisotropic component.

$$H_{CS} = \hbar\omega_0\delta_{iso}^{CS}I_z + \hbar\gamma\sum_{m=-2}^{2}(-1)^m T_{2m}^{CS}R_{2-m}^{CS}. \tag{1.126}$$

Again using static perturbation theory, to first order only the secular part of the Hamiltonian remains, allowing us to discard terms with $m > 0$. The Hamiltonian can then be written as

$$H_{CS} = \hbar\omega_0\delta_{iso}^{CS}I_z + \hbar\gamma T_{20}^{CS}R_{20}^{CS} = \hbar\omega_0\delta_{iso}^{CS}I_z + \hbar\omega_0\sqrt{\frac{2}{3}}R_{20}^{CS}I_z \tag{1.127}$$

The first term of eqn (1.127), the isotropic chemical shift, is normally incorporated into the Zeeman interaction and appears as an offset to the Larmor frequency. The second term eqn (1.127) is known as the chemical shift anisotropy (CSA). It will prove useful to express eqn (1.127) in a form similar to that of the quadrupolar Hamiltonian in eqn (1.112). We can define a chemical shift frequency Ω_{CS}, such that

$$\Omega_{CS} = \sum_{l=0,2}\mathcal{A}_{l0}^{CS}, \tag{1.128}$$

where

$$\mathcal{A}_{00}^{CS} = \omega_0\delta_{iso}^{CS} \tag{1.129}$$

and

$$\mathcal{A}_{20}^{CS} = \omega_0 \sqrt{\frac{2}{3}} R_{20}^{CS}. \tag{1.130}$$

If we wish to describe a system that has both quadrupolar and chemical shift elements, we can express the resulting Hamiltonian as

$$H = \hbar \Omega I_z = \hbar \sum_{l=0,2,4} \mathcal{A}_{l0} I_z. \tag{1.131}$$

The irreducible tensor $\mathcal{A}_{l0}$ includes contributions form both the chemical shift and quadrupolar interactions, since we can combine the chemical shift and quadrupolar tensors as follows:

$$\mathcal{A}_{00} = \mathcal{A}_{00}^{Q} + \mathcal{A}_{00}^{CS}, \tag{1.132}$$

$$\mathcal{A}_{20} = \mathcal{A}_{20}^{Q} + \mathcal{A}_{20}^{CS} \tag{1.133}$$

and

$$\mathcal{A}_{40} = \mathcal{A}_{40}^{Q}. \tag{1.134}$$

The Dipolar Interaction

The dipolar interaction Hamiltonian between two spins I_i and I_j can be expressed as

$$H_{D_{ij}} = -\hbar \omega_{D_{ij}} \sum_{m=-2}^{2} (-1)^m T_{2m}^{D_{ij}} A_{2-m}^{D_{ij}} \tag{1.135}$$

where $\omega_{D_{ij}}$ is defined as

$$\omega_{D_{ij}} = \frac{\gamma_i \gamma_j}{r_{ij}^3}. \tag{1.136}$$

The components of $T^{D_{ij}}$ are given by

$$T_{20}^{D_{ij}} = \frac{1}{\sqrt{6}} \left(3 I_{z,i} I_{z,j} - \mathbf{I}_i \cdot \mathbf{I}_j \right), \tag{1.137}$$

$$T_{2\pm1}^{D_{ij}} = \frac{\sqrt{2}}{2} \left(I_{z,i} I_{\pm1,j} + I_{\pm1,i} I_{z,j} \right), \tag{1.138}$$

and

$$T_{2\pm2}^{D_{ij}} = I_{\pm1,i} I_{\pm1,j} \,. \tag{1.139}$$

The components of $R^{D_{ij}}$ relative to the PAS frame of the dipolar interaction are

$$\rho_{20}^{D_{ij}} = \sqrt{\frac{3}{2}} \tag{1.140}$$

and

$$\rho_{2\pm1}^{D_{ij}} = \rho_{2\pm2}^{D_{ij}} = 0 \,. \tag{1.141}$$

Analysis of the dipolar interaction is complicated and commonly computed with the method of moments [19]. For the purposes of this thesis, the dipolar Hamiltonian can either be expressed for a homonuclear interaction as

$$H_D = \hbar \sum_{\substack{ij \\ i \neq j}} \omega_{D_{ij}} \frac{1}{\sqrt{6}} \left(3 I_{z,i} I_{z,j} - \mathbf{I}_i \cdot \mathbf{I}_j \right) A_{20}^{D_{ij}} \tag{1.142}$$

or for the heteronuclear case as

$$H_D = \hbar \sum_{\substack{IS \\ pairs}} \omega_{D_{IS}} \frac{3}{\sqrt{6}} I_z S_z A_{20}^{D_{IS}} \,. \tag{1.143}$$

Interaction with Radio-Frequency Irradiation

The Hamiltonian describing a rf pulse of frequency ω and field strength B_1 is

$$H_{rf} = -\hbar \gamma B_1 \left[\cos(\omega t + \phi) I_x + I_y \sin(\omega t + \phi) \right] \tag{1.144}$$

To simplify further calculations, the Hamiltonian is transferred into a rotating frame of frequency ω. The effective Zeeman and rf irradiation Hamiltonian can then be written

$$H_{eff} = \hbar(\omega - \omega_0) - \hbar \omega_1 \left(I_x \cos\phi + I_y \sin\phi \right) \tag{1.145}$$

where $\omega_1 = \gamma B_1$. Note that in the rotating frame, the Larmor frequency appears as an effective frequency $\omega - \omega_0$, and for an on-resonance pulse ($\omega = \omega_0$) the rf pulse induces rotations about an axis is the xy-plane. In such a case the rf Hamiltonian

can be expressed (assuming $\phi = 0$) as

$$H_{RF} = -\hbar\omega_1 I_x. \tag{1.146}$$

Chapter 2
Dynamic-Angle Spinning

Solid state nuclear magnetic resonance (NMR) spectroscopy of the central $(1/2 \leftrightarrow -1/2)$ transition of half-odd integer quadrupolar nuclei can yield information about the nuclear quadrupole interaction, which in turn can be correlated with the structural properties of a material [20-24]. As seen in the previous chapter, the central transition is broadened by the second-order anisotropic quadrupolar interaction often making the resolution of multiple-sites within a sample impossible. Solid state NMR techniques, such as magic-angle spinning (MAS) [25,26] and variable-angle spinning (VAS), can through the use of sample spinning, achieve high resolution spectra of spin-$1/2$ nuclei but fail to completely average the quadrupolar anisotropy. Dynamic-angle spinning (DAS) has been shown to average such broadening, producing narrow lines and resolution of crystallographically distinct sites for a variety of samples [27-32]. In this chapter, the basic technique of DAS will be explained and demonstrated using the spin-$3/2$ nucleus ^{87}Rb [33].

2.1 Magic-Angle Spinning

We will start our analysis of the effects of sample spinning for the simpler case of the chemical shift anisotropy (CSA), using the chemical shift Hamiltonian in eqn (1.128). If we rotate the sample at a frequency of ω_r about an axis oriented at an angle θ with respect to the magnetic field, then the chemical shift frequency Ω_{CS} becomes

$$\Omega_{CS}(t) = \sum_{l=0,2} \sum_{m=-l}^{l} D_{m0}^{(l)}(\omega_r t, \theta, 0) \mathcal{A}_{lm} . \tag{2.1}$$

In eqn (2.1) only those terms with $m \neq 0$ are time dependent and we can rewrite the Hamiltonian, separating the time-independent and time-dependent terms, as

$$\Omega_{CS}(t) = \mathcal{A}_{00} + D_{00}^{(2)}(\omega_r t, \theta, 0) \mathcal{A}_{20} + \sum_{\substack{m=-2 \\ m \neq 0}}^{2} D_{m0}^{(2)}(\omega_r t, \theta, 0) \mathcal{A}_{2m} . \tag{2.2}$$

The final term in eqn (2.2) is time dependent since it contains the terms $\exp(-im\omega_r t)$ and, as a result, is modulated by frequencies of $m\omega_r$. This modulation appears as the presence of spinning sidebands at multiples of the spinning frequency. If ω_r is greater than the width of the static powder pattern, then the effect of this modulation is negligible and the last term can be ignored. For this discussion on MAS, it will be assumed that the spinning frequency is sufficiently fast and the last term will be dropped. In Chapter 3, we will discuss methods of removing sidebands when the last term cannot be ignored, but for now we can rewrite eqn (2.2) using eqn (1.25) as

$$\Omega_{CS}(\alpha, \beta, \gamma, \theta) = \mathcal{A}_{00} + \mathcal{A}_{20}(\alpha, \beta, \gamma) P_2(\cos\theta) . \tag{2.3}$$

In eqn (2.3), the orientational dependence has been given explicitly. The first term, $\mathcal{A}_{00}$ is isotropic (eqn (1.129)) and therefore contains no dependence upon the orientation of the sample. In the second term, $\mathcal{A}_{20}$, the CSA, is dependent upon the Euler angles defining the orientation of the chemical shift tensor to the frame of the rotor (eqn (1.130)), and therefore will lead to a broadening of the spectrum because of the distribution of orientations present in a powder sample. However, if we can manipulate the spins in a way such that

$$P_2(\cos\theta) = \frac{1}{2}\left(3\cos^2\theta - 1\right) = 0 , \tag{2.4}$$

then the chemical shift anisotropy can be averaged to zero, i.e., $\langle \mathcal{A}_{20} \rangle = 0$. The

angle that solves eqn (2.4), the so-called second-rank magic angle, is

$$\theta_m = \cos^{-1}\left(\frac{1}{\sqrt{3}}\right) = 54.74°. \tag{2.5}$$

2.2 Dynamic-Angle Spinning

The Dynamic-Angle Spinning Experiment

When dealing with the second-order quadrupolar interaction, the situation is more complicated, but we can examine it in a similar manner. Starting with eqn (1.112), we calculate the frequency when the sample is rotating at a frequency ω_r around an axis oriented at angle θ with respect to the magnetic field. The quadrupolar frequency becomes time dependent and is expressed as

$$\Omega_Q(t) = \sum_{l=0,2,4} \sum_{m=-l}^{l} D^{(l)}_{m0}(\omega_r t, \theta, 0)\mathcal{A}_{lm}. \tag{2.6}$$

Again, we separate the time-independent from the time-dependent terms, yielding

$$\Omega_Q(t) = \sum_{l=0,2,4} D^{(l)}_{00}(\omega_r t, \theta, 0)\mathcal{A}_{l0} + \sum_{l=0,2,4} \sum_{\substack{m=-l \\ m\neq 0}}^{l} D^{(l)}_{m0}(\omega_r t, \theta, 0)\mathcal{A}_{lm}. \tag{2.7}$$

As in the case of MAS, the last term is time-dependent and can generate sidebands in the spectrum. For this discussion of DAS the spinning frequency will be assumed to be great enough to render the second term negligible. We can again expand eqn (2.7) using eqn (1.25), resulting in

$$\Omega_Q(\alpha,\beta,\gamma,\theta) = \mathcal{A}_{00} + \mathcal{A}_{20}(\alpha,\beta,\gamma)P_2(\cos\theta) + \mathcal{A}_{40}(\alpha,\beta,\gamma)P_4(\cos\theta) \tag{2.8}$$

As in the case of the CSA we find we have an orientationally independent term, which will be defined as the isotropic second-order quadrupolar shift, $\delta^{(2Q)}_{iso}$, (defined in Hz)

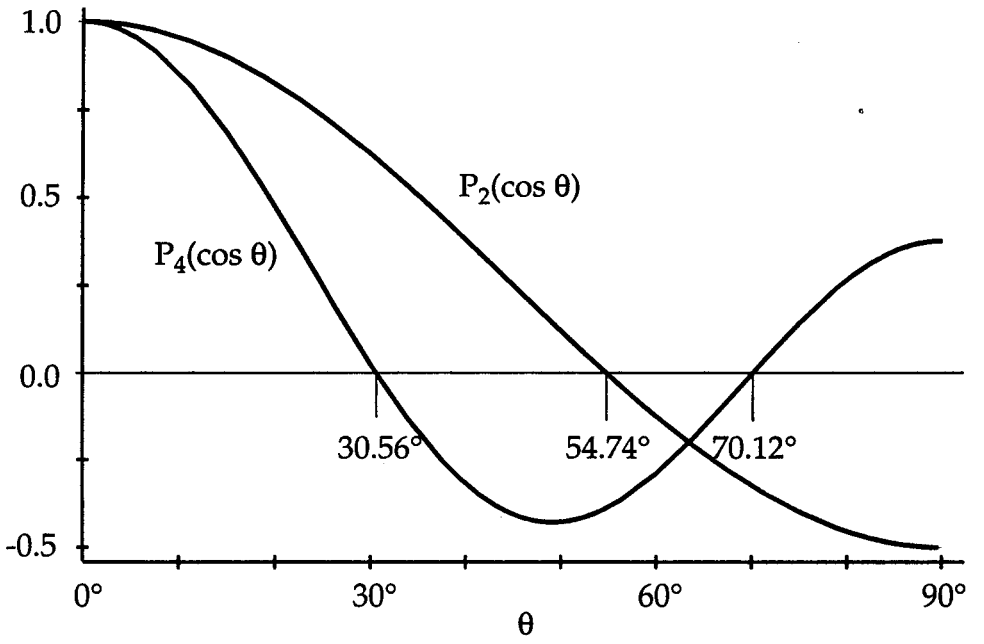

Figure 2.1 Plot of the second- (solid line) and fourth-rank (dashed line) Legendre polynomial of cos θ *vs.* θ. As shown, $P_2(\cos\theta)$ is zero when $\theta = 54.74°$ while the first two zeros of $P_4(\cos\theta)$ are at $\theta = 30.56°$ and $\theta = 70.12°$. The second- and fourth-rank polynomials have no common zero.

$$\delta_{iso}^{(2Q)} = \mathcal{A}_{00}^{Q}/2\pi = \frac{-3\left(I(I+1)-3/4\right)}{40\nu_0 I^2(2I-1)^2} C_Q^2\left(1+\frac{\eta^2}{3}\right), \tag{2.9}$$

where C_Q is defined in eqn (1.85) and $\nu_0 = \omega_0/2\pi$. We also have an orientationally dependent term that is scaled by $P_2(\cos\theta)$ and a second orientationally dependent term that is scaled by $P_4(\cos\theta)$. The sum of these two orientationally dependent terms will be defined as $\delta_{aniso}^{(2Q)}$.

We would, of course, like to find an angle θ where both $P_2(\cos\theta)$ and $P_4(\cos\theta)$ are zero simultaneously, so that $\left\langle \delta_{aniso}^{(2Q)} \right\rangle = 0$. However, as seen in Fig. 2.1 there is no single angle where both $P_2(\cos\theta)$ and $P_4(\cos\theta)$ are zero. Note that there are two fourth-rank magic angles, 30.56° and 70.12°, where the fourth-rank Legendre polynomial is zero; neither of these angles results in a zero second-rank polynomial. We can, however, find two angles that will yield the de-

sired averaging. One such experiment is double rotation DOR [34,35], where the sample is spun about two axes simultaneously. The axis angles chosen are the zeros of the second- and fourth rank Legendre polynomials, 54.74° and either 30.56° or 70.12°.

A second solution is dynamic-angle spinning (DAS) where the sample is spun about two different axes sequentially so that the net evolution period at both angles results in an averaging of the anisotropy to zero. Such a condition can be met if we can find a set of angles which solve the equations,

$$x_1 P_2(\cos\theta_1) + x_2 P_2(\cos\theta_2) = 0 \tag{2.10}$$

and

$$x_1 P_4(\cos\theta_1) + x_2 P_4(\cos\theta_2) = 0 \tag{2.11}$$

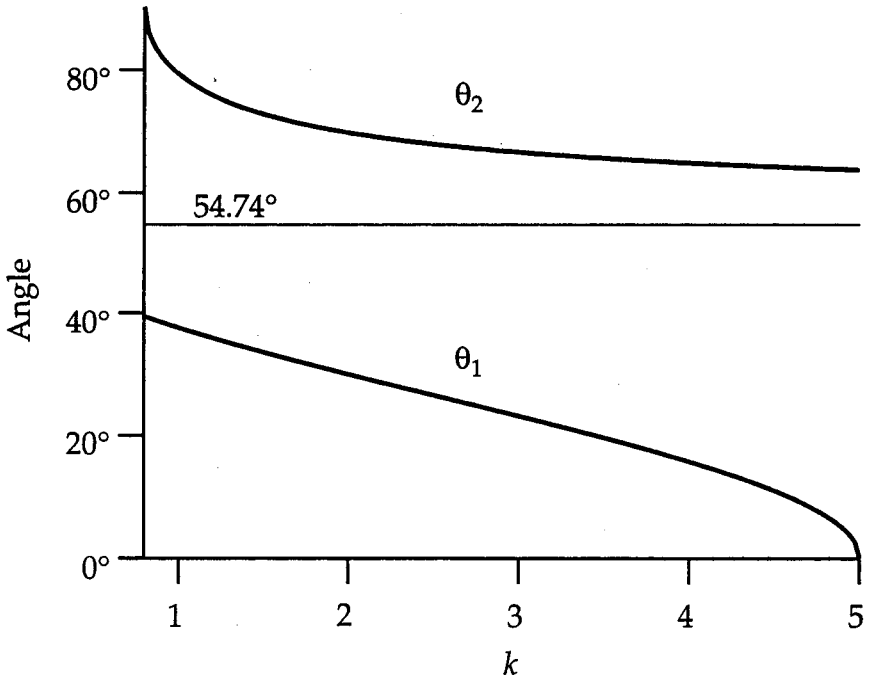

Figure 2.2 Solutions to eqns (2.10) and (2.11) plotted as DAS angle pair (θ_1, θ_2) *vs. k*. Solutions only exist for $k = 0.8$ to $k = 5.0$ and vary continuously from $\theta_1 = 0°$ to $\theta_1 = 39.23°$ and from $\theta_2 = 63.43°$ to $\theta_2 = 90°$.

where x_1 and x_2 are the fractions of time spent at the angles θ_1 and θ_2, respectively. To solve these equations we define a constant k such that

$$k \equiv \frac{x_2}{x_1}. \tag{2.12}$$

The pairs of angles which solve eqns (2.10) and (2.11) are

$$\theta_1 = \cos^{-1}\left(\sqrt{\frac{1+2\sqrt{k/5}}{3}}\right) \tag{2.13}$$

and

$$\theta_2 = \cos^{-1}\left(\sqrt{\frac{1-3\sqrt{1/5k}}{3}}\right) \tag{2.14}$$

and are plotted in Fig. 2.2. For a solution to exist k must be between $k = 0.8$ and $k = 5.0$. The allowed values of θ_1 and θ_2 are between $\theta_1 = 0°$ and $\theta_1 = 39.23°$ and between $\theta_2 = 63.43°$ to $\theta_2 = 90°$, respectively. No angle pair contains the second-rank magic angle 54.74°. However, the two fourth-rank magic angles, 30.56° and 70.12°, are an allowed set of DAS angles with $k = 1.87$.

Fig. 2.3 shows the basic DAS pulse sequence. As seen in the figure, an evolution period of $t_1/(k+1)$ at angle θ_1 with respect to the external field is followed by a $\pi/2$ storage pulse that stores the magnetization along the z-axis thus allowing for the hop to the second angle θ_2. After a second evolution period of $kt_1/(k+1)$, a DAS echo forms. The phase cycle, which can be calculated using the coherence transfer pathway given in Fig. 2.3 with the method explained in Chapter 1, is given in Table 2.1.

Table 2.1 Phase Cycle for experiment in Fig. 2.3.

φ_1	φ_2	φ_3	φ_r	φ_1	φ_2	φ_3	φ_r	φ_1	φ_2	φ_3	φ_r	φ_1	φ_2	φ_3	φ_r
0°	0°	0°	0°	0°	90°	0°	270°	0°	180°	0°	180°	0°	270°	0°	90°
90°	0°	0°	90°	90°	90°	0°	0°	90°	180°	0°	270°	90°	270°	0°	180°
180°	0°	0°	180°	180°	90°	0°	90°	180°	180°	0°	0°	180°	270°	0°	270°
270°	0°	0°	270°	270°	90°	0°	180°	270°	180°	0°	90°	270°	270°	0°	0°

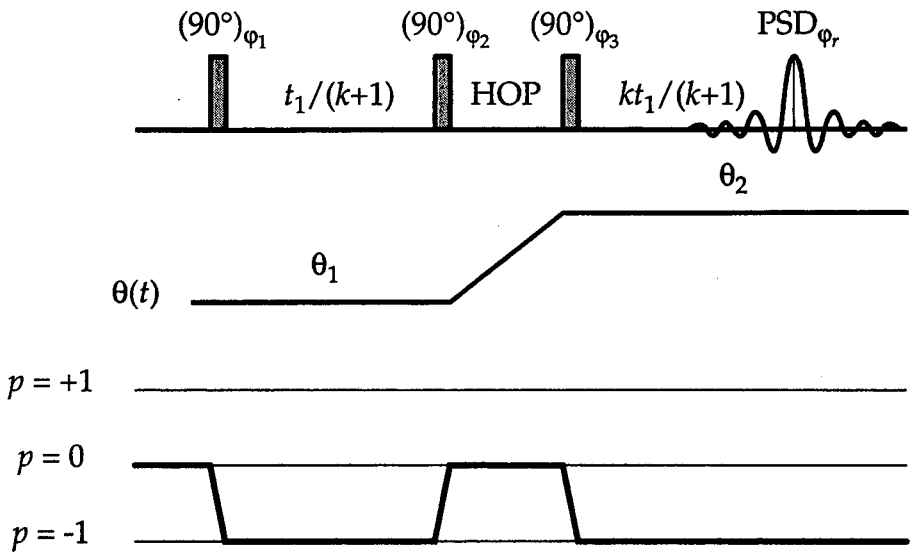

Figure 2.3 The basic DAS pulse sequence consists of a $\pi/2$ pulse followed by an evolution period of $t_1/(k+1)$ while the sample is spun about an axis oriented at an angle θ_1 with respect to the external field (the direction of which defines the z-axis). A second $\pi/2$ pulse stores the magnetization along the z-axis to allow for the hop to the second angle θ_2. After a second evolution period of $kt_1/(k+1)$, a DAS echo forms, and one point in the isotropic spectrum can be collected. By incrementing t_1, a two-dimensional spectrum can be taken. The desired coherence transfer pathway is shown at the bottom.

Pure Phase DAS

The pulse sequence in Fig. 2.3, leads a two-dimensional spectrum with phase-twisted lineshape, which means that the lineshape contains a mixture of absorptive and dispersive Lorentzian elements. The signal arising from a two-dimensional experiment can be expressed as

$$S(t_1,t_2) = e^{-(t_1+t_2)/T_2} e^{-i\Omega_1 t_1} e^{-i\Omega_2 t_2} \tag{2.15}$$

where Ω_1 and Ω_2 are the frequencies for a given peak in the first and second dimensions, respectively, and $1/2T_2$ is the linewidth. The first Fourier transform with respect to t_2 gives

$$S(t_1,\omega_2)=e^{-t_1/T_2}e^{-i\Omega_1 t_1}\left[A(\omega_2,\Omega_2)+iD(\omega_2,\Omega_2)\right], \tag{2.16}$$

where $A(\omega_2, \Omega_2)$, the absorptive Lorentzian lineshape function is

$$A(\omega,\Omega)=\frac{T_2}{1+(\omega-\Omega)^2T_2^2} \tag{2.17}$$

and $D(\omega_2, \Omega_2)$, the dispersive Lorentzian lineshape function is

$$D(\omega,\Omega)=\frac{(\omega-\Omega)T_2^2}{1+(\omega-\Omega)^2T_2^2}. \tag{2.18}$$

The second Fourier transform produces

$$\begin{aligned}S(\omega_1,\omega_2)=&\left[A(\omega_1,\Omega_1)A(\omega_2,\Omega_2)-D(\omega_1,\Omega_1)D(\omega_2,\Omega_2)\right]\\&+i\left[A(\omega_1,\Omega_1)D(\omega_2,\Omega_2)-D(\omega_1,\Omega_1)A(\omega_2,\Omega_2)\right]\end{aligned}. \tag{2.19}$$

As can be seen in eqn (2.19), the real component of the signal contains both absorptive and dispersive terms, which leads to an undesirable lineshape that requires taking the magnitude of the data.

Several of the traditional methods of producing pure-phase spectra, including the method of States *et al.* [36], time-proportional phase incrementation (TPPI) [37,38], and whole echo acquisition [39] have been used to produce pure-phase DAS spectra; details can be found in references [27,40-42].

Most of the spectra presented in this thesis have been obtained using whole-echo acquisition in which a pulse sequence of the form

$$\pi/2\text{—}t_{echo}\text{—}\pi\text{—}acquisition \tag{2.20}$$

is used to refocus the signal and produce an echo. If the entire echo is collected, the signal is of the form

$$S(t_1,t_2)=e^{-(t_2-t_{echo})^2/T_2^2}e^{-i\Omega_2(t_2-t_{echo})}e^{-t_1/T_2}e^{-i\Omega_1 t_1}. \tag{2.21}$$

A Fourier transform with respect to t_2 followed by a phase correction of t_{echo} applied to the ω_2 dimension, and then a Fourier transform with respect to t_1 gives

$$S(\omega_1,\omega_2) = A_{se}(\omega_2,\Omega_2)\left[A(\omega_1,\Omega_1) - iD(\omega_1,\Omega_1)\right] \tag{2.22}$$

where

$$A_{se}(\omega_2,\Omega_2) = e^{-(\omega_2-\Omega_2)^2 T_2^2/4} \tag{2.23}$$

giving a pure-absorption mode two-dimensional spectrum.

The method of States, in which a hypercomplex data set is collected, is also used on occasion in this thesis. Two data sets are acquired, the first cosine modulated in t_1, and the second sine modulated in t_1. The resulting signal can be expressed as

$$S_c(t_1,t_2) = \cos(\Omega_1 t_1) e^{-(t_1+t_2)/T_2} e^{-i\Omega_2 t_2} \tag{2.24}$$

and

$$S_s(t_1,t_2) = \sin(\Omega_1 t_1) e^{-(t_1+t_2)/T_2} e^{-i\Omega_2 t_2}\,. \tag{2.25}$$

A Fourier transform with respect to t_2 is performed on each data set and then the data sets are combined to form a data set whose real component is $\mathrm{Re}\left[S_c(t_1,\omega_2)\right]$ and whose imaginary component is $\mathrm{Im}\left[S_s(t_1,\omega_2)\right]$. The result is given by

$$S(t_1,\omega_2) = A(\omega_2,\Omega_2) e^{-t_1/T_2} e^{-i\Omega_1 t_1}\,. \tag{2.26}$$

A pure-phase data set results when eqn (2.26) is Fourier transformed with respect to t_2. The phase cycles necessary to obtain a hypercomplex data set can be calculated using the coherence transfer pathways method described in Chapter 1 by recognizing that both the $p = +1$ and $p = -1$ pathways must be collected in the t_1 dimension. The sum of the two pathways produces a cosine modulated data set and the difference produces a sine modulated data set.

Multiple Field DAS

The isotropic shifts observed in the F_1 dimension of a DAS spectrum can be expressed as

$$\delta_{obs} = \delta_{iso}^{CS} + \delta_{iso}^{(2Q)}, \tag{2.27}$$

where δ_{iso}^{CS} is the isotropic chemical shift and $\delta_{iso}^{(2Q)}$ is the second-order isotropic quadrupolar shift, given in eqn (2.9). Evaluating the constants in eqn (2.9), the second-order quadrupolar shift may be written

$$\delta_{iso}^{(2Q)} = -\left(1.28\times10^{-10}\,\frac{\mathrm{T}^2}{\mathrm{Hz}^2}\right)P_Q^2\left(\frac{1}{B_0^2}\right) \tag{2.28}$$

where the quadrupolar product, P_Q is defined by

$$P_Q \equiv C_Q\sqrt{1+\frac{\eta^2}{3}}. \tag{2.29}$$

Note that, in ppm, the isotropic chemical shift is independent of field strength while the second-order quadrupolar shift is proportional to the inverse of the Larmor frequency. By measuring the total isotropic shift at various field strengths, we can calculate δ_{iso}^{CS} and P_Q, using the equation

$$\delta_{obs} = \delta_{iso}^{CS} - \left(1.28\times10^{-10}\,\frac{\mathrm{T}^2}{\mathrm{Hz}^2}\right)P_Q^2\left(\frac{1}{B_0^2}\right). \tag{2.30}$$

Note that the values of C_Q and η_Q are not uniquely specified by P_Q; an independent method, such as simulations, must be used to determine these values.

2.3 Dynamic-Angle Spinning of Rubidium-87

Alkali metals such as rubidium are important in a number of areas, serving as promoters in the heterogeneous catalysis of ammonia synthesis [43] and the oxidative coupling of methane to yield ethane and ethene [44]. Rubidium is an important component of some glasses [45], and it has been shown that buckminsterfullerene, C_{60}, doped with Rb metal becomes superconducting with a transition temperature of 28 K [46].

In order to assess the applicability of dynamic-angle spinning NMR to

rubidium and its potential to yield structural information about materials such as those listed above, ^{87}Rb MAS, VAS and DAS spectra were obtained for five inorganic rubidium salts: RbCl, $RbClO_4$, Rb_2SO_4, Rb_2CrO_4 and $RbNO_3$. We show that substantial narrowing of the spectral lines occurs in DAS over MAS or VAS. Using pure-phase MAS-detected DAS experiments together with single site simulations and phase-modulated DAS experiments at several field strengths, we have extracted quadrupolar parameters for the various ^{87}Rb sites in each compound. The static lineshapes of all of these compounds have previously been studied by Cheng *et al.* [47], in order to obtain values for quadrupolar and chemical shift parameters. Crystal structures for all of the compounds RbCl [48], $RbClO_4$ [49], Rb_2CrO_4 [50], Rb_2SO_4 [51], and $RbNO_3$ [52,53], have also been determined previously and are used to identify the number of inequivalent sites in each compound.

Experimental

All rubidium compounds were obtained from Alfa Products, Morton Thiokol, Inc., or Aldrich Chemical Co., and were used without further purification. Spectra were acquired at 7.0 T (98.55 MHz), 9.4 T (130.89 MHz) and 11.7 T (163.62 MHz), using the probe design described in reference [54] and the pulse sequences given earlier and shown in Fig. 2.4. The ^{81}Br signal in solid KBr was used as an internal standard for calibration of the magic angle. All spectra are referenced relative to aqueous 1 M $RbNO_3$ as an external frequency standard. Either 256 or 512 complex points were acquired in t_2 and between 128 and 512 real points in t_1. Spectra were acquired with 1.0 s relaxation delays and pulses selective for the central transition of approximately 5 μs (B_1 ~ 20 G). Hopping times for the reorientation of the rotor axis were about 30 ms. Normal rotor spinning speeds were between 6.5 and 7.8 kHz. All VAS, MAS, and static spectra

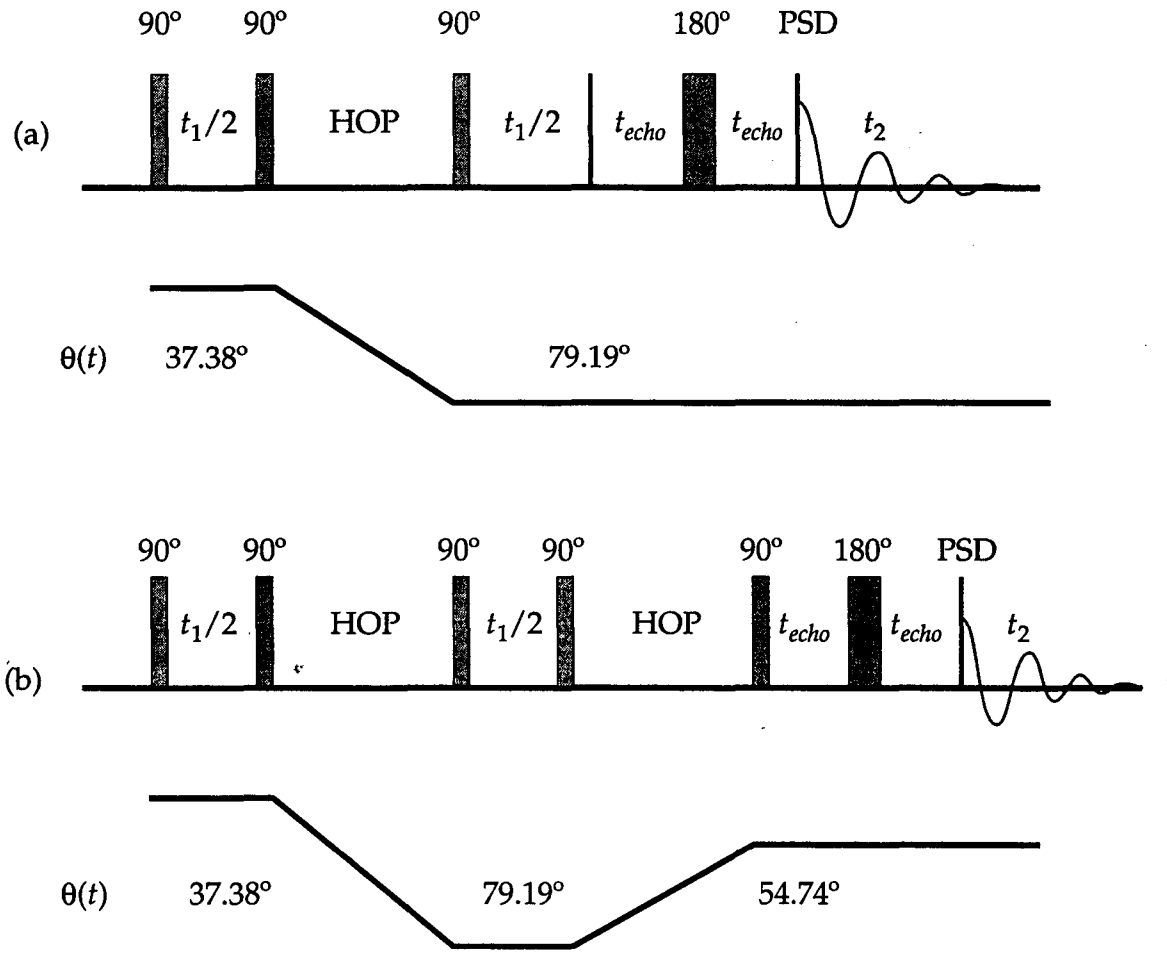

Figure 2.4 DAS pulse sequences used for experiments on ^{87}Rb. The pulse sequence in (a) gives a phase-modulated data because the entire echo is not acquired, while the pulse sequence in (b) adds a second hop to the magic angle after the second DAS evolution period. Pure phase data was collected by taking a hyper-complex data set in t_1.

were acquired using a Hahn-echo pulse sequence. Procedures for performing simulations can be found in reference [55].

Results and Discussion

Figs. 2.5 and 2.6 show the VAS and DAS spectra, respectively, of ^{87}Rb at 11.7 T in RbCl, $RbClO_4$, Rb_2SO_4, Rb_2CrO_4 and $RbNO_3$. In all cases except for RbCl, there is narrowing by over an order of magnitude in the high-resolution

DAS dimension over the MAS spectra. The MAS spectrum of the RbCl (Fig. 2.5a) gives a slightly narrower line than the DAS spectrum (Fig. 2.6a). This is as expected since the rubidium nucleus is in an environment of cubic symmetry within the crystal [48]; therefore, there is no second-order broadening. Both DAS and MAS will average first-order quadrupolar and chemical shift anisotropy, but only MAS will average the homonuclear dipolar interaction. This is because multilinear homonuclear terms such as $I_{1+}I_{2z}...I_{nz}$ (eqn (1.135)) created during the first DAS evolution period are not stored during the hop and therefore cannot be refocused during the second DAS evolution period. The additional broadening in the DAS spectrum of RbCl arises from the scaled homonuclear dipolar interaction. For a discussion on the DAS dipolar linewidth refer to references [55] and [56].

The MAS spectrum of $RbClO_4$ (Fig. 2.5b) yields a well resolved powder pattern which may be simulated easily (Table 2.2). These simulations agree completely with the isotropic chemical shift and quadrupolar parameters determined by the DAS measurements (Fig. 2.6b) at the two different fields. The ^{87}Rb VAS spectrum of Rb_2SO_4 (Fig. 2.5c) shows that two powder patterns centered at -18 and 33 ppm can be resolved. The 79.19° spectrum is shown instead of the MAS spectrum because the 79.19° spectrum is significantly narrower.

Table 2.2 Results from simulating single-site ^{87}Rb MAS/DAS spectra of $RbClO_4$ and $RbNO_3$ taken at 11.7 T.

	δ_{iso}^{CS} / ppm	P_Q / MHz	C_Q / MHz	η_Q
$RbClO_4$	-16.2 ± 1.0	3.21 ± 0.05	3.20 ± 0.05	0.10 ± 0.05
	-26.2 ± 1.0	1.83 ± 0.05	1.83 ± 0.05	0.12 ± 0.05
$RbNO_3$	-26.8 ± 1.0	2.39 ± 0.07	2.07 ± 0.05	1.00 ± 0.05
	-30.9 ± 1.0	1.91 ± 0.06	1.85 ± 0.05	0.48 ± 0.05

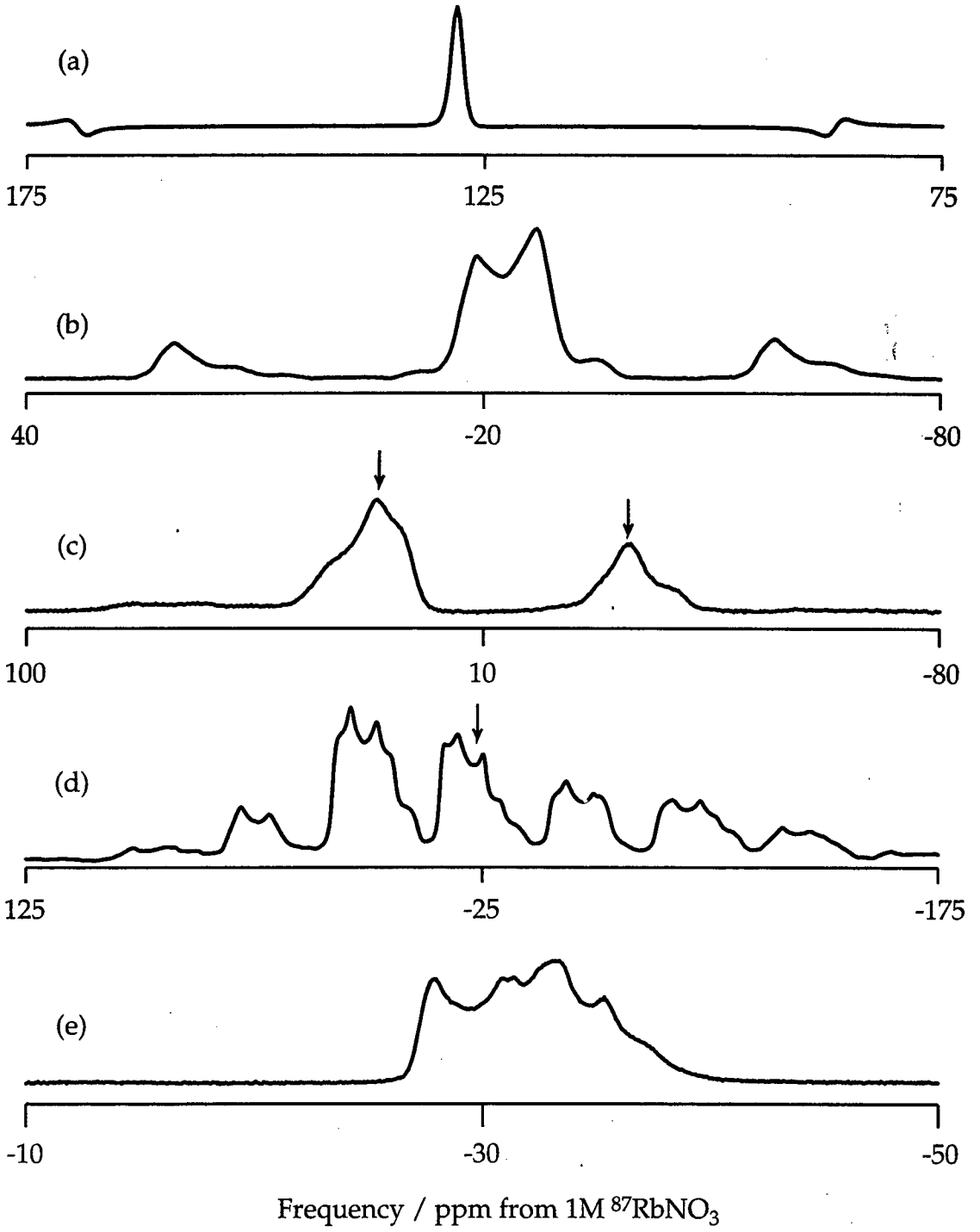

Figure 2.5 ^{87}Rb VAS spectra at 11.7 T of (a) RbCl at 54.74°, (b) $RbClO_4$ at 54.74°, (c) Rb_2SO_4 at 79.19°, (d) Rb_2CrO_4 at 54.74°, and (e) $RbNO_3$ at 54.74°.

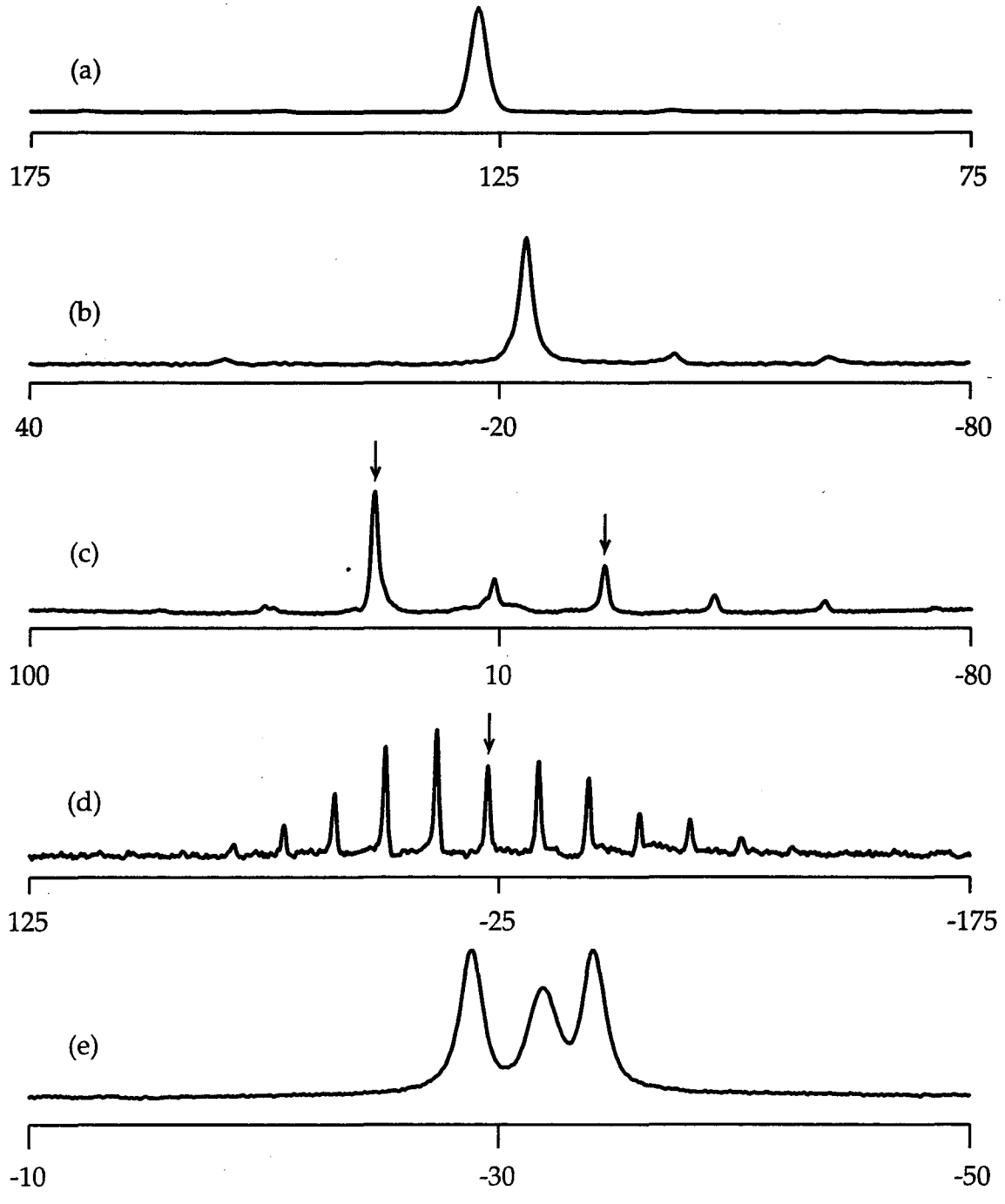

Figure 2.6 ^{87}Rb DAS spectra of (a) RbCl (b) $RbClO_4$ (c) Rb_2SO_4, (d) Rb_2CrO_4, and (e) $RbNO_3$.

These lines narrow substantially under DAS (Fig. 2.6c) to give two sharp peaks corresponding to the two crystallographically distinct rubidium sites in this compound. One of these resonances is clearly present at $\delta_{obs}^{11.7T} = 34\,\text{ppm}$, while the upfield site is broken into spinning sidebands. Assignment of the line at $\delta_{obs}^{11.7T} = -10\,\text{ppm}$ to the isotropic resonance position of the second site was made by comparing DAS spectra taken at spinning speeds of 5.3 and 6.5 kHz.

The DAS (Fig. 2.6d) and MAS (Fig. 2.5d) spectra of Rb_2CrO_4 show a single site with prominent sets of spinning sidebands. The isotropic line was assigned by performing DAS at two different spinning speeds. However, there are two crystallographically distinct rubidium sites in Rb_2CrO_4 [50]. The large C_Q (~12 MHz) for the second site [47] makes it unobservable because the total intensity is distributed over a bandwidth that is too broad to be excited with 5 μs rf pulses.

The MAS spectrum of $RbNO_3$ (Fig. 2.5e) consists of three overlapping

Table 2.3 Results from DAS experiments of various rubidium compounds at 9.4 and 11.7 T. δ_{iso}^{CS} and P_Q were determined using eqn (2.30). ‡ This site was too broad for detection.

	$\delta_{obs}^{9.4T}$/ppm	$\delta_{obs}^{11.7T}$/ppm	δ_{iso}^{CS}/ppm	P_Q / MHz
RbCl	127 ± 1	127 ± 1	127 ± 2	~0
$RbClO_4$	-28 ± 1	-23 ± 1	-14 ± 2	3.1 ± 0.3
Rb_2SO_4	-25 ± 1	-10 ± 1	16 ± 2	5.3 ± 0.2
	29 ± 1	34 ± 1	42 ± 2	3.0 ± 0.3
Rb_2CrO_4	-27 ± 1	-21 ± 1	-11 ± 2	3.3 ± 0.3
	‡	‡	‡	‡
$RbNO_3$	-32 ± 1	-29 ± 1	-24 ± 2	2.4 ± 0.4
	-36 ± 1	-32 ± 1	-25 ± 2	2.8 ± 0.4
	-37 ± 1	-34 ± 1	-29 ± 2	2.4 ± 0.4

powder patterns which give rise to narrow, resolved lines under DAS (Fig. 2.6e). In Fig. 2.7 is the two-dimensional MAS-detected DAS spectrum of $RbNO_3$ taken with the pulse sequence in Fig. 2.4b at 11.7 T. Each of the three sites is resolved in the isotropic DAS dimension and correlated to its MAS powder pattern. The cross-sections through the MAS powder patterns in the F_2 dimension are shown

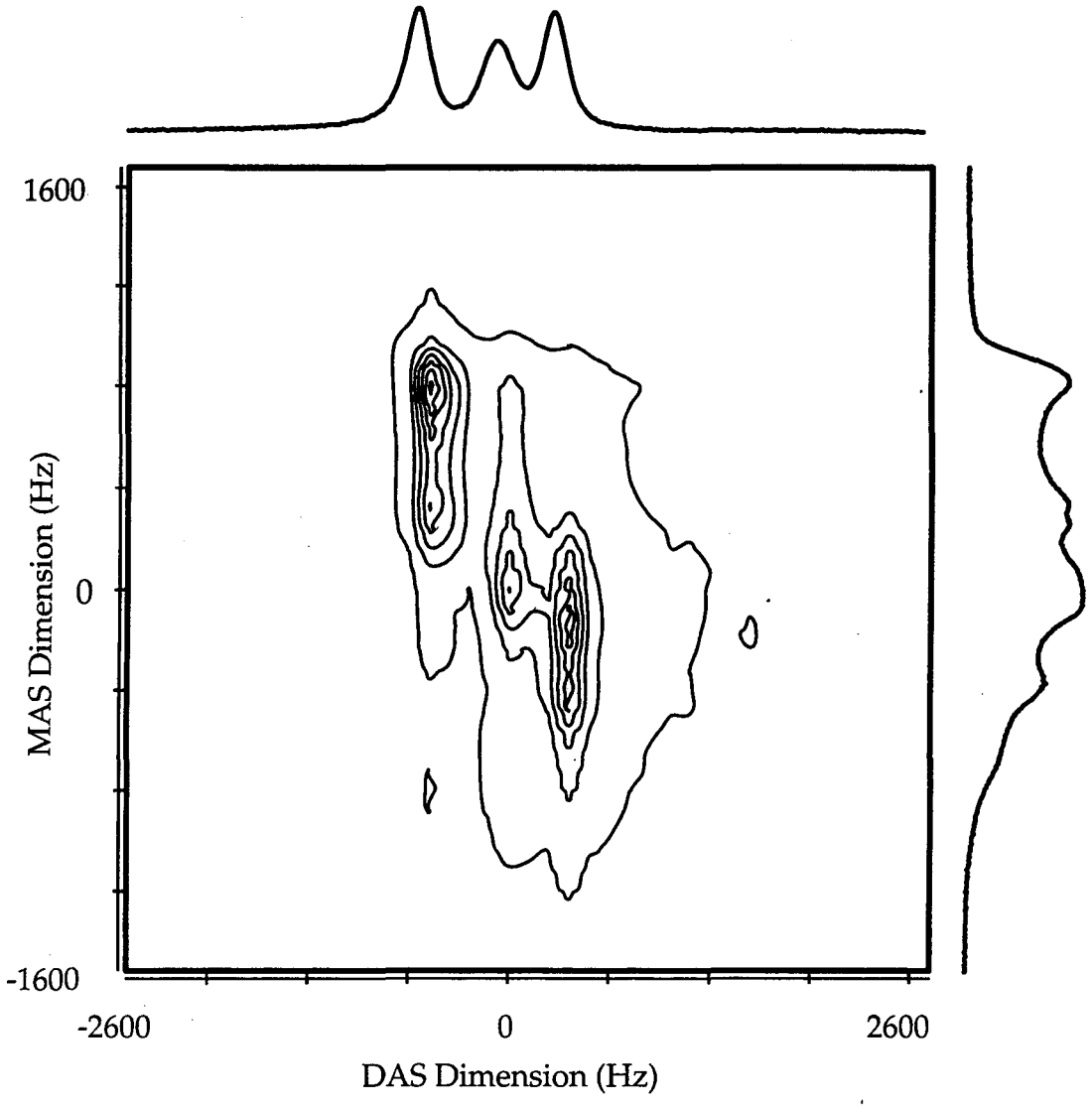

Figure 2.7 Two-dimensional MAS-detected spectrum of $RbNO_3$ taken at 11.7 T with the pulse sequence in Fig. 2.4b. MAS powder patterns for each site are separated by their total isotropic shift.

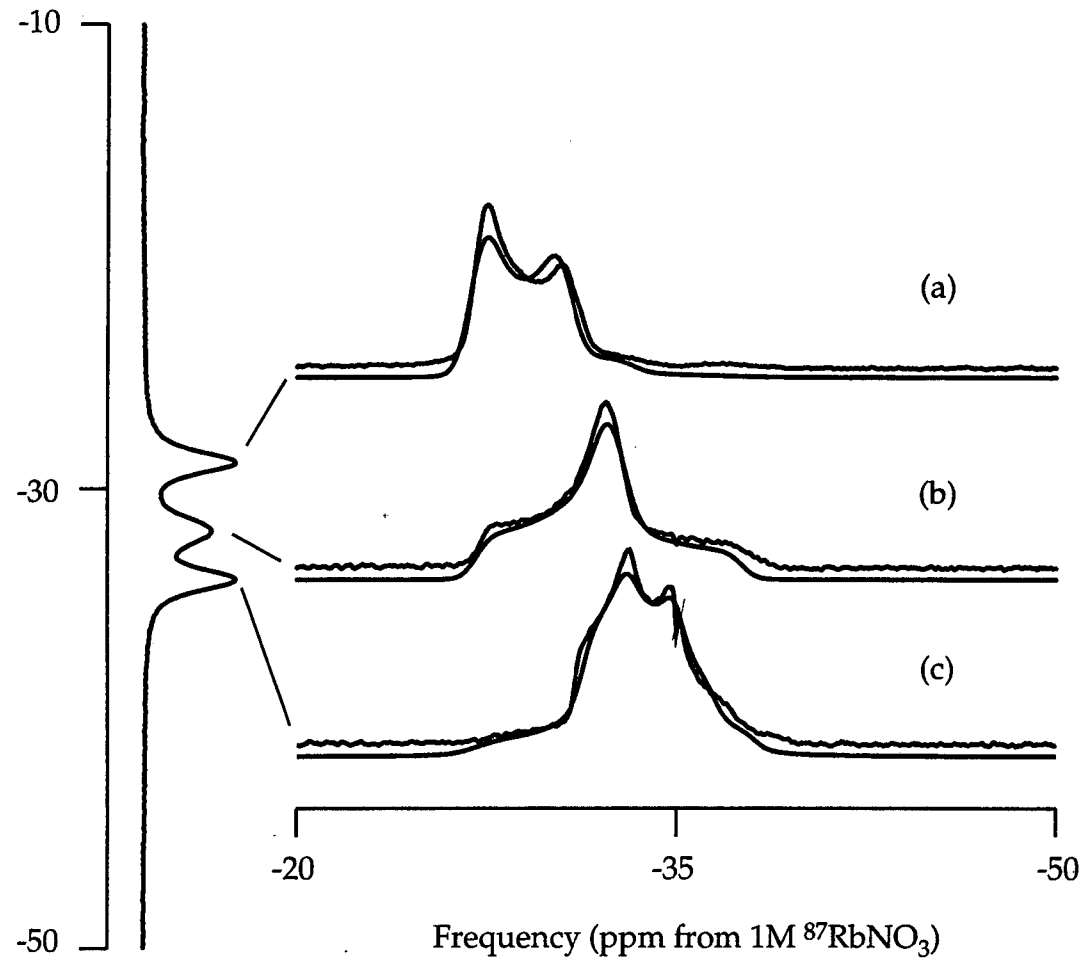

Figure 2.8 Single-site MAS spectra with simulations overlaid taken from Fig. 2.7. Slices through the isotropic DAS dimension are at (a) -29 ppm, (b) -32 ppm, and (c) -34 ppm.

cross-sections through the MAS powder patterns in the F_2 dimension are shown in Fig. 2.8 for each of the three isotropic frequencies in F_1. Simulations of these three powder patterns are also shown in figure Fig. 2.8, and the values of δ_{iso}^{CS}, C_Q, and η_Q obtained by simulating each site are given in Table 2.2. Each simulation started with a different set of initial parameters covering a wide range of values, with all simulations converging to the same set of parameters within ±0.01%. The estimates which are shown in Table 2.2 for the absolute accuracy of

the simulations are that C_Q is accurate to ±0.05 MHz, η_Q to ±0.05, and the isotropic chemical shift to ±1.0 ppm.

The total isotropic shift at both 9.4 and 11.7 T along with the isotropic chemical shift, δ_{iso}^{CS}, and the quadupolar product, P_Q, calculated from the DAS spectra of the five salts at these two fields using eqn (2.30), are tabulated in Table 2.3. Calculation of P_Q and δ_{iso}^{CS} using data from DAS spectra taken at only two different field strengths can introduce large errors, since this requires two DAS measurements and two external references. Furthermore, since P_Q is proportional to the square root of the difference between the two isotropic shifts at two different fields, smaller differences lead to larger errors. The overall errors reported in Table 2.3 for the calculated parameters were made assuming that the measurements are accurate to ±1 ppm. Since the errors of the parameters determined by simulation of a single site can be less than those determined by two field measurements, it is highly desirable to perform simulations in conjunction with the measurements at two or more magnetic field strengths.

By performing measurements at several different magnetic field strengths, the accuracy and precision of the calculated product, P_Q, and δ_{iso}^{CS} may be greatly improved. This has been done with $RbNO_3$ by comparing the results performed at three field strengths from this work with measurements taken at 4.2 T [42]. Fig. 2.9 shows the field-dependent shift of the four lines in $RbNO_3$ obtained from these DAS experiments at 4.2, 7.0, 9.4 and 11.7 T. The total isotropic frequency δ_{obs} is plotted *vs.* $(1/B_0)^2$ in Fig. 2.10, demonstrating the predicted linear relationship. The slope of each line may be related to P_Q by eqn (2.30), while the zero intercept (which corresponds to infinite field) is simply δ_{iso}^{CS}. A linear least squares analysis allows estimation of errors and we observe a dramatic improvement over two field results (almost a factor of 10). This improvement

arises due to the large range isotropic shift differences between the measurements at all four fields. The results and errors are compiled in Table 2.4 and agree very well with our simulations.

The isotropic shift for RbCl that reported above is in very good agreement with the work by Cheng *et al.* [47], indicating that the external references were consistent with theirs, but the determination of the isotropic chemical shifts for the other salts using DAS are different. Dynamic-angle spinning should give more precise values than wide-line simulation techniques, which require a large number of adjustable parameters, since DAS allows the determination of isotropic chemical shifts and P_Q directly. Furthermore, in the case of $RbNO_3$, DAS allows the separation of MAS powder patterns and the determination of isotropic chemical shifts, quadrupolar coupling constants, and asymmetry parameters for each of the $RbNO_3$ sites through single site simulation. The quadrupolar parameters determined for $RbNO_3$ by multiple-field DAS measurements agree quite well with a previous study performed in low magnetic field by Segel [57].

Table 2.4 Data (rows 1-4) and results (rows 5-6) from a linear least squares fit of the data graphed in Fig. 2.10 for $RbNO_3$. The sites are identified by the asymmetry parameter η_Q obtained from the simulations.

	$\eta_Q = 0.12$	$\eta_Q = 1.00$	$\eta_Q = 0.48$
$\delta_{obs}^{4.2T}$/ppm	-48.4 ± 1.0	-67.5 ± 1.0	-55.3 ± 1.0
$\delta_{obs}^{7.0T}$/ppm	-34.4 ± 1.0	-40.2 ± 1.0	-39.8 ± 1.0
$\delta_{obs}^{9.4T}$/ppm	-32.0 ± 1.0	-36.0 ± 1.0	-37.0 ± 1.0
$\delta_{obs}^{11.7T}$/ppm	-29.0 ± 1.0	-32.0 ± 1.0	-34.0 ± 1.0
δ_{iso}^{CS}/ppm	-26.8 ± 0.8	-26.8 ± 0.8	-31.6 ± 0.8
P_Q / MHz	1.72 ± 0.06	2.36 ± 0.04	1.81 ± 0.05

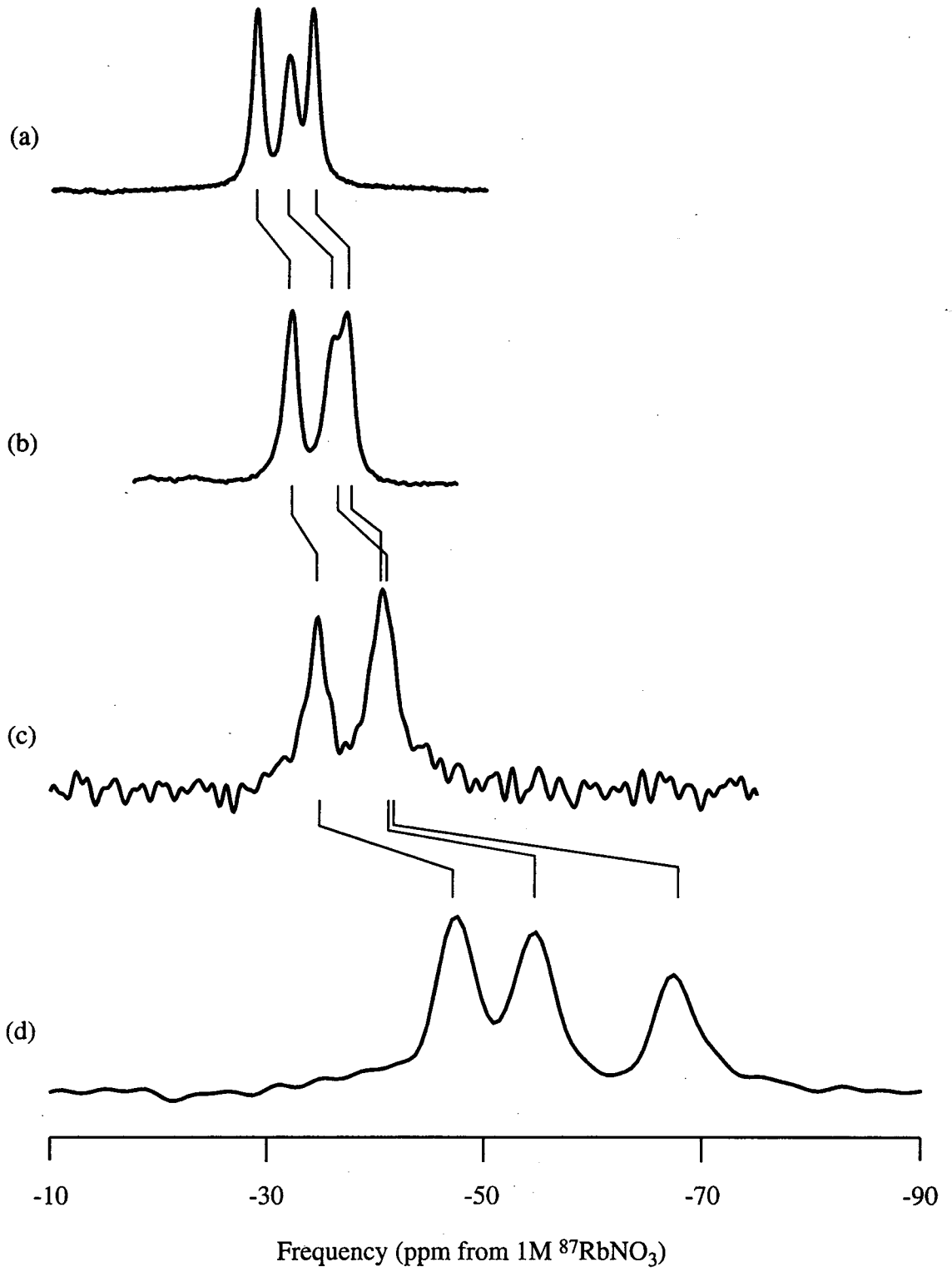

Figure 2.9 ^{87}Rb DAS spectra of $RbNO_3$ acquired at (a) 11.7 T, (b) 9.4 T, (c) 7.0 T, and (d) 4.2 T.

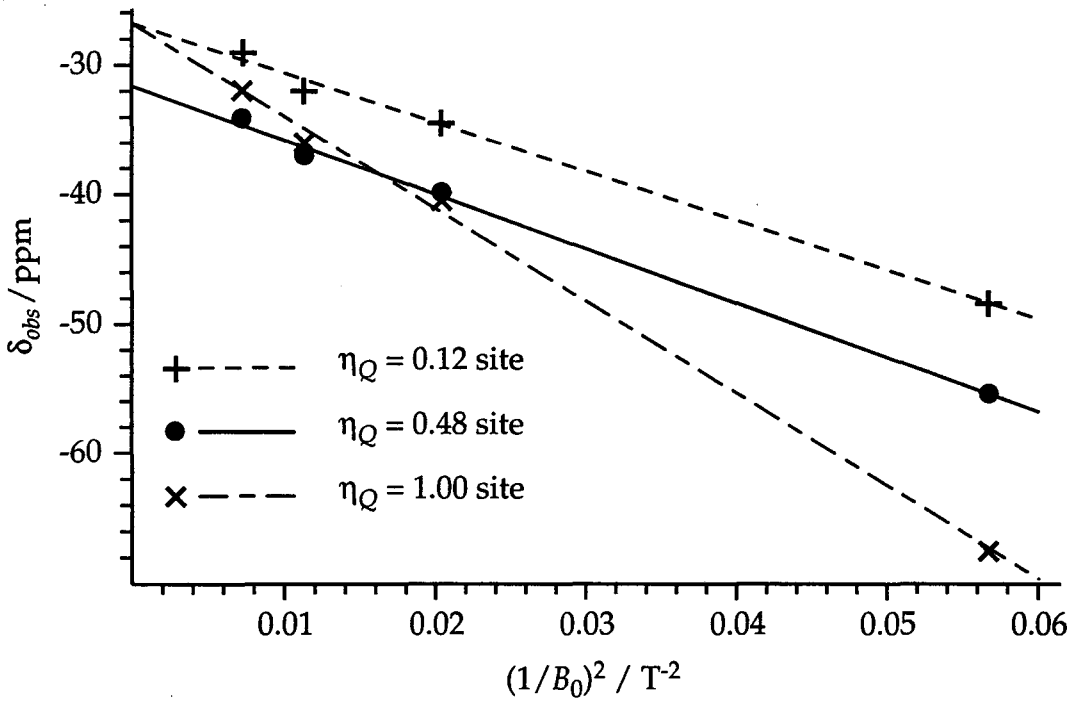

Figure 2.10 Isotropic shifts (δ_{obs}) of $^{87}RbNO_3$ plotted vs. $(1/B_0)^2$ and fit using a linear least squares algorithm. Using the slopes and intercepts, the values of δ_{obs}^{CS} and P_Q are calculated and tabulated in Table 2.4.

Chapter 3
Dynamic-Angle Hopping

3.1 Background and Theory

For a static sample, the secular part of the Hamiltonian is given in eqn (1.131) as

$$H = \hbar\Omega I_z = \hbar\sum_l \mathcal{A}_{l0} I_z \tag{3.1}$$

where $\mathcal{A}_{l0}$ describes the spatial tensors of the CSA and quadrupolar interactions with rank $l = 0$ or $l = 2$ for CSA and $l = 0$, $l = 2$, or $l = 4$ for the quadrupolar interaction. The anisotropic components of these interaction are contained in the $\mathcal{A}_{l0}$ with rank l greater than zero as explained in Chapter 2; motional averaging experiments such as MAS, DAS, and DOR attempt to obtain high resolution by averaging to zero the $\mathcal{A}_{l0}$ with rank greater than zero.

However, as mentioned in Chapter 2, one of the drawbacks of spinning experiments is the introduction of a time dependence to the Hamiltonian, and this time dependence introduces sidebands. Sidebands are artifacts that appear at integer multiples of the spinning speed [58]. If the spinning speed is sufficiently fast, the intensity of the sidebands is negligible and they do not complicate the spectrum. However, for many sample of interest, such speeds cannot be obtained. Spinning the sample at high speeds also requires a decrease in sample volume and therefore a decrease in sensitivity, which can cause problems for low gamma nuclei or for samples where enriching is unfeasible. There are sideband suppression techniques such as TOSS [59], however, these can also lead to a loss

of signal intensity.

Another approach to removing sidebands is to remove the time dependence of the Hamiltonian. This can be seen by examining the background of motional averaging experiments. Sample spinning is an implementation of the following theoretical experiment. Allow a static sample to evolve for equal times at various orientations with respect to the magnetic field. If the proper orientations are chosen, such an experiment will result in $\mathcal{A}_{l0}$ with $l > 0$ being averaged to zero. This is a consequence of the symmetry of the irreducible spherical tensors $\mathcal{A}_{l0}$. For example, a second-rank spherical tensor is averaged to zero if it undergoes reorientations with octahedral symmetry, such as being moved instantly between the vertices of an octahedron. Reorientations with icosahedral symmetry, such as being instantly moved between the vertices of an icosahedron, will average to zero both second- and fourth-rank interactions. Under such reorientations, the effective Hamiltonian can be written as

$$\langle H \rangle = \hbar \sum_{l} \langle \mathcal{A}_{l0} \rangle I_z = \hbar \mathcal{A}_{00} I_z , \tag{3.2}$$

with only the isotropic component remaining.

In practice it not possible to instantly reorient the sample between the various orientations. One implementation that will average second-rank interactions is a two-dimensional experiment called magic-angle hopping (MAH) developed by Szeverenyi, *et al.* [60], in which a sample is rotated in 120° steps about an axis inclined at the magic angle (54.74°). During the reorientation, the magnetization is stored with $\pi/2$ pulses along the direction of the magnetic field. In another method developed by Gan [61], the sample slowly rotates about the magic angle and storage pulses are used to interrupt the evolution and approximate 120° hops.

One big disadvantage of these experiments is the use of the $\pi/2$ pulses.

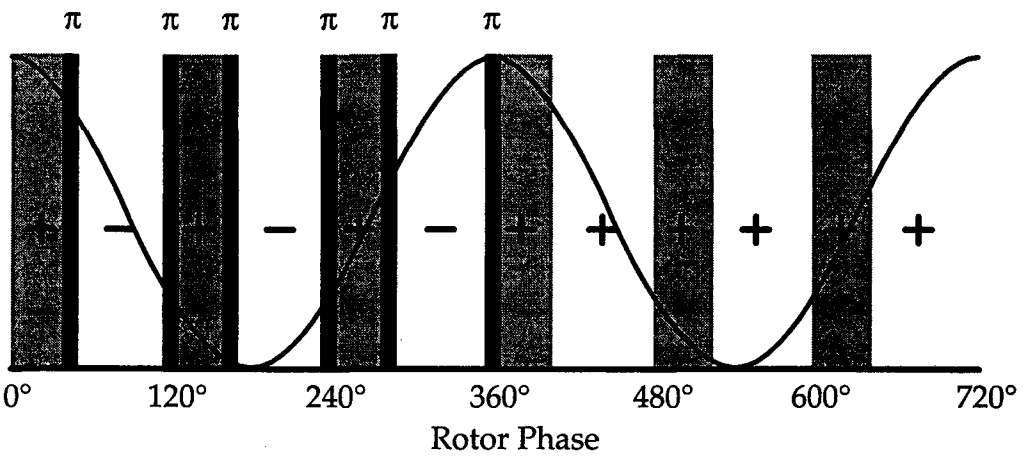

Figure 3.1 In the basic MAH-180 experiment, periods of isotropic evolution (in gray) 120° apart are sandwiched by π-pulses such that the isotropic evolution adds across two rotor cycles while the periods of reorientation to the next evolution position cancels across the same two rotor cycles.

Since only half the magnetization can be stored, there is a decrease in the signal-to-noise ratio by a factor of $\sqrt{2}$ for each pair of pulses (plus any due to T_1 relaxation). The experiment described here eliminates the problem of storage pulses by using π-pulses to refocus the evolution which occurs during the period of reorientation [62]. An experiment, labeled MAH-180, designed to produce a sideband-free MAS spectrum is shown in Fig. 3.1. The desired periods of evolution (shown in gray), at positions 120° degree apart, are sandwiched by π–pulses. As indicated in the figure, each π-pulse reverses the sign of the evolution such that the desired periods add while the undesired periods cancel. A minimum of two rotor cycles are needed to accomplish the refocusing

To show how this works for a quadrupolar nucleus, consider the experiment shown in Fig. 3.2. This experiment is assumed to occur over $2N$ rotor cycles of period τ_r for a total time of $2N\tau_r$. The first N cycles are divided into κ intervals so that each interval has a length of $N\tau_r/\kappa$. Each interval consists of a

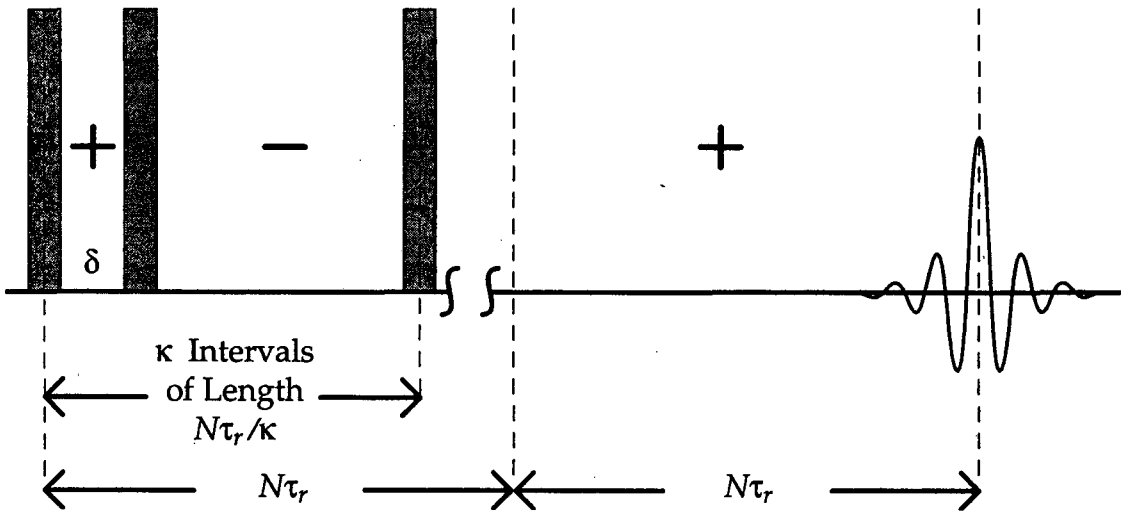

Figure 3.2 Experiment occurs over $2N$ rotor periods of length τ_r. The first N periods are divided into κ intervals of length $N\tau_r/\kappa$. Each interval consists of a period δ followed by a π-pulse which reverses the sign of the Hamiltonian. At the end of each interval a π-pulse restores the Hamiltonian to its original sign. The echo appears at $2N\tau_r$. The maximum value for δ is $\delta_{max} = N\tau_r/\kappa$.

period of evolution δ followed by a perfect π-pulse which reverses the sign of the evolution of the Hamiltonian.

The second-order quadrupolar frequency $\Omega_Q(t)$ of a sample spinning at ω_r about an axis oriented at an angle θ with respect to the magnetic field is given as

$$\Omega_Q(t) = \sum_{l=0,2,4} \sum_{m=-l}^{l} D_{m0}^{(l)}(\omega_r t + \gamma_r, \theta, 0)\mathcal{A}_{lm}^{Q}. \tag{3.3}$$

The initial phase of the rotor is γ_r and $\mathcal{A}_{lm}^{Q}$ is described in eqns (1.109) through (1.111). Since we will be integrating over time to obtain the phase of the signal, it is useful to separate the time-independent and time-dependent portions of eqn (3.3), which gives

$$\Omega_Q(t) = \sum_{l=0,2,4} d_{00}^{(l)}(\theta)\mathcal{A}_{l0}^{Q} + \sum_{l=2,4} \sum_{\substack{m=-l \\ m\neq 0}}^{l} D_{m0}^{(l)}(\omega_r t + \gamma_r, \theta, 0)\mathcal{A}_{lm}^{Q}. \tag{3.4}$$

The phase of the resulting signal obtained by integrating over time is then

$$\Phi_Q(\delta) = \sum_{j=0}^{\kappa-1}\left[\int_{N\tau_r j/\kappa}^{(N\tau_r j/\kappa)+\delta}\Omega_Q(t)dt - \int_{(N\tau_r j/\kappa)+\delta}^{(N\tau_r j/\kappa)+(N\tau_r/\kappa)}\Omega_Q(t)dt\right] + \int_{N\tau_r}^{2N\tau_r}\Omega_Q(t)dt. \quad (3.5)$$

In eqn (3.5), the negative sign before the second integral reflects the effects of the π-pulse. The integrals can be solved analytically, yielding

$$\Phi_Q(\delta) = 2\kappa\delta \sum_{l=0,2,4} d_{00}^{(l)}(\theta)\mathcal{A}_{l0}^{Q} + \sum_{l=2,4}\sum_{\substack{m=-l \\ m\neq 0}}^{l} e^{-im\gamma_r} d_{m0}^{(l)}(\theta)\mathcal{A}_{lm}^{Q}\left(2e^{-im\omega_r\delta} - e^{-im2\pi N/\kappa} - 1\right)\sum_{j=0}^{\kappa-1}\left(e^{-im2\pi N/\kappa}\right)^j \quad (3.6)$$

In eqn (3.6), we can see that the sidebands arise from the time-dependent terms $\exp(-im\omega_r\delta)$. If, then, we can render the time-dependent term in eqn (3.6) zero for all δ then, as a consequence, the sidebands would be eliminated. We must therefore examine under what conditions the second term in (3.6) is zero. First, note that

$$\sum_{j=0}^{\kappa-1}\left(e^{-im2\pi N/\kappa}\right)^j = e^{-i(\kappa-1)m\pi N/\kappa}\frac{\sin(-m\pi N)}{\sin(-m\pi N/\kappa)}. \quad (3.7)$$

This equation is zero when the following is true

$$\frac{\sin(-m\pi N)}{\sin(-m\pi N/\kappa)} = 0. \quad (3.8)$$

The solutions to this equation are

$$m\pi N = a\pi, \quad a = 0,\pm 1,\pm 2,\ldots \quad (3.9)$$

and

$$\frac{m\pi N}{\kappa} \neq b\pi, \quad b = 0,\pm 1,\pm 2,\ldots. \quad (3.10)$$

For the case of a quadrupolar nucleus, the maximum value of m is four, therefore for eqn (3.10) to always be true, κ must be greater than or equal to five. Also, N must be an integer to fulfill eqn (3.9) and not equal to a multiple of κ, or else eqn

(3.10) would fail to be true for all m. This means that the minimum experiment as shown in Fig. 3.2 for a quadrupolar nucleus would consist of five intervals and ten π-pulses. While this example specifically dealt with the quadrupolar Hamiltonian, these results also apply to a Hamiltonian that includes CSA since the maximum value of l (and therefore m) is two. If the nucleus is a spin-1/2 nucleus, κ must be only greater than or equal to three for a total of six π-pulses.

If the conditions of eqn (3.8) are met, the phase can be written (assuming $\kappa = 5$) as

$$\Phi_Q(\delta) = \left(\mathcal{A}_{00}^Q + d_{00}^{(2)}(\theta)\mathcal{A}_{20}^Q + d_{00}^{(4)}(\theta)\mathcal{A}_{40}^Q\right)10\delta \tag{3.11}$$

While there are no longer sidebands, there is anisotropy contained in the tensors $\mathcal{A}_{20}^Q$ and $\mathcal{A}_{40}^Q$. To remove this anisotropy, the standard DAS experiment described in Chapter 2 can be modified by combining it with above method to give an experiment called dynamic-angle hopping (DAH). As in DAS, the evolution occurs first at one angle θ_1 and after storing the magnetization and hopping to the second angle, further evolution occurs at a second angle θ_2. The ratio of the times spent at the two angles is determined by the constant k which also determines the two angles used. The presence of two evolution periods at two different angles complicates the DAH experiment since time dependence can be introduced into the Hamiltonian during both evolution periods. One method of dealing with this is to simply perform the ten π-pulse sequence at both angles, but this of course means the doubling of the number of pulses with the resulting loss of signal due to pulse imperfections. Theoretically, fewer pulses are needed over the two evolution periods but the relative phase of the rotor before and after the hop must be known; this is experimentally difficult to accomplish. However, by taking advantage of the $k = 5$ angle pair (0°, 64.43°), the π-pulse sequence only

needs to be performed when the rotor is at 64.43°. This is because spinning at 0° is equivalent to static conditions and therefore no time dependence is introduced and no sidebands produced. Also note that the angle 0° and five equally spaced positions around the axis 63.43° correspond to the various vertices of an icosahedron. Under the DAH experiment the phase becomes

$$\begin{aligned}\Phi_Q(\delta) = &\left(\mathcal{A}_{00}^Q + d_{00}^{(2)}(\theta_1)\mathcal{A}_{20}^Q + d_{00}^{(4)}(\theta_1)\mathcal{A}_{40}^Q\right)10\delta \\ &+\left(\mathcal{A}_{00}^Q + d_{00}^{(2)}(\theta_2)\mathcal{A}_{20}^Q + d_{00}^{(4)}(\theta_2)\mathcal{A}_{40}^Q\right)\frac{10\delta}{k}\end{aligned} \tag{3.12}$$

or, since $k = 5$,

$$\Phi(\delta) = \mathcal{A}_{00}^Q\, 12\delta\,. \tag{3.13}$$

Note that the experiment described above gives us a single point just as in DAS; the experiment must performed two-dimensionally, with the t_1 evolution time being $t_1 = 12\delta$. As can be seen in Fig. 3.2, the maximum value for $t_1/12$ is $N\tau_r/5$; therefore the maximum acquisition length in the t_1 dimension is $12N\tau_r/5$. This limit to the maximum value of t_1 can result in truncation artifacts if the full FID cannot be collected in the t_1 dimension. The number of rotor cycles that the experiment is performed over can be increased to allow for a longer acquisition time in the t_1 dimension; however, since the magnetization is in the transverse plane the entire length of the experiment, the loss in signal due to T_2 relaxation can be substantial.

Instead of using π-pulses, the DAH-90 experiment uses $\pi/2$ storage pulses as in the MAH experiments mentioned above. Each pair of storage pulses results in a loss of signal by a factor of $\sqrt{2}$ plus an additional loss of signal due to T_1 relaxation during the storage period. As a result the DAH-180 experiment is expected to be superior to the DAH-90 experiment because of the loss of signal due to the storage pulses. The phase cycling of the DAH-90 experiment is also much

more complicated because each of the $\pi/2$ pulses in the pulse train should be phase cycled, while in the DAH-180 experiment the π-pulses, if accurate, do not need phase cycling. In theory, the signal-to-noise of the DAH-180 spectrum should be identical to that of the standard DAS experiment given in Chapter 2 in the limit of infinite speed. It should also be superior to a method such as TOSS [59], which can result in a loss of signal-to-noise since the sideband intensity is not always folded into the isotropic peak. However, in practice, imperfections in the train of π-pulses can in itself lead to a loss of intensity in the DAH-180 experiment. Incomplete inversion due to resonant offset effects of the π-pulses can also lead to significant loss of intensity. Also the effects of T_2 relaxation can substantially reduce the signal-to-noise, since T_2 relaxation times tend to be short in many solids.

3.2 Experimental Results

Rubidium sulfate and lead nitrate were obtained from standard commercial sources. The ^{87}Rb experiments were performed at 9.4 T (130.89 MHz) and the ^{207}Pb experiments were performed at 11.7 T (104.25 MHz) using a home-built DAS probe described in reference [54]. The pulse sequences used for the DAH-180 and MAH-180 experiments are shown in Fig. 3.3. DAS experiments were performed as indicated in Chapter 2. The π-pulses were not phase cycled to reduce the length of the phase cycle. ^{87}Rb DAH-180 and DAS experiments were performed on Rb_2SO_4. The magic angle was set by detecting ^{81}Br present in a KBr internal standard, also obtained from standard commercial sources. The spectra were referenced relative to a 1 M $RbNO_3$ solution. Rubidium $\pi/2$ pulse widths selective for the central transition were 4.7 μs. Recycle delays of 2 s were used to allow for relaxation and to allow the spinning speed to stabilize after the

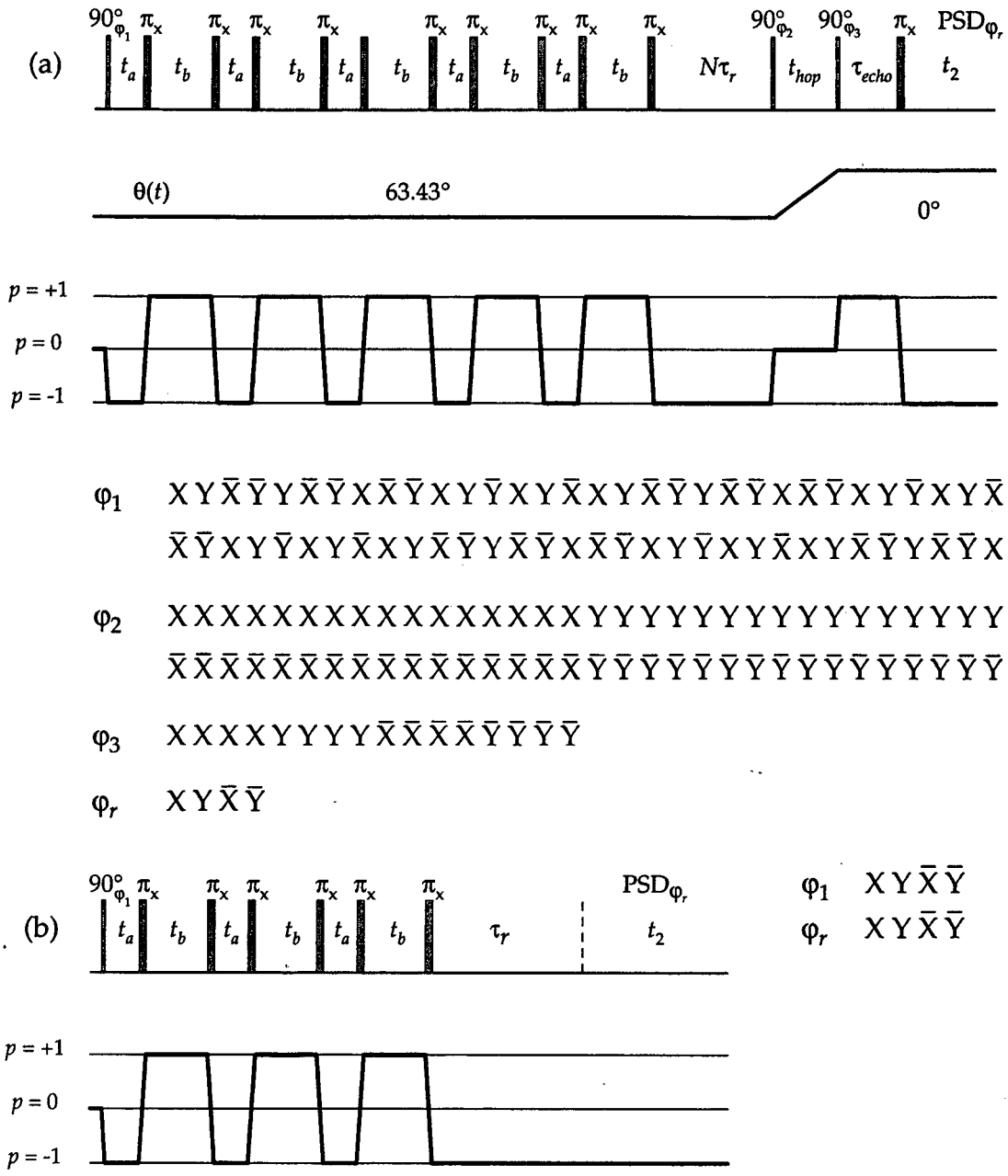

Figure 3.3 Pulse sequences for the (a) DAH and (b) MAH experiments. In (a) $t_a = t_1/12$ and $t_b = (N\tau_r/5) - (t_1/12)$ and in (b) $t_a = t_1/6$ and $t_b = (N\tau_r/3) - (t_1/6)$ where $2N$ is the number of rotor and τ_r is the spinning period. In (a), t_{hop} is the hop time need for sample reorientation and t_{echo} is the dephasing time needed to form a Hahn-echo. $\theta(t)$ indicates the angle the spinning axis forms with respect to the magnetic field. Subscripts indicate the phase of the pulses and PSD refers to phase-sensitive detection.

hop to the initial angle. We have found that this delay is crucial since significant variations in spinning speed due to the disruption caused by the hop may lead to a loss of signal-to-noise and resolution. The hop time was 55 ms. For both DAH-180 and DAS experiments, 256 complex points were acquired in t_2. For the DAH-180 experiment, 49 were acquired in t_1, and for the DAS experiment, 68 were acquired in t_1. The dwell time in t_2 was 16 μs and in t_1 was 33.6 μs. 512 transients were acquired for each t_1 point. Whole-echo acquisition was used to obtain pure-absorption mode two-dimensional spectra [42,63]. The rotor period for the DAH-180 experiment was 199.6 μs (5.0 kHz). For the DAS experiment, the spinning frequency was 1.8 kHz. The rotor period was monitored during the DAH experiment by observing the piezoelectric signal from the vibrations of the spinner detected with a wire attached to the stator housing. The DAH-180 experiment was performed over eight rotor cycles ($N = 4$).

^{207}Pb MAH-180 with a hop to 0° was performed on $PbNO_3$. Lead $\pi/2$ pulse widths were 11 μs. A recycle delay of 10.2 s was used. The hop time was 75 ms. 256 complex points were acquired in t_2 and 64 were acquired in t_1. The dwell time was 40 μs in t_1 and 50 μs in t_2. 128 transients were acquired. Whole-echo acquisition was used to obtain pure-absorption mode 2D spectra. The rotor period was 1326.67 μs. The experiment was performed over two rotor cycles ($N = 1$).

The two-dimensional spectrum of rubidium sulfate taken with the DAH-180 sequence in Fig. 3.3a is shown in Fig. 3.4. The projection of the isotropic dimension is shown in Fig. 3.5b. The two sites occur at -25 ppm and 28 ppm in agreement with previous studies at 9.4 T presented in Chapter 2 [33]. As expected, a sideband-free isotropic dimension is observed, correlated with an anisotropic dimension consisting of the separated static powder patterns for the

individual sites. Since detection occurs under static conditions no sidebands are observed in the second dimension. Truncation artifacts are present in the t_1 dimension since the maximum allowed value for t_1 was not sufficient to collect the full FID in the t_1 dimension. The projection of the isotropic dimension of the standard DAS experiment is shown in Fig. 3.5a. The site at -25 ppm has a large number of sidebands reducing the intensity of the isotropic position by a signifi-

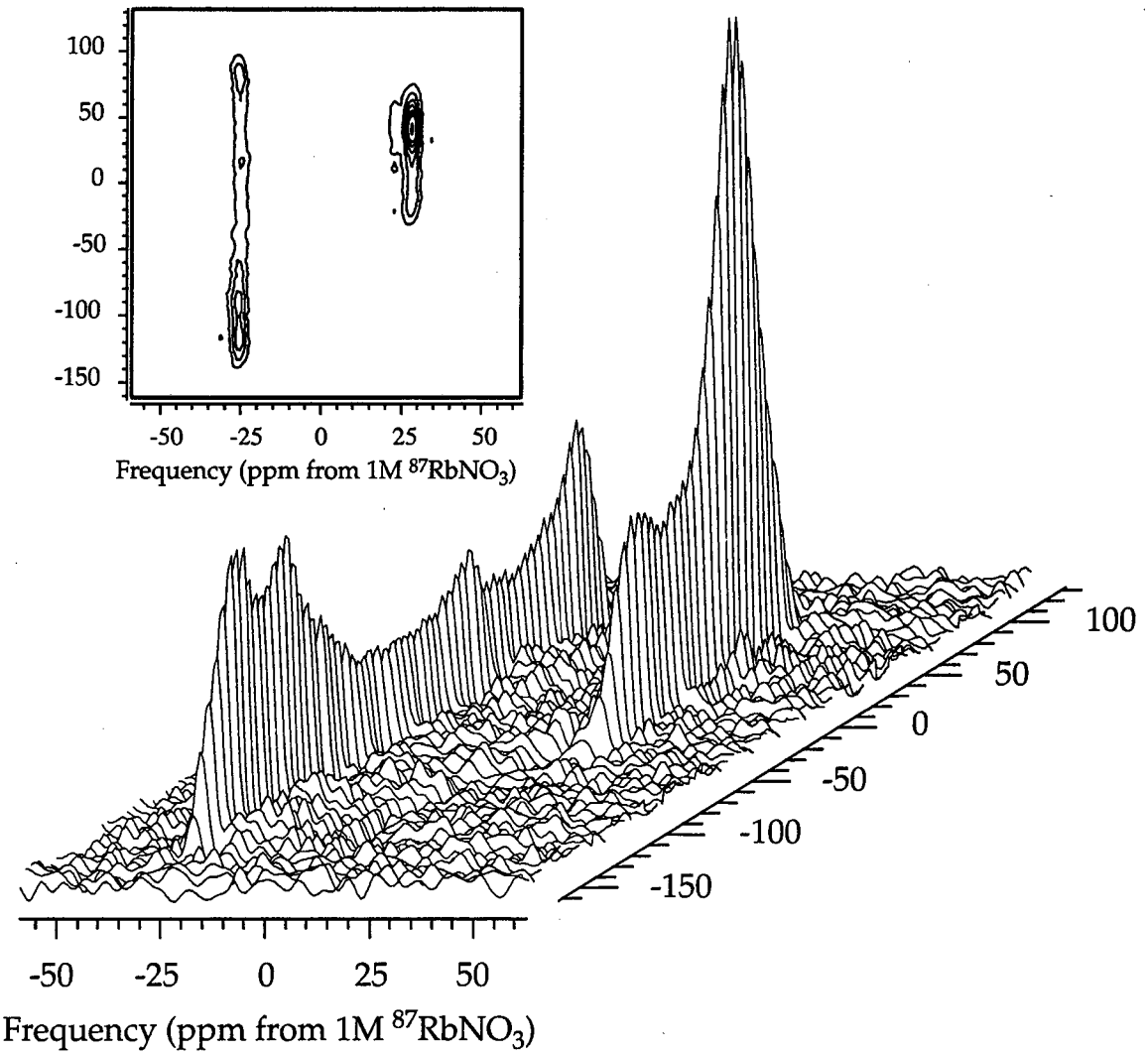

Figure 3.4 DAH-180 spectra of ^{87}Rb in Rb_2SO_4 acquired at 9.4 T using the sequence in Fig. 3.3a. Both the contour and stacked plot show that the spectra are free from sidebands.

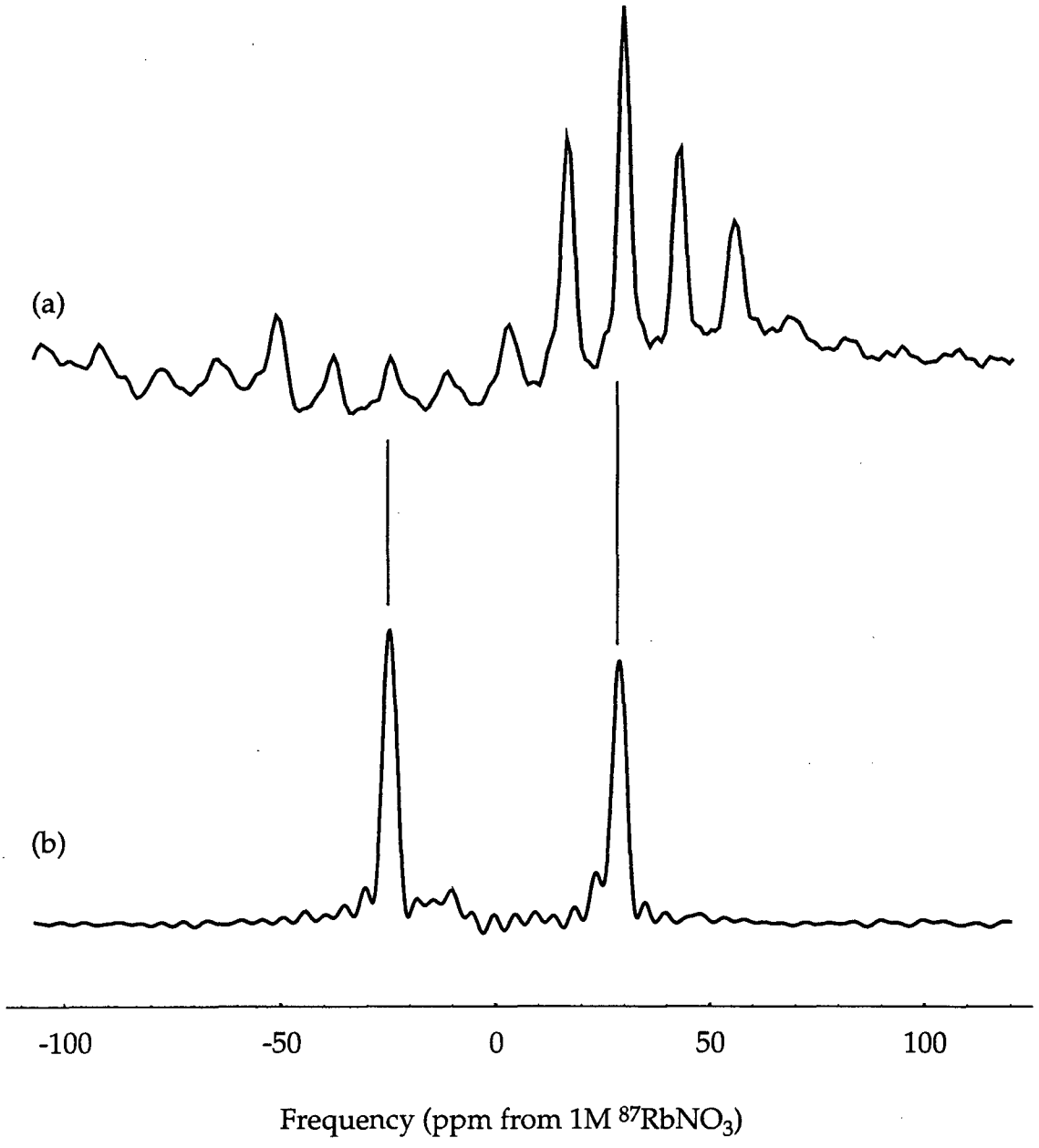

Figure 3.5 Isotropic projections of (a) DAS and (b) DAH spectra of Rb2SO4 taken at 9.4 T. The isotropic peak positions are at -25 ppm and 29 ppm. The DAS spectra in (a), take with a spinning frequency of 1.8 kHz, shows multiple sidebands and a corresponding loss of intensity in the isotropic peaks. In contrast the DAH-180 spectrum exhibits no sidebands and the isotropic peaks appear at full intensity. The spectrum does exhibit some truncation artifacts due to the limitations on the maximum value of t_1 in the DAH-180 experiment.

cant amount. In contrast, the same peak in the DAH spectrum is clearly resolved, and, in fact, the two sites show the expected 1:1 intensity [51]. As an example of the MAH-180, in Fig. 3.6 is shown the two-dimensional spectrum of lead nitrate taken with both the MAH-180 pulse sequence given in Fig. 3.3b and with a MAH-180 pulse sequence followed by a hop to 0° for detection. $PbNO_3$ has a long T_2 and the spectrum breaks into sidebands at very low spinning speeds as shown in Fig. 3.6a. However, by following the MAH-180 sequence with a hop to 0° for detection the isotropic sideband-free dimension is correlated to the static powder pattern (Fig. 3.6b). Again truncation artifacts are present. Slight distortions are present in the lineshape and are probably due to cumulative effects of imperfect π–pulses.

3.3 Sidebands in Double Rotation NMR

An obvious question would be whether this method of removing sidebands can be applied to double rotation NMR (DOR), an experiment mentioned in Chapter 2. The problem of sidebands is more acute in DOR experiments due to the large size that is needed for the outer rotor. (For a detailed analysis of DOR sidebands see references [64,65]. Typically, the speed of the outer rotor is limited at most to few kilohertz, leading to the almost inevitable presence of sidebands for a typical sample. There are methods that will allow the suppression of the odd order sidebands of the outer rotor [35,65-70]. It would be preferable, however, to eliminate the sidebands completely without any reduction in signal-to-noise.

To analyze whether the procedure of using π-pulses to remove sidebands will work in the case of DOR, the same procedure will be followed as above in the analysis of DAH. The basic experiment is again give in Fig. 3.2. In the case of

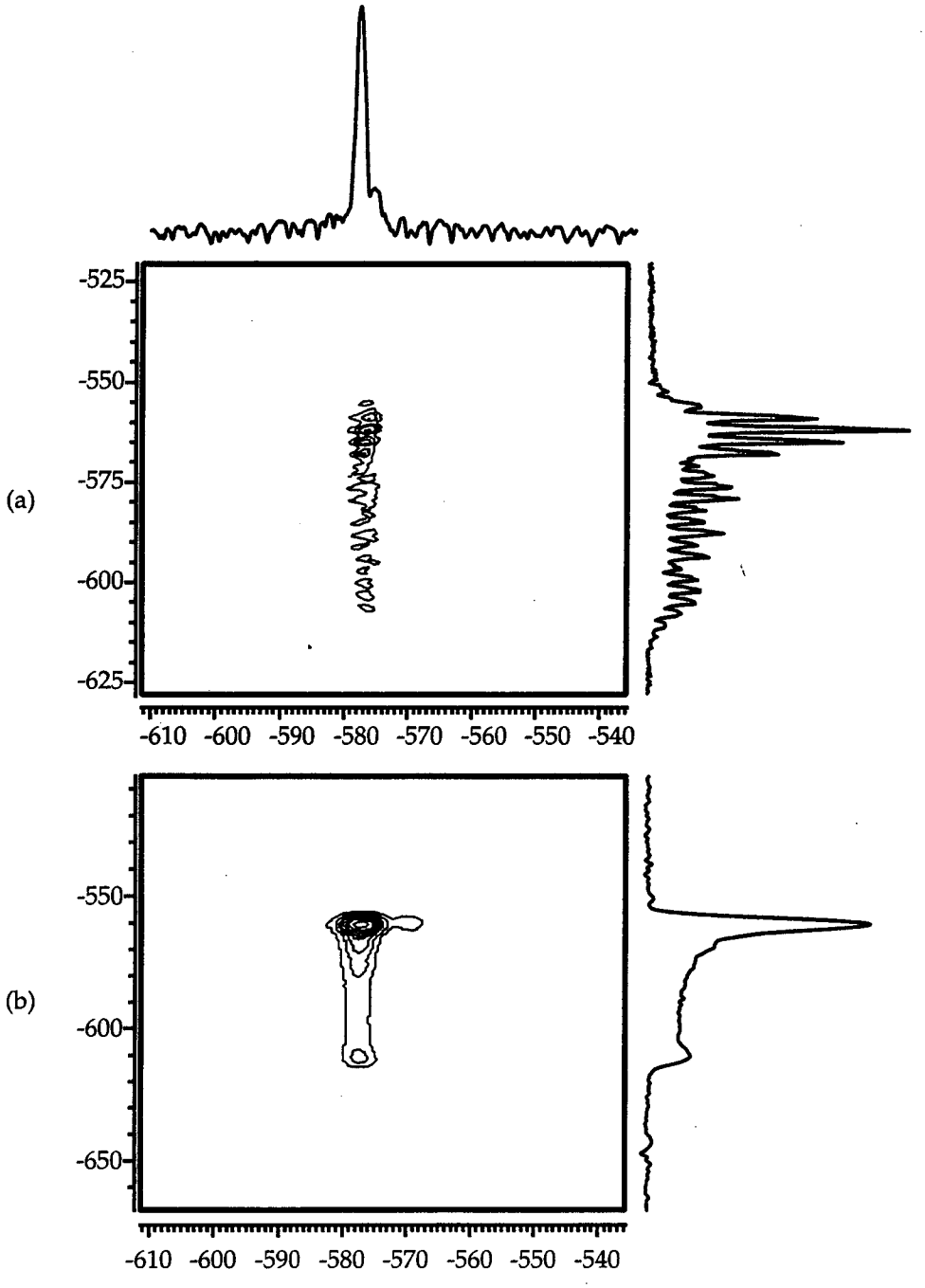

Figure 3.6 ^{207}Pb MAH-180 two-dimensional spectra at 11.7 T of $PbNO_3$ (a) with detection at the magic angle and a spinning speed of 300 Hz and (b) followed by a hop to 0° for detection with a spinning speed of 750 Hz. In (a), the sideband free isotropic spectra is correlated to the MAS spectrum which exhibits sidebands. In (b), the isotropic spectrum is correlated to the static powder spectrum.

DOR, we have two rotor frequencies ω_1 and ω_2. We will assume that $\omega_2 = f\omega_1$ so that ω_1 corresponds to the outer rotor and ω_2 corresponds to the inner rotor. Since we must perform the sequence in Fig. 3.2 over complete rotor cycles, τ_r equals the slowest rotor period τ_1. The two DOR angles will be labeled θ_1 and θ_2 and the initial phase of the rotors will be labeled γ. The second-order quadrupolar frequency of a sample under double rotations may be written

$$\Omega_{DOR}(t) = \sum_{l=0,2,4} \sum_{m,n=-l}^{l} D^{(l)}_{m0}(\omega_1 t, \theta_1, 0) D^{(l)}_{nm}(\omega_2 t, \theta_2, \gamma) \mathcal{A}^Q_{ln}. \tag{3.14}$$

As in the above derivation of DAH, we will separate out the time-independent components of eqn (3.14). To do so, we must recognize that not only does the conditions $m = n = 0$ yield time-independent terms, but the condition $m = -fn$ as well. We can see this by expanding the two Wigner rotation matrices:

$$D^{(l)}_{m0}(\omega_1 t, \theta_1, 0) D^{(l)}_{nm}(\omega_2 t, \theta_2, \gamma) = e^{-i(m\omega_1 + n\omega_2)t} e^{-im\gamma} d^{(l)}_{m0}(\theta_1) d^{(l)}_{nm}(\theta_2). \tag{3.15}$$

Separating the time-independent from the time-dependent terms, we have

$$\begin{aligned} \Omega_{DOR}(t) = & \sum_{l=0,2,4} d^{(l)}_{00}(\theta_1) d^{(l)}_{00}(\theta_2) \mathcal{A}_{l0} + \sum_{l=0,2,4} \sum_{n=-l}^{l} d^{(l)}_{-fn,0}(\theta_1) d^{(l)}_{n,-fn}(\theta_2) \mathcal{A}_{ln} \\ & + \sum_{l=0,2,4} \sum_{\substack{m,n=-l \\ m,n\neq 0 \\ m\neq -fn}}^{l} D^{(l)}_{m0}(\omega_1 t + \alpha_1, \theta_1, 0) D^{(l)}_{nm}(\omega_2 t, \theta_2, \gamma) \mathcal{A}_{ln}. \end{aligned} \tag{3.16}$$

Performing the integration in eqn (3.5) using the expression for the frequency in eqn (3.16), gives

$$\begin{aligned} \Phi_Q(t) = & 2\kappa\delta \sum_{l=0,2,4} d^{(l)}_{00}(\theta_1) d^{(l)}_{00}(\theta_2) \mathcal{A}_{l0} + 2\kappa\delta \sum_{l=0,2,4} \sum_{n=-l}^{l} d^{(l)}_{-fn,0}(\theta_1) d^{(l)}_{n,-fn}(\theta_2) \mathcal{A}_{ln} \\ & - \sum_{l=0,2,4} \sum_{\substack{m,n=-l \\ m,n\neq 0 \\ m\neq -fn}}^{l} \frac{i\mathcal{A}_{ln}}{(m\omega_1 + n\omega_2)} d^{(l)}_{m0}(\theta_1) d^{(l)}_{nm}(\theta_2) e^{-im\gamma} \\ & \times \left\{ \left[2e^{-i\omega_1(m+fn)\delta} - e^{-i2\pi N(m+fn)/\kappa} - 1 \right] \sum_{j=0}^{\kappa-1} \left(e^{-i2\pi N(m+fn)/\kappa} \right)^j \right. \\ & \left. - e^{-i(m\omega_1 + n\omega_2)2N\tau_r} - e^{-i(m\omega_1 + n\omega_2)N\tau_r} \right\}. \end{aligned} \tag{3.17}$$

In eqn (3.17), the term $\exp\left(-i\omega_1(m+fn)\delta\right)$ leads to sidebands, and to eliminate them, we need to find the conditions for which the sum over j is zero for all δ. Performing the summation over j results in

$$\sum_{j=0}^{\kappa-1}\left(e^{-i2\pi N(m+fn)/\kappa}\right)^j = e^{-i(\kappa-1)\pi N(m+fn)/\kappa}\frac{\sin\left(-\pi N(m+fn)\right)}{\sin\left(-\pi N(m+fn)/\kappa\right)}. \tag{3.18}$$

The solutions to the equation

$$\frac{\sin\left(-\pi N(m+fn)\right)}{\sin\left(-\pi N(m+fn)/\kappa\right)} = 0 \tag{3.19}$$

are

$$\pi N(m+fn) = a\pi, \quad a = 0,\pm1,\pm2,\ldots \tag{3.20}$$

and

$$\frac{\pi N(m+fn)}{\kappa} \neq b\pi, \quad b = 0,\pm1,\pm2,\ldots. \tag{3.21}$$

The second time-independent term in eqn (3.17), generated when $m=-fn$, contains quadrupolar anisotropy in the form of the $\mathcal{A}_{4n}$'s. However, the maximum allowed value for m is $|m_{max}|=4$; therefore, as long as the ratio of the speeds of the inner rotor to the outer is greater than four, the second term vanishes. In order to fulfill eqn (3.20) and to eliminate the anisotropy, the minimum allowed value for f is five. If we use $\kappa = 5$, as in the case of the DAH experiment, along with $f = 5$, then we find that eqn (3.21) is fulfilled for all values of m except $m = 0$, eliminating any sidebands arising from the spinning of the outer rotor. However, when $m = 0$, the time-dependent term in eqn (3.17) no longer vanishes and noting that the total evolution time in the t_1 dimension is $t_1 = 2\kappa\delta$, we find that the term that generates sidebands, $\exp\left(-i\omega_1(m+fn)\delta\right)$, now reduces to

$$e^{-i\omega_1(m+fn)\delta}\Big|_{m=0} \rightarrow e^{-in\omega_2 t_1/10}. \tag{3.22}$$

The implication of eqn (3.22) is that, while the sidebands arising from the

outer rotor have disappeared, the inner rotor appears to be spinning at *one-tenth* its actual speed. Since we are assuming that the inner rotor is spinning five times faster than the outer rotor, we have actually increased the number of sidebands appearing in the spectrum. If we wish to completely remove the sidebands in the DOR spectrum, we can see using eqn (3.21) that since the maximum values of m and n are four and $f = 5$ in our example, κ must be equal to or greater than twenty-five. Therefore, a train of at least fifty π-pulses is needed to produce a sideband-free isotropic spectrum.

A further comment is necessary about the above derivation. It was assumed that the inner rotor was spinning an integral number of times faster than the outer rotor. In practice, the ratio of the outer and inner rotors is determined by the design of the DOR probe [34,35] and, for a given probe, adjusting the two speeds so that eqns (3.20) and (3.21) are satisfied for reasonable value of N and κ will quite likely prove impossible.

Chapter 4
Cross-Polarization Dynamic-Angle Spinning

4.1 Introduction

Significant increases in NMR sensitivity can be achieved by transferring high nuclear spin polarization between inequivalent nuclei using cross polarization (CP) techniques [71,72]. In addition, selective CP transfer can be applied as a useful tool for spectral editing [73-80]. While CP is a very effective technique for static samples, the combination of CP with sample spinning NMR techniques from a number of difficulties. One of these difficulties is that the dipolar spin interactions that mediate the CP transfer become time dependent under magic-angle spinning (MAS), making the Hartmann-Hahn matching conditions more complicated and also reducing the efficiency of the polarization transfer [81]. In Chapter 5, the effects of MAS on cross-polarization will be examined more closely. Another difficulty arises when cross polarizing the central transition of half-integer quadrupolar nuclei. In this situation, the time-dependence of the large first-order quadrupolar interaction interferes with the Hartmann-Hahn matching [82,83]. However, by using the techniques of dynamic-angle spinning, the problem can be eliminated by exploiting the time independence of the spin eigenvalues when spinning at 0° (parallel) with respect to the external magnetic field. By performing cross polarization while spinning at 0°, the full static CP intensity can be obtained and used in a MAS, variable-angle spinning (VAS) or DAS experiment [56]. First, the problem of cross-polarizing quadrupolar nuclei

will be presented and then experimental results will be shown.

4.2 Theoretical Background

This is a condensed treatment of a detailed treatment by Vega [82,83] of the theory of spin locking and cross polarization of the central transition of a half-odd integer spin nucleus. Consider a cross-polarization experiment in which polarization is transferred from a spin $I = 1/2$ to a quadrupolar nucleus $S = 3/2$. The secular Hamiltonian in the rotating frame can be written as

$$H(t) = H_{RF} + H_D(t) + H_Q(t) \tag{4.1}$$

where the rf Hamiltonian is given using eqn (1.146) as

$$H_{RF} = -\hbar\omega_{1I} I_x - \hbar\omega_{1S} S_x, \tag{4.2}$$

the dipolar Hamiltonian is given using eqn (1.143) by

$$H_D(t) = \hbar\omega_D A_{20}^D(t) 2 I_z S_z, \tag{4.3}$$

and the quadrupolar Hamiltonian is given using eqn (1.95) by

$$H_Q = \hbar\omega_Q A_{20}^Q T_{20} = \frac{\hbar\omega_Q}{\sqrt{6}} A_{20}^Q \left(3I_z^2 - I^2\right). \tag{4.4}$$

The nutation frequency ω_{nut} for the central transition of a quadrupolar nucleus with a spin S in the presence of a large quadrupolar interaction [2,84-86] is

$$\omega_{nut} = (S + 1/2)\gamma_S B_{1S}. \tag{4.5}$$

This leads to a Hartmann-Hahn match condition for a spin-1/2 and a spin-3/2 of

$$\gamma_I B_{1I} = 2\gamma_S B_{1S};\ \omega_{1I} = 2\omega_{1S}. \tag{4.6}$$

In order to simplify the following calculations, it is necessary to rewrite the Hamiltonian in eqn (4.1) using fictitious spin-1/2 operators (see eqns (1.20) to (1.22)) as

$$
\begin{aligned}
H(t) = &-\hbar\omega_{1I}I_x - \sqrt{3}\hbar\omega_{1S}\left(S_x^{1-2} + S_x^{3-4}\right) - 2\hbar\omega_{1S}S_x^{2-3} \\
&+\omega_Q A_{20}^Q(t)\left(S_z^{1-2} - S_z^{3-4}\right) \\
&+3\omega_D A_{20}^D(t)2I_zS_z^{1-4} + \omega_D A_{20}^D(t)2I_zS_z^{2-3}
\end{aligned}
\tag{4.7}
$$

To diagonalize $H_{RF} + H_Q(t)$, we assume that $|\omega_{1I}|, |\omega_{1S}| \gg |\omega_D|$ and transform the Hamiltonian into a time-dependent frame [85]. The function, $W(t)$, that performs this transformation is

$$
\begin{aligned}
W(t) = &\exp\left(-i\frac{\pi}{2}I_y\right)\exp\left(i\frac{\pi}{2}S_y^{1-4}\right)\exp\left(-i\frac{\pi}{2}S_y^{2-3}\right) \\
&\times\exp\left(i2\xi_1(t)S_y^{1-3}\right)\exp\left(i2\xi_2(t)S_y^{2-4}\right),
\end{aligned}
\tag{4.8}
$$

where $0 \le \{\xi_1(t), \xi_2(t)\} \le \pi/2$,

$$
\tan 2\xi_1(t) = \frac{\sqrt{3}\omega_{1S}}{-\omega_Q A_{20}^Q(t) + \omega_{1S}} \tag{4.9}
$$

and

$$
\tan 2\xi_2(t) = \frac{\sqrt{3}\omega_{1S}}{-\omega_Q A_{20}^Q(t) - \omega_{1S}}. \tag{4.10}
$$

In the rotating frame a given operator $\tilde{O}(t)$ can be calculated using

$$
\tilde{O}(t) = W^\dagger(t)O(t)W(t). \tag{4.11}
$$

Therefore, the Hamiltonian in this time-dependent frame $\tilde{H}(t)$ is given by

$$
\tilde{H}(t) = W^\dagger(t)H(t)W(t) \tag{4.12}
$$

becoming

$$
\begin{aligned}
\tilde{H}(t) = &-\omega_{1I}I_z + \omega_{1S}\left(S_z^{1-4} - S_z^{2-3}\right) - \omega^{1-3}(t)S_z^{1-3} - \omega^{2-4}(t)S_z^{2-4} \\
&-b_{IS}^{1-4}(t)2I_xS_x^{1-4} + b_{IS}^{2-3}(t)2I_xS_x^{2-3} - b_{IS}^{1-2}(t)2I_xS_x^{1-2} - b_{IS}^{3-4}(t)2I_xS_x^{3-4},
\end{aligned}
\tag{4.13}
$$

where

$$
\omega^{1-3}(t) = \sqrt{3\omega_{1S}^2 + \left(\omega_Q A_{20}^Q(t) - \omega_{1S}\right)^2} = \frac{-\omega_Q A_{20}^Q(t) + \omega_{1S}}{\cos 2\xi_1(t)}, \tag{4.14}
$$

$$\omega^{2-4}(t) = -\sqrt{3\omega_{1S}^2 + \left(\omega_Q A_{20}^Q(t) + \omega_{1S}\right)^2} = \frac{\omega_Q A_{20}^Q(t) + \omega_{1S}}{\cos 2\xi_2(t)}, \tag{4.15}$$

$$b_{IS}^{1-4}(t) = \omega_D A_{20}^D(t)\left\{2\cos\left(\xi_1(t) - \xi_2(t)\right) + \cos\left(\xi_1(t) + \xi_2(t)\right)\right\}, \tag{4.16}$$

$$b_{IS}^{1-2}(t) = \omega_D A_{20}^D(t)\left\{2\sin\left(\xi_1(t) - \xi_2(t)\right) - \sin\left(\xi_1(t) + \xi_2(t)\right)\right\}, \tag{4.17}$$

$$b_{IS}^{2-3}(t) = \omega_D A_{20}^D(t)\left\{2\cos\left(\xi_1(t) - \xi_2(t)\right) - \cos\left(\xi_1(t) + \xi_2(t)\right)\right\}, \tag{4.18}$$

and

$$b_{IS}^{3-4}(t) = \omega_D A_{20}^D(t)\left\{2\sin\left(\xi_1(t) - \xi_2(t)\right) + \sin\left(\xi_1(t) + \xi_2(t)\right)\right\}. \tag{4.19}$$

The observable $\langle S_+(t)\rangle$ of interest can be calculated using eqn (1.8),

$$\langle S_+(t)\rangle = \mathrm{Tr}\{\sigma(t) S_+\}. \tag{4.20}$$

Ignoring the effects of relaxation, the time evolution of the density matrix $\sigma(t)$ is given by (see eqn (1.15))

$$\sigma(t) = U(t)\sigma(0)U^\dagger(t);\ U(t) = T\exp\left(-i\int_0^t H(s)ds\right). \tag{4.21}$$

The propagator in the rotating frame is given by

$$\tilde{U}(t) = T\exp\left\{-i\int_0^t \left[\tilde{H}(t') - i\dot{W}^\dagger(t')W(t')\right]dt'\right\} \tag{4.22}$$

where

$$i\dot{W}^\dagger(t)W(t) = 2\frac{d\xi_1(t)}{dt}S_y^{1-3} + 2\frac{d\xi_2(t)}{dt}S_y^{2-4} \tag{4.23}$$

The derivatives are related to $A_{20}^Q(t)$ by

$$2\frac{d\xi_1(t)}{dt} = \frac{\sqrt{3}\omega_1\omega_Q}{\left(-\omega_Q A_{20}^Q(t) + \omega_{1S}\right)^2 + 3\omega_{1S}^2}\frac{dA_{20}^Q(t)}{dt} \tag{4.24}$$

and

$$2\frac{d\xi_2(t)}{dt} = \frac{\sqrt{3}\omega_1\omega_Q}{\left(\omega_Q A_{20}^Q(t) + \omega_{1S}\right)^2 + 3\omega_{1S}^2}\frac{dA_{20}^Q(t)}{dt}. \tag{4.25}$$

The propagator $U(t)$ in the original frame is related to the propagator $\tilde{U}(t)$ in the rotating frame by

$$U(t) = W(t)\tilde{U}(t)W^{\dagger}(0). \tag{4.26}$$

Therefore, the observable $\langle S_+(t)\rangle$ from eqn (4.20) can be expressed as

$$\langle S_+(t)\rangle = tr\left[\tilde{U}(t)\tilde{\sigma}(0)\tilde{U}^{\dagger}(t)\tilde{S}_+\right] \tag{4.27}$$

where

$$\begin{aligned}
\tilde{S}_+ = {} & S_z^{2-3}\cos^2\xi_1(t)\cos^2\xi_2(t) + S_z^{1-3}\sin 2\xi_1(t) \\
& - S_z^{1-4}\sin^2\xi_1(t)\sin^2\xi_2(t) - S_z^{2-4}\sin 2\xi_2(t) \\
& - S_z^{1-2}\sin^2\xi_1(t)\cos^2\xi_2(t) - S_z^{3-4}\cos^2\xi_1(t)\sin^2\xi_2(t) \\
& + S_x^{1-3}\left[\cos\xi_1(t)\sin\xi_1(t) - \cos 2\xi_1(t)\right] \\
& + S_x^{2-4}\left[\cos\xi_2(t)\sin\xi_2(t) + \cos 2\xi_2(t)\right] \\
& + iS_y^{1-2}\left[\sin\xi_1(t)\cos\xi_2(t) + \cos\left(\xi_1(t) - \xi_2(t)\right)\right] \\
& + iS_y^{3-4}\left[\cos\left(\xi_1(t) - \xi_2(t)\right) - \cos\xi_1(t)\sin\xi_2(t)\right] \\
& + iS_y^{1-4}\left[\sin\xi_1(t)\sin\xi_2(t) - \sin\left(\xi_1(t) - \xi_2(t)\right)\right] \\
& + iS_y^{2-3}\left[\cos\xi_1(t)\cos\xi_2(t) - \sin\left(\xi_1(t) - \xi_2(t)\right)\right].
\end{aligned} \tag{4.28}$$

The initial density matrix in a typical experiment after an initial $\pi/2$ pulse on the I spin is $\sigma(0) = I_x$; using eqn (4.11), the initial density operator in the rotating frame becomes $\tilde{\sigma}(0) = I_z$.

To calculate $\tilde{U}(t)$ it is necessary to evaluate eqn (4.22). The Dyson time-ordering operator T makes the evaluation of the integral difficult since the integrand does commute with itself at all times. However, certain approximations can be made by examining the relative size of the two terms in the Hamiltonian. In Fig. 4.1 the functions $\xi_1(t)$ and $\xi_2(t)$ are plotted for a typical crystallite. For a majority of the rotor cycle, both functions have values close to either 0 or $\pi/2$. The abrupt transition between the two values occurs as the quadrupolar cou-

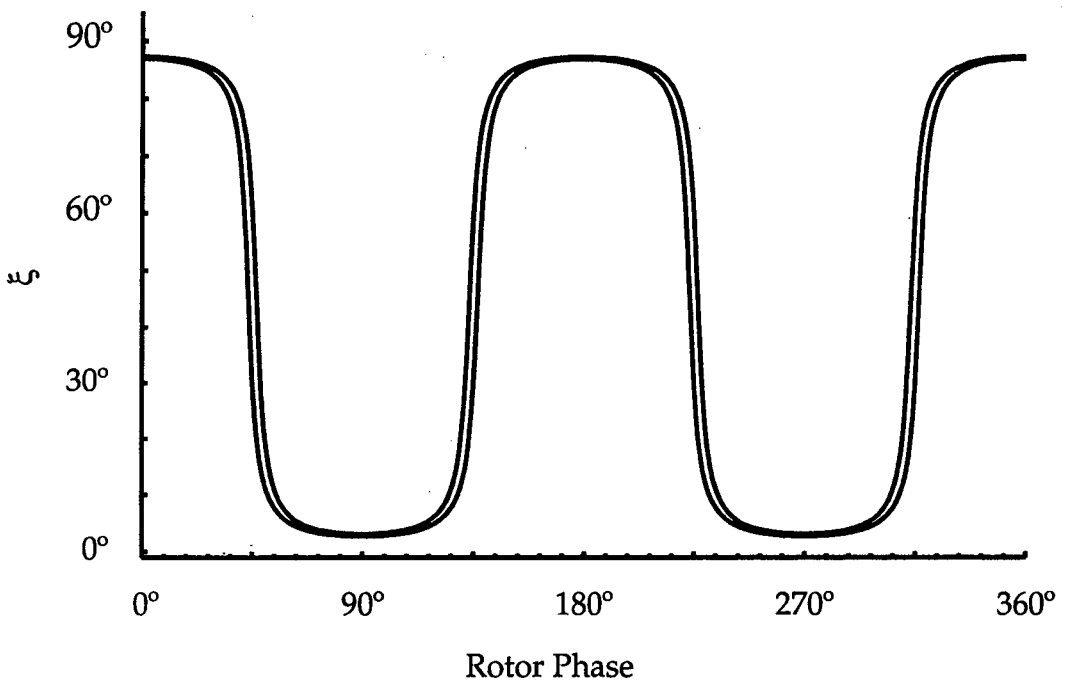

Figure 4.1 ξ_1 and ξ_2 *vs.* rotor phase for a typical crystallite under MAS with a PAS oriented perpendicular to the rotor, e^2qQ/h = 11 MHz and η = 0.0.

pling passes through zero. As a result, the Hamiltonian in eqn (4.13) can be written as either

$$\tilde{H}(\xi \approx 0) \approx -\omega_{1I} I_z - 2\omega_{1S} S_z^{2-3} + \omega_Q \left(S_{00}^{1-4} - S_{00}^{2-3} \right) - 6\omega_D A_{20}^D(t) I_x S_x^{1-4} + 2\omega_D A_{20}^D(t) I_x S_x^{2-3} \tag{4.29}$$

or

$$\tilde{H}\left(\xi \approx \frac{\pi}{2} \right) \approx -\omega_{1I} I_z + 2\omega_{1S} S_z^{1-4} - \omega_Q \left(S_{00}^{1-4} - S_{00}^{2-3} \right) - 2\omega_D A_{20}^D(t) I_x S_x^{1-4} + 6\omega_D A_{20}^D(t) I_x S_x^{2-3}. \tag{4.30}$$

It is also necessary to consider the nature of the passage of $Q(t)$ through zero. Fig. 4.2 shows a schematic of the eigenvalues of a spin-3/2 nucleus under spin-locking conditions; we can use this to predict the effects on various eigenstates as $Q(t)$ oscillates through zero. If the change in $Q(t)$ is slow, the passage is

considered adiabatic, and the population of the original states change along with the quadrupolar coupling ($|C\pm\rangle \leftrightarrow |\pm 3/2\rangle$). If the change in $Q(t)$ is fast, the passage is considered sudden and there is no change in state. The third possibility is the intermediate regime which is more difficult to describe but in general results in the creation of non-spinlocked states.

In terms of our previous calculations, the adiabatic approximation is applicable when $|\tilde{H}(t)| \gg |\dot{W}^{\dagger}(t)W(t)|$ and the sudden approximation holds when

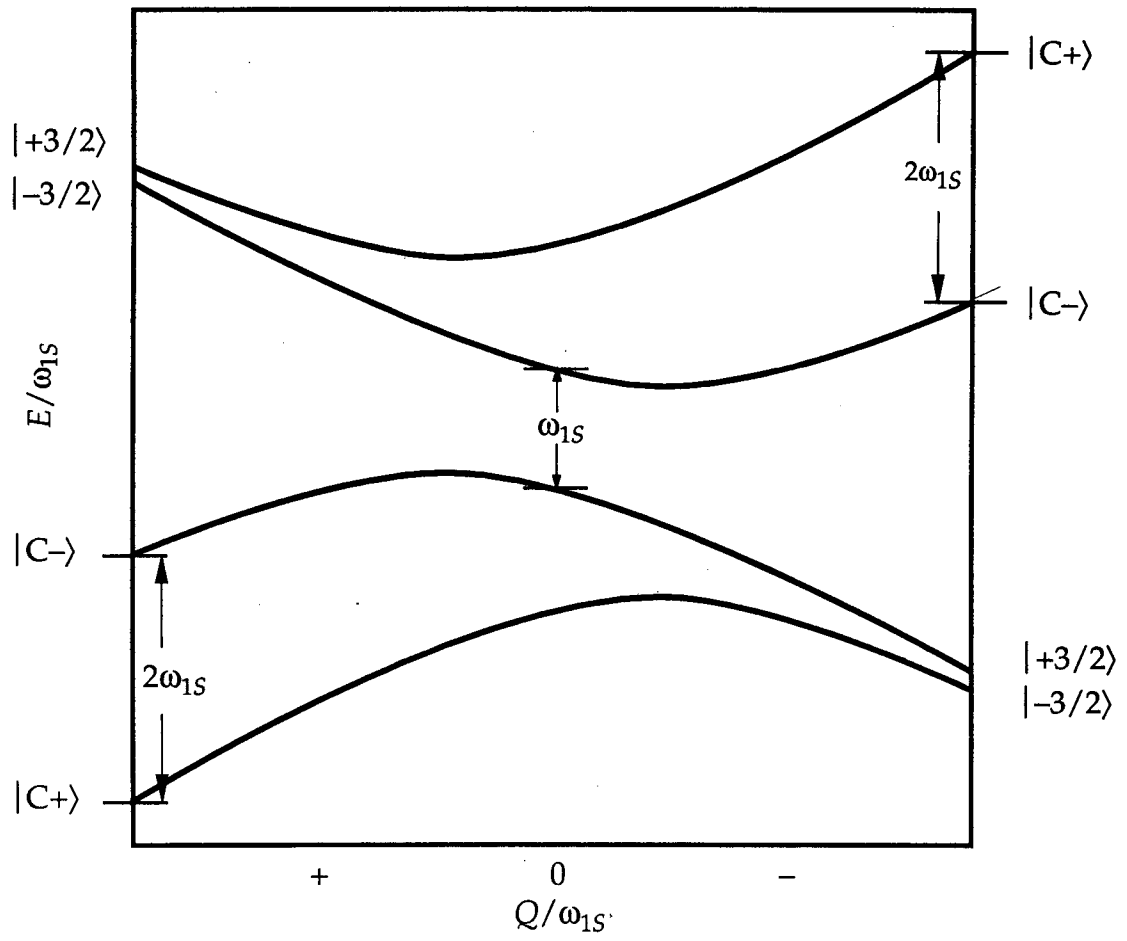

Figure 4.2 Eigenvalues E of a quadrupolar nucleus with $S = 3/2$ and Hamiltonian $H_Q + H_{RF}$ *vs.* the ratio $Q(t)/\omega_{1S}$. The eigenstates are indicated for $Q(t) \gg \omega_{1S}$ where $|C\pm\rangle = \left(|1/2\rangle \pm |-1/2\rangle\right)/\sqrt{2}$ corresponding to the central transition and $|\pm 3/2\rangle$ corresponding to the triple quantum transitions.

$\left|\tilde{H}(t)\right| \ll \left|\dot{W}^{\dagger}(t)W(t)\right|$. The relative intensity of $\tilde{H}(t)$ *vs.* $\dot{W}^{\dagger}(t)W(t)$ is shown in Fig. 4.3a and c. If the adiabatic approximation holds when $A_{20}^{Q}(t)$ passes through the extremum in $\dot{W}^{\dagger}(t)W(t)$, the level crossing is avoided and the propagator for all times can be written

$$\tilde{U}_{adiabatic}(t) = \exp\left[-i\int_0^t \tilde{H}(t')dt'\right] \tag{4.31}$$

If we assume a crystallite initially starts with $\xi_1 \approx \xi_2 \approx 0$, and if the Hartmann-Hahn matching condition of $\omega_{1I} = (S+1/2)\omega_{1S}$ is being fulfilled then evolution of the density matrix, $\tilde{\sigma}(0) = I_z$, under the Hamiltonian in eqn (4.29) leads to

$$\tilde{\sigma}(t) = \tilde{U}_{adiabatic}(t)\tilde{\sigma}(0)\tilde{U}_{adiabatic}^{\dagger}(t) \rightarrow \frac{1}{2}\left(I_z + S_z^{2-3}\right). \tag{4.32}$$

Polarization is thus transferred from the I spin to the central transition of the S spin. Polarization transfer is interrupted when the first-order quadrupolar coupling passes through zero as a consequence of the sample rotation. The values of ξ_1 and ξ_2 now approach $\pi/2$ and the eqn (4.30) is now the governing Hamiltonian. The density matrix with $\tilde{\sigma}(0) = I_z$ now evolves as

$$\tilde{\sigma}(t) = U_{adiabatic}(t)\tilde{\sigma}(0)U_{adiabatic}^{\dagger}(t) \rightarrow \frac{1}{2}\left(I_z + S_z^{1-4}\right) \tag{4.33}$$

During MAS, this process occurs either two or four times every rotor period depending on the PAS orientation. In addition, S_z^{2-3} and S_z^{1-4} remain spin locked and unchanged during those periods when they are not involved in polarization transfer, the polarization transfer from I_z is switching between S_z^{2-3} and S_z^{1-4}, and the effective observable is also switching between

$$\tilde{S}_{+}(\xi \approx 0) \approx 2S_z^{2-3} - \sqrt{3}\left(S_x^{1-3} + S_x^{2-4}\right) + \sqrt{3}i\left(S_y^{1-2} + \frac{2\sqrt{3}}{3}S_y^{2-3} + S_y^{3-4}\right) \tag{4.34}$$

and

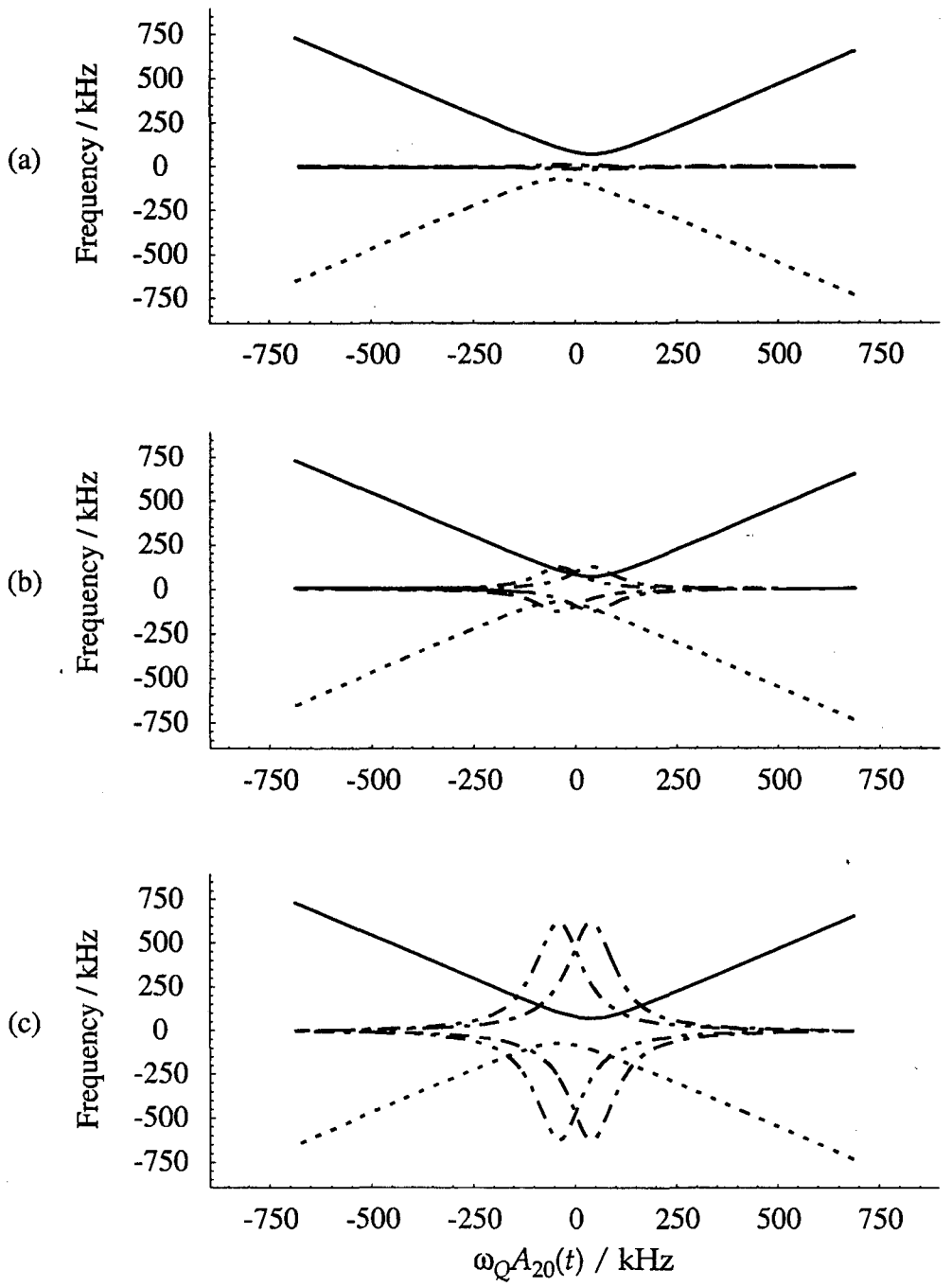

Figure 4.3 Diagonal coefficients $\omega^{1\text{-}3}$ (——) and $\omega^{2\text{-}4}$ (- - -) and off-diagonal elements $2d\xi_1/dt$ (— · —) and $2d\xi_2/dt$ (— — —) as a function of $\omega_Q A_{20}^Q(t)$. (a) Adiabatic regime calculated with a spinning rate 100 Hz corresponding to $\alpha = 5.5$. (b) Intermediate regime calculated with a spinning rate of 1 kHz corresponding to $\alpha = 0.55$. (c) Sudden regime calculated with a spinning rate of 5 kHz corresponding to $\alpha = 0.11$.

$$\tilde{S}_+\left(\xi \approx \frac{\pi}{2}\right) \approx -2S_z^{1-4} + \sqrt{3}\left(S_z^{1-3} - S_x^{2-4}\right) + \sqrt{3}i\left(S_y^{1-2} + \frac{2\sqrt{3}}{3}S_y^{1-4} + S_y^{3-4}\right). \quad (4.35)$$

As shown by Vega [83], after multiple zero crossings, the central and triple quantum transitions will be equally polarized from the I spin. The overall CP intensity will be identical to that observed for a static spin in the thermodynamic limit. However, the overall rate will be half as fast, since both the central and triple quantum transitions are being polarized simultaneously. In the presence of a short rotating frame relaxation time, this will lead to a reduced overall CP intensity from the spins undergoing adiabatic zero crossings.

When the sudden approximation holds, the propagator can be written

$$\tilde{U}_{sudden}(t) = \exp\left[\int_0^t \dot{W}^{\dagger}(t')W(t')dt'\right]. \quad (4.36)$$

While this propagator does not hold for all times, the term $\dot{W}^{\dagger}(t)W(t)$ has the form of an impulse function with an integrated area of $\pi/2$ centered near the zero crossing of $A_{20}^{Q}(t)$. This results in a discontinuous transition between the adiabatic propagator of eqn (4.31) and the sudden propagator of eqn (4.36) (see Fig. 4.3c). Under the sudden propagator, S_z^{2-3} and S_z^{1-4} transform according to

$$\tilde{\sigma}(t) = \tilde{U}_{sudden}(t)S_z^{2-3}\tilde{U}_{sudden}^{\dagger}(t) \rightarrow S_z^{1-4} \quad (4.37)$$

and

$$\tilde{\sigma}(t) = \tilde{U}_{sudden}(t)S_z^{1-4}\tilde{U}_{sudden}^{\dagger}(t) \rightarrow S_z^{2-3} \quad (4.38)$$

Therefore, the coefficients of the S_z^{2-3} and S_z^{1-4} terms in the density matrix will be exchanged after evolving through a sudden zero crossing. After multiple zero crossings, one of the two transitions will be completely polarized while the other will be unpolarized. The observable operator will always match the cross polarizing transition, so the polarized intensity will always remain observable, and the CP efficiency and rate should be identical to the static case.

Crystallites which pass through the zero crossing under neither adiabatic or sudden conditions fall into the intermediate regime. This type of evolution is the most difficult to calculate analytically. As indicated in Fig. 4.3b, in determining such evolution, contributions from both $\tilde{H}(t)$ and $\dot{W}^{\dagger}(t)W(t)$, which do not commute at all times, must be retained in the propagator in eqn (4.22). Vega [82 ,83] has shown with numerical simulations that spins undergoing an intermediate regime zero crossing evolve into non-spin locked states and thus result in a significant loss of CP intensity.

To indicate whether a zero crossing is in the adiabatic, intermediate, or sudden regime, an adiabaticity parameter α is defined:

$$\alpha = \frac{\omega^{1-3}\left(t_0^{1-3}\right)}{\left.\frac{2d\xi_1(t)}{dt}\right|_{t_0^{1-3}}} = -\frac{\omega^{2-4}\left(t_0^{2-4}\right)}{\left.\frac{2d\xi_2(t)}{dt}\right|_{t_0^{2-4}}} = \frac{3\omega_{1S}^2}{\omega_Q \left.\frac{dA_{20}^{Q}(t)}{dt}\right|_{t_0^{1-3}}} \tag{4.39}$$

This is then evaluated at one of the zero crossings, $\omega_Q A_{20}^{Q}\left(t_0^{1-3}\right) \approx \omega_{1S}$ or $\omega_Q A_{20}^{Q}\left(t_0^{1-3}\right) \approx -\omega_{1S}$, corresponding to a maximum in $\dot{W}^{\dagger}(t)W(t)$ as ξ_1 or ξ_2 pass through $\pi/4$. This definition of the adiabaticity parameter is proportional to the one used by Vega [83], however, there is an additional orientation dependence as well which comes from the time derivative of $A_{20}^{Q}(t)$. When the value of α at the zero crossing is much larger than one, the crossing will be adiabatic. If it is much less than one, it will fall into the sudden regime. When α is on the order of one, the crossing will be in the intermediate regime.

Theoretically, it is possible to adjust α to match any of these three conditions by changing the spinning rate or rf power levels. However, in a multi-site system it may be difficult or even impossible to adjust for optimal CP transfer of all sites while spinning at the magic angle. One solution that eliminates the problem is to exploit the time independence of the spin eigenvalues when spin-

ning at 0° (parallel) to the external magnetic field direction. By performing cross polarization while spinning at 0°, none of the spins undergo zero crossing and the full static CP intensity can be recovered. When designing the CPDAS experiment, we therefore logically pick the $k = 5$ angle pair (0°, 63.43°), performing the cross-polarization at 0° and acquisition at 63.43°. In order to improve cross polarization under MAS or VAS, we can perform the zero-polarized MAS (ZPMAS) or zero-polarized (ZPVAS), in which cross polarization occurs at 0° followed by a hop to a second angle to collect a MAS or VAS spectrum.

4.3 Experimental

Experiments were performed on a home-built spectrometer at 7.04 T, corresponding to a ^{1}H NMR frequency of 301.2 MHz and a ^{23}Na frequency of 79.671 MHz. The DAS probe was home built with a stationary coil with a diameter of 19 mm, used for both transmission and detection [54]. The double-tuned rf resonant circuit was similar to one described by Doty *et al.* [87,88]. The input power of 300 watts on the ^{1}H channel gave 7 μs ^{1}H $\pi/2$ pulses and 100 watts on the ^{23}Na channel gave 7 μs central transition selective ^{23}Na $\pi/2$ pulses. The spinning frequency was between 4.0 kHz and 6.6 kHz. The samples of sodium pyruvate used for these experiments were obtained from standard commercial sources. The pulse sequence for the various VAS experiments are given in Fig. 4.4, and the pulse sequence for CPDAS is shown in Fig. 4.5. Further details about the DAS pulse sequence and data processing can be found in Chapter 2 and in reference [42]. For the CP efficiency experiments, phase alternation of the ^{1}H rf pulse was used to assure that only the intensity due to CP would be measured. For CPDAS and ZPVAS experiments, a ^{23}Na $\pi/2$ pulse was

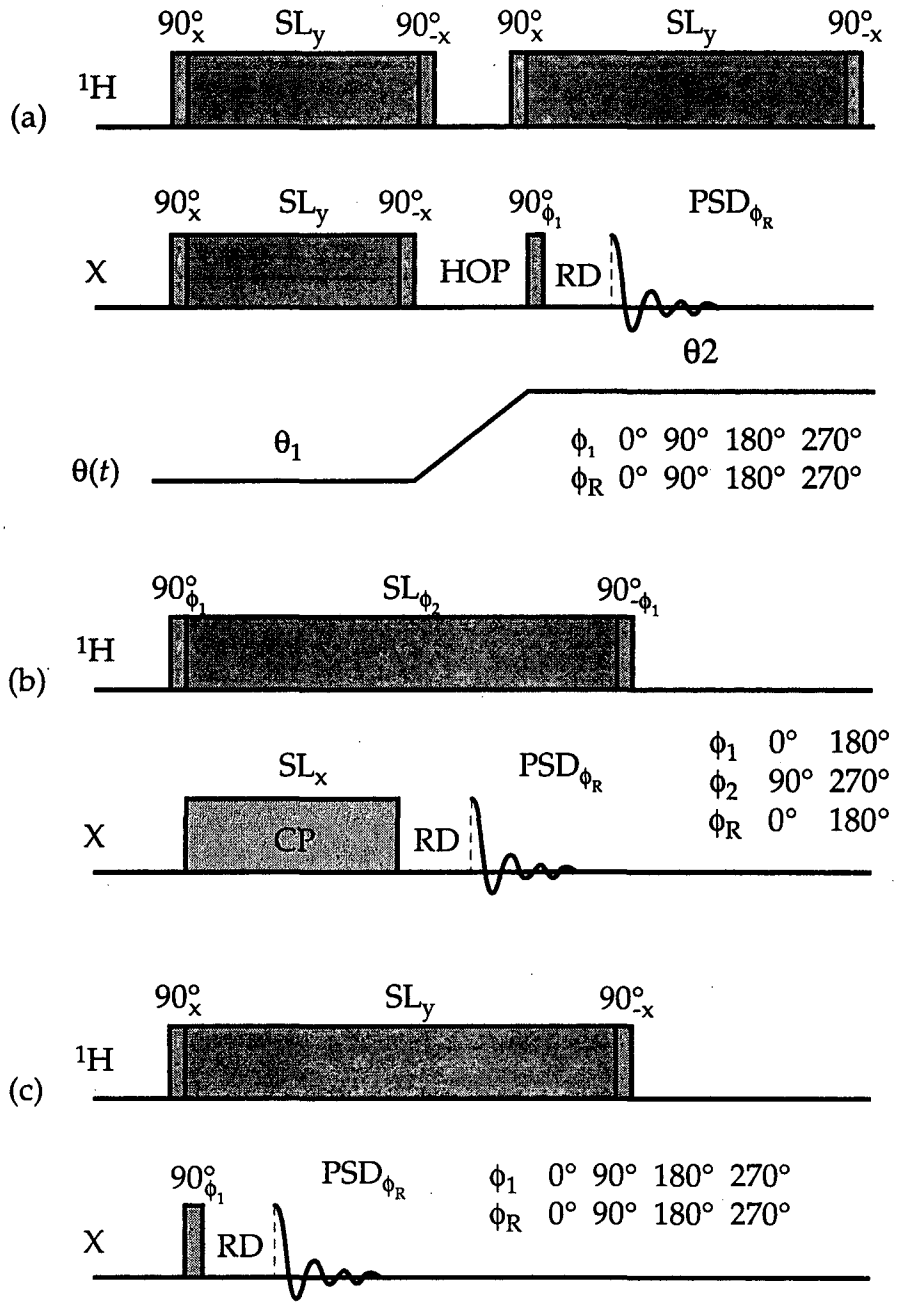

Figure 4.4 Pulse sequences used for (a) ZPVAS, (b) CPVAS, and (c) decoupled MAS experiments. SL refers to the spin lock period, subscripts refer to the phases of the pulses, $\theta(t)$ refers to the orientation of the spinning axis angle with respect to the magnetic field, and PSD refers to phase-sensitive detection. Decoupling is not performed during the storage period while the spinning axis is reoriented due to the long interval required.

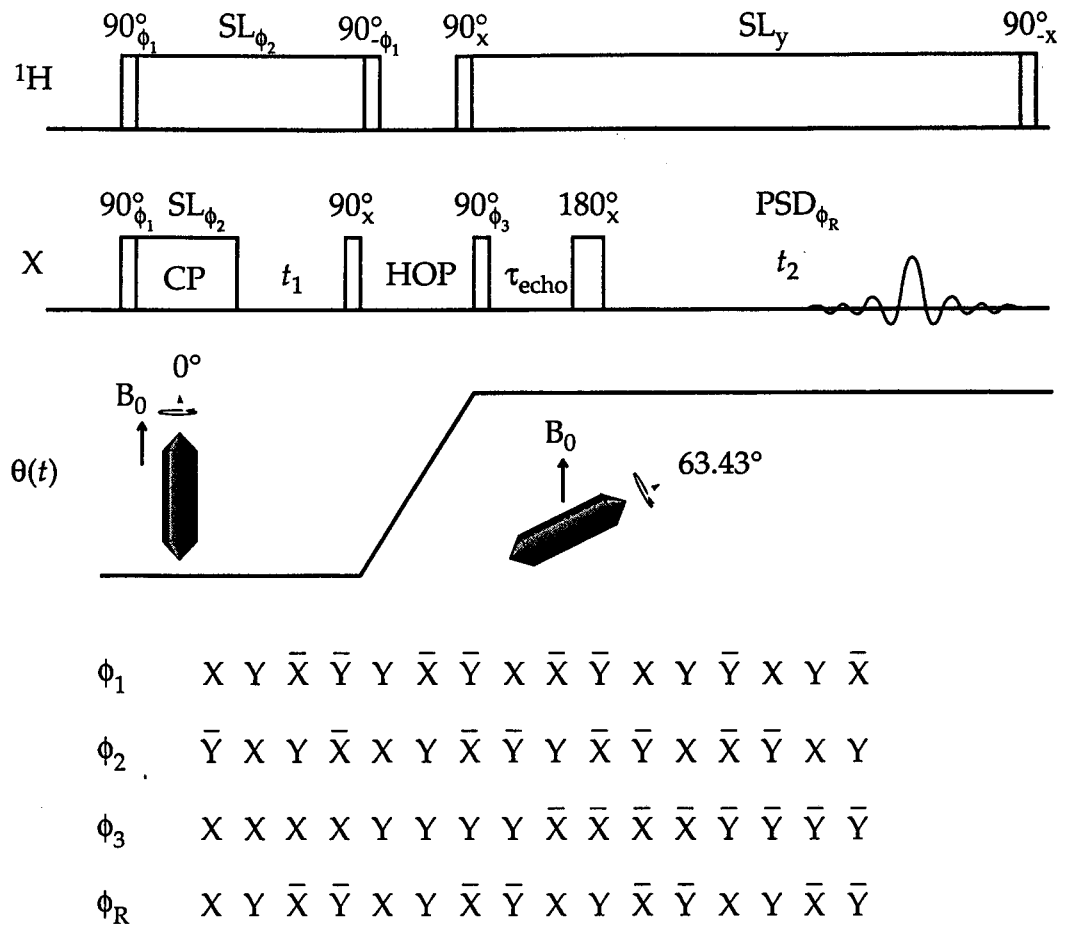

ϕ_1	X	Y	$\bar{X}$	$\bar{Y}$	Y	$\bar{X}$	$\bar{Y}$	X	$\bar{X}$	$\bar{Y}$	X	Y	$\bar{Y}$	X	Y	$\bar{X}$
ϕ_2	$\bar{Y}$	X	Y	$\bar{X}$	X	Y	$\bar{X}$	$\bar{Y}$	Y	$\bar{X}$	$\bar{Y}$	X	$\bar{X}$	$\bar{Y}$	X	Y
ϕ_3	X	X	X	X	Y	Y	Y	Y	$\bar{X}$	$\bar{X}$	$\bar{X}$	$\bar{X}$	$\bar{Y}$	$\bar{Y}$	$\bar{Y}$	$\bar{Y}$
ϕ_R	X	Y	$\bar{X}$	$\bar{Y}$	X	Y	$\bar{X}$	$\bar{Y}$	X	Y	$\bar{X}$	$\bar{Y}$	X	Y	$\bar{X}$	$\bar{Y}$

Figure 4.5 Pulse sequence and rf phase cycle for the two-dimensional ^{1}H decoupled CPDAS experiment. SL refers to spinlock period, PSD refers to phase-sensitive detection, subscripts indicated the phase of the pulse, and $\theta(t)$ refers to the orientation of the spinning axis with respect to the magnetic field. Decoupling is not performed during the storage interval while the sample is being reoriented because of the long delay needed (typically 30 ms - 100 ms). Further details can be found in Chapter 2.

applied simultaneously with the initial ^{1}H $\pi/2$ pulse to achieve the largest final sodium polarization. For the ^{23}Na spectra without CP, a recycle delay of 16 s was used for the sodium pyruvate while for the CP experiments a recycle delay of 36 s was used to assure complete relaxation and accurate intensity comparisons. For the DAS experiments, 32 scans were acquired after one dummy scan

for each of the 90 t_1 points, while for the CP build up curves and ZPVAS either 4, 8, or 64 scans were acquired after two dummy scans for each different contact time and angle pair. For the CPDAS and ZPVAS experiments on sodium pyruvate the CP contact time was 20 ms. The procedures used for simulating quadrupolar powder patterns can be found in reference [55].

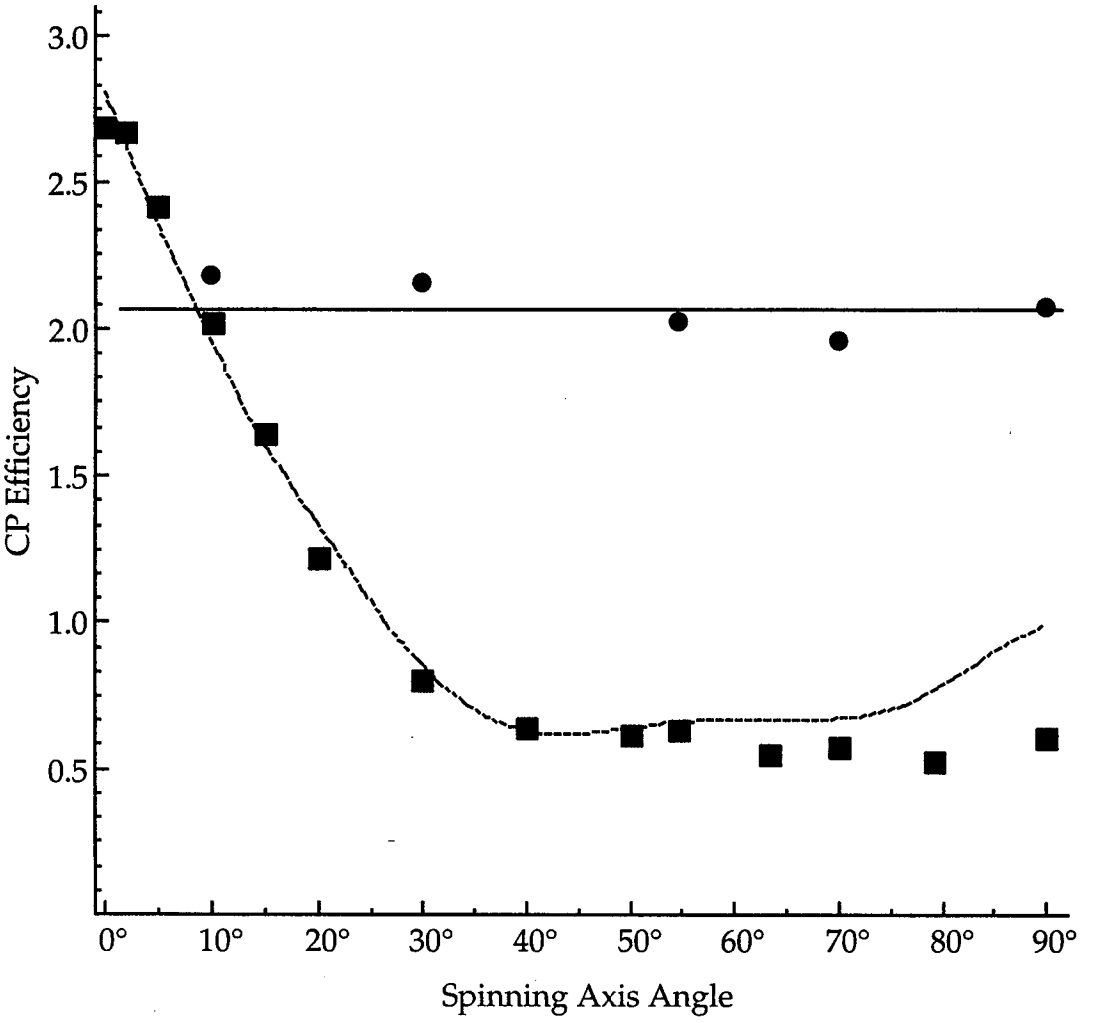

Figure 4.6 CP intensity as a function of VAS angle for sodium pyruvate using traditional CPVAS (■) and using ZPVAS (●). The curve through the CPVAS data was obtained numerically as described in the text. The line through the ZPVAS data indicates the average intensity obtained from all experiments. The contact time was 20 ms.

4.4 Results and Discussion

The effect of level crossings on CP efficiency can be seen clearly in Fig. 4.6, which shows the cross polarization efficiencies of sodium pyruvate, $CH_3OCOONa$, versus VAS angle. All intensities are scaled relative to the corresponding single pulse ^{23}Na VAS and MAS spectra, using the sequence in Fig. 4.4 a. As expected, only under static (0° VAS) conditions is the expected CP efficiency maximum of approximately $3\gamma_1/4\gamma_2$ for sodium pyruvate achieved. The factor of 3/4 is due to the high abundance of both ^1H and ^{23}Na causing cross polarization to be controlled by the equilibrium between the respective spin temperatures. As the VAS angle increases, CP efficiency decreases dramatically. Spinning the sample at an angle greater than approximately 25° results in an efficiency that is less than that achieved by a single pulse. This indicates that the level crossings are significant, even when only a reduced fraction of the spins are undergoing the maximum of four crossings per rotor cycle.

We can calculate the approximate CP efficiency at any given spinning angle, shown by the dashed curve in Fig. 4.6, by first determining the number of crystallites with excursions of $\xi_1(t)$ and $\xi_2(t)$ within some value δ of 0° or 90° and therefore capable of Hartmann-Hahn matching. For the data shown in Fig. 4.6, it was assumed that $\delta \approx 15°$, corresponding to approximately $\omega_Q A_{20}^Q(t) > 5\omega_{1S}$, which should be sufficiently large to allow the Hartmann-Hahn match condition to be met. For those spins that can undergo cross polarization, we sum the number that undergo adiabatic or sudden regime zero crossings. The spins undergoing sudden regime zero crossings are assigned an intensity of 1.0. Spins where $\left|\omega_Q A_{20}^Q(t)\right|$ is large for the entire rotor period but undergo no zero crossings also fall into this category. The adiabatic spins are assigned an arbitrary intensity between 0.5 and 1.0 to account for their slower rate of polarization compared to the

spins undergoing sudden regime zero crossings. The intensity of those spins with a large $\left|\omega_Q A_{20}^Q(t)\right|$, but undergoing intermediate regime zero crossings, as well as those where $\left|\omega_Q A_{20}^Q(t)\right|$ is sufficiently small for much of the rotor period so that the Hartmann-Hahn match condition in eqn (4.6) does not hold, is assumed to be lost. To determine whether a spin is undergoing an adiabatic or sudden regime zero crossing, we consider the value of the adiabaticity parameter, α, given in eqn (4.39) and as explained above, assume those spins with α much greater than one are in the adiabatic regime, those spins with α much less than one are in the sudden regime, and those spins with α on the order of one are in the intermediate regime. The values used for e^2qQ/h and η_Q were 2.36 MHz and 0.77, respectively, in these calculations. These values were obtained from simulations of the MAS spectrum as mentioned earlier.

Fig. 4.6 also shows CP efficiency for sodium pyruvate at the angle at which detection occurred under ZPVAS. Since CP always occurs at 0°, under effectively static conditions, the observed efficiency is constant for all angles. The observed decrease in efficiency compared to that of cross-polarization under 0° VAS is due to T_1 relaxation processes that occur during the hop from 0° to the detection angle.

Fig. 4.7 shows the ^{1}H decoupled MAS spectra of sodium pyruvate acquired with and without cross polarization and with ZPMAS along with the simulation of the MAS powder pattern. The signal-to-noise is the worst for CPMAS—about 75% of that seen in the MAS spectrum without CP. On the other hand, the ZPMAS spectrum has a signal-to-noise ratio about twice that seen in the MAS spectrum taken without CP.

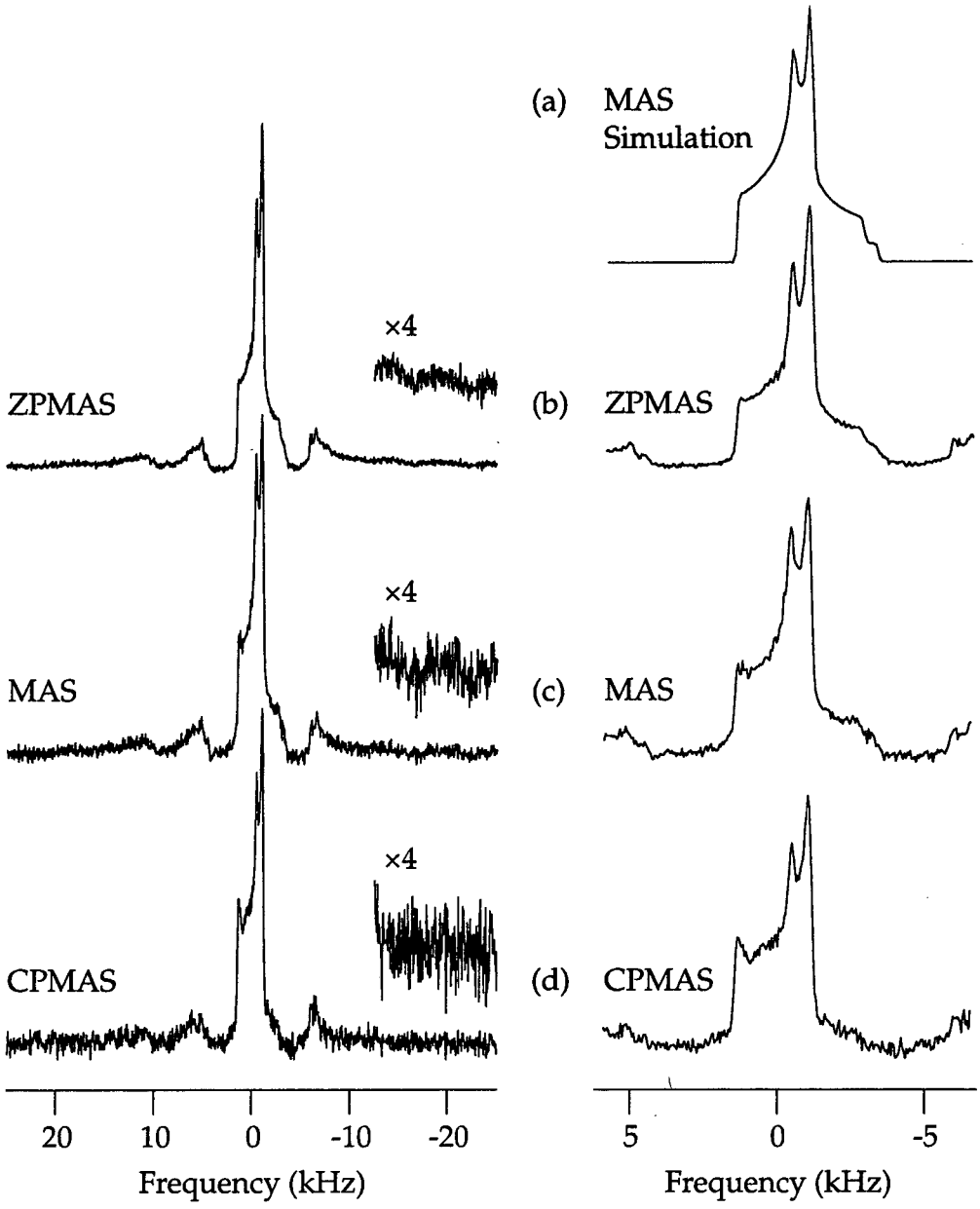

Figure 4.7 MAS spectra of sodium pyruvate acquired with the (b) ZPMAS, (c) MAS, and (d) CPMAS pulse sequences given in Fig. 4.4. The center band is expanded on the right to show details more clearly. The insets show magnified sections of the baseline for comparison of signal-to-noise ratios. (a) The MAS simulation was calculated as explained in reference [55] and generated values of e^2qQ/h = 2.36 MHz and η_Q = 0.77.

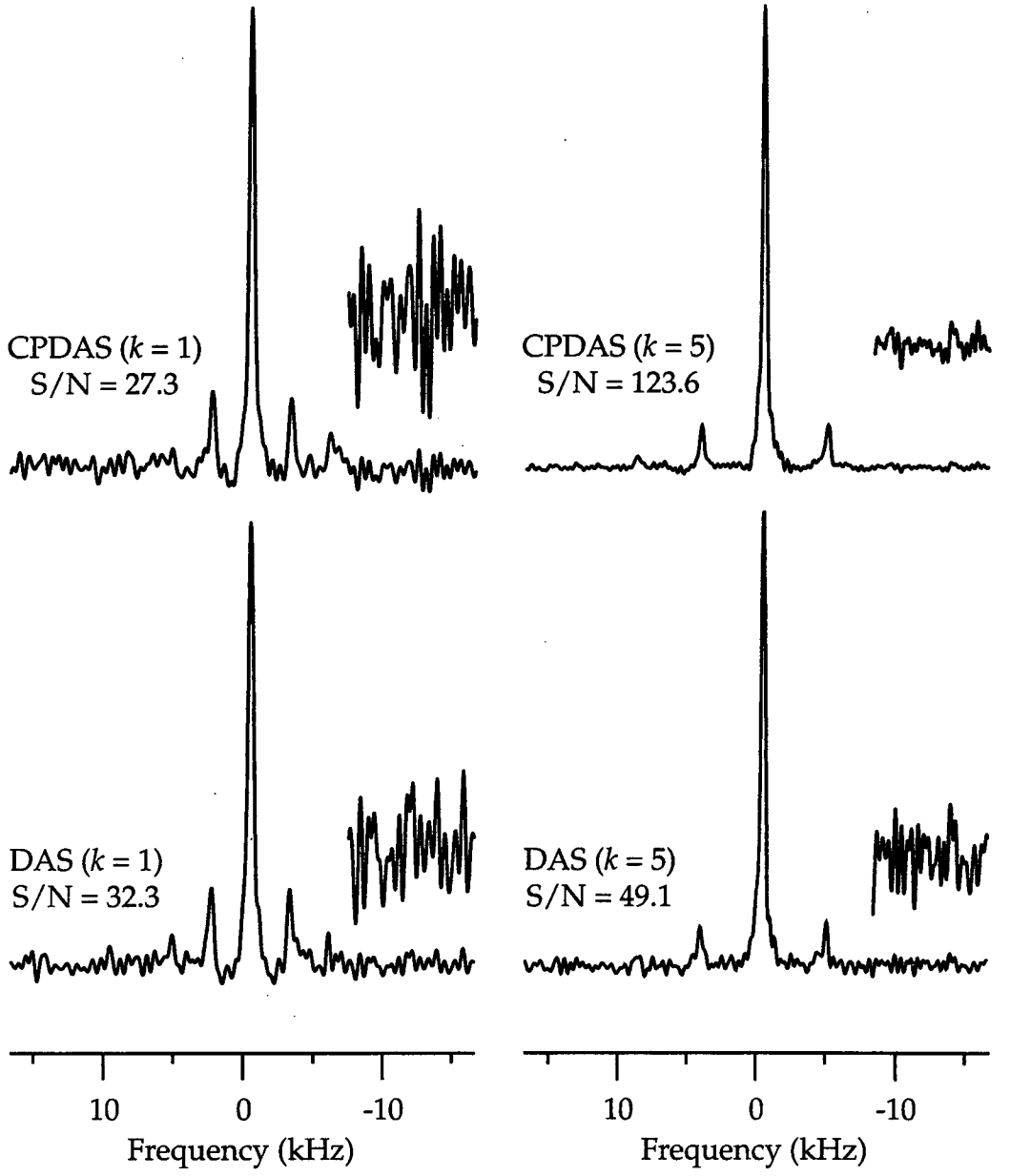

Figure 4.8 CPDAS and DAS spectra of sodium pyruvate taken with the $k = 1$ (37.38°, 79.19°) and $k = 5$ (0°, 63.43°) angle pairs using the pulse sequence in Fig. 4.5. Insets shows the baseline of the respective spectra magnified by × 5 for better comparison of signal-to-noise ratios.

In Fig. 4.8, the decoupled DAS and CPDAS spectra of sodium pyruvate for the $k = 5$ (0°, 63.43°) and $k = 1$ (37.38°, 79.19°) angle pairs are compared. For

$k = 5$, we observe over 2.5 times the signal-to-noise in the spectrum taken with CP compared to the spectrum taken without CP. In addition, the CPDAS experiment at $k = 5$ has a signal-to-noise ratio over 4.5 times that of the CPDAS experiment at $k = 1$. This demonstrates the importance of 0° cross polarization for DAS. The CPDAS experiment done at 37.38° ($k = 1$) has a worse signal-to-noise than the same experiment done without cross polarization. Other k values will also have reduced CP efficiencies.

4.5 CPDAS of ^{17}O Labelled L-Alanine

The study of biologically active and other organic compounds by solid-state NMR has for the most part been limited to spin-1/2 nuclei such as ^{1}H, ^{13}C, ^{15}N, ^{19}F, and ^{31}P. The study of ^{17}O, a quadrupolar nucleus ($S = 5/2$), in solid organic compounds has been limited due to its low natural abundance, low gyromagnetic ratio, and strong second-order quadrupolar interactions. The first two difficulties can be alleviated to some extent through isotopic substitution, the use of high magnetic fields, and through cross polarization (CP) [72] from ^{1}H to the central ($1/2 \leftrightarrow 1/2$) ^{17}O transition. For a static sample, it is theoretically possible to achieve a one-shot sensitivity enhancement of 7.3 (assuming a large excess of ^{1}H compared to ^{17}O). However, as described above, when the sample is spun about an axis inclined with respect to the magnetic field, there can be a significant decrease in CP efficiency because the time dependence of the first-order quadrupolar interaction interferes with Hartmann-Hahn matching. In this section is demonstrated the application of CPDAS to ^{17}O labeled L-alanine [89].

Experimental

A sample of L-alanine, enriched approximately to 20% in ^{17}O, was synthesized by H. Zimmermann by acid-catalyzed exchange of oxygen in ^{17}O labeled

water at 80 °C, followed by neutralization with aniline and precipitation of the free amino acid. Powder x-ray diffraction was consistent with the known structure of L-alanine [90]. A polycrystalline sample of approximately 200 mg was used for the following experiments. Experimental details of the DAS experiment are as explained in Chapter 2. Cross-polarization experiments were performed at a field of 7.04 T (301.2 MHz for the ^{1}H frequency and 40.832 MHz for the ^{17}O frequency) on a home-built spectrometer using a Tecmag acquisition system and a home-built DAS probe [54] spinning at 6 kHz, with the pulse sequence shown in Fig. 4.5. The probe was equipped with a double-tuned rf-circuit with a 3/4" static coil based on a description by Doty *et al.* [88]. A decoupling power level of 500 W on the ^{1}H channel produced a $\pi/2$ pulse width of approximately 7 μs. A 7 μs ^{17}O $\pi/2$ pulse selective to the central transition was also used to achieve the Hartmann-Hahn match condition given in eqn (4.5). The cross-polarization contact time was 1 ms, which gave a CP efficiency per scan (signal compared to a single pulse FID on oxygen with hydrogen spin decoupling) of approximately 200%. The theoretical maximum was not achieved because of short rotating frame relaxation times. T_1 relaxation times were 750 ms for ^{1}H and 2.5 s for ^{17}O. DAS experiments at a field strength of 11.7 T (67.797 MHz) were performed on a CMX spectrometer using the single-tuned DAS probe described in reference [54]. No decoupling or cross-polarization was performed at this field because the DAS probe as designed is incapable of being tuned to the ^{1}H frequency of 500 MHz.

Results and Discussion

The structure of the amino acid L-alanine, shown in Fig. 4.9, has been determined previously by x-ray crystallography and neutron diffraction [90-91] and indicates two inequivalent ^{17}O sites due to a difference in hydrogen bonding

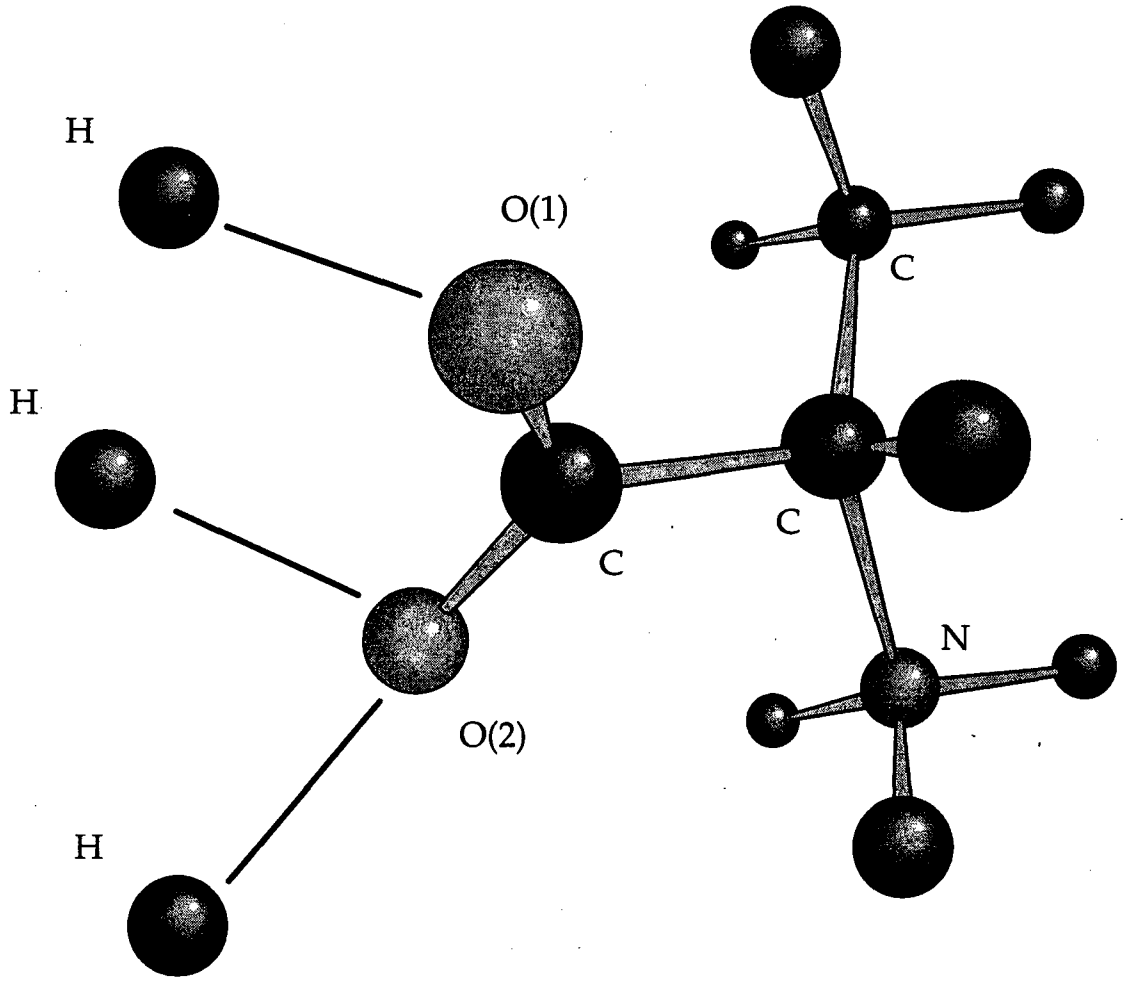

Figure 4.9 Structure of L-alanine showing the differences in hydrogen bonding at the two oxygen sites.

of the two oxygen atoms [91], so the spectrum should consist of two overlapping powder patterns. Fig. 4.10 shows the ^{17}O MAS and DAS spectra of L-alanine taken at 11.7 T, both without spin decoupling. The MAS spectrum shows a broad powder pattern with a number of singularities. In addition, sidebands complicate the powder pattern, resulting in a spectrum that is difficult to simulate. In contrast, the DAS spectrum shows a separated isotropic peak and sideband pattern. The two sites in alanine are not clearly resolved in this spectrum and appear as one peak. The isotropic position is assigned to 200 ± 7 ppm by com-

parison with a spectrum taken at a different spinning speed.

Fig. 4.11 shows the two-dimensional CPDAS spectrum of alanine, along with the projection of the isotropic shift dimension, acquired at 7.0 T. Spin de-

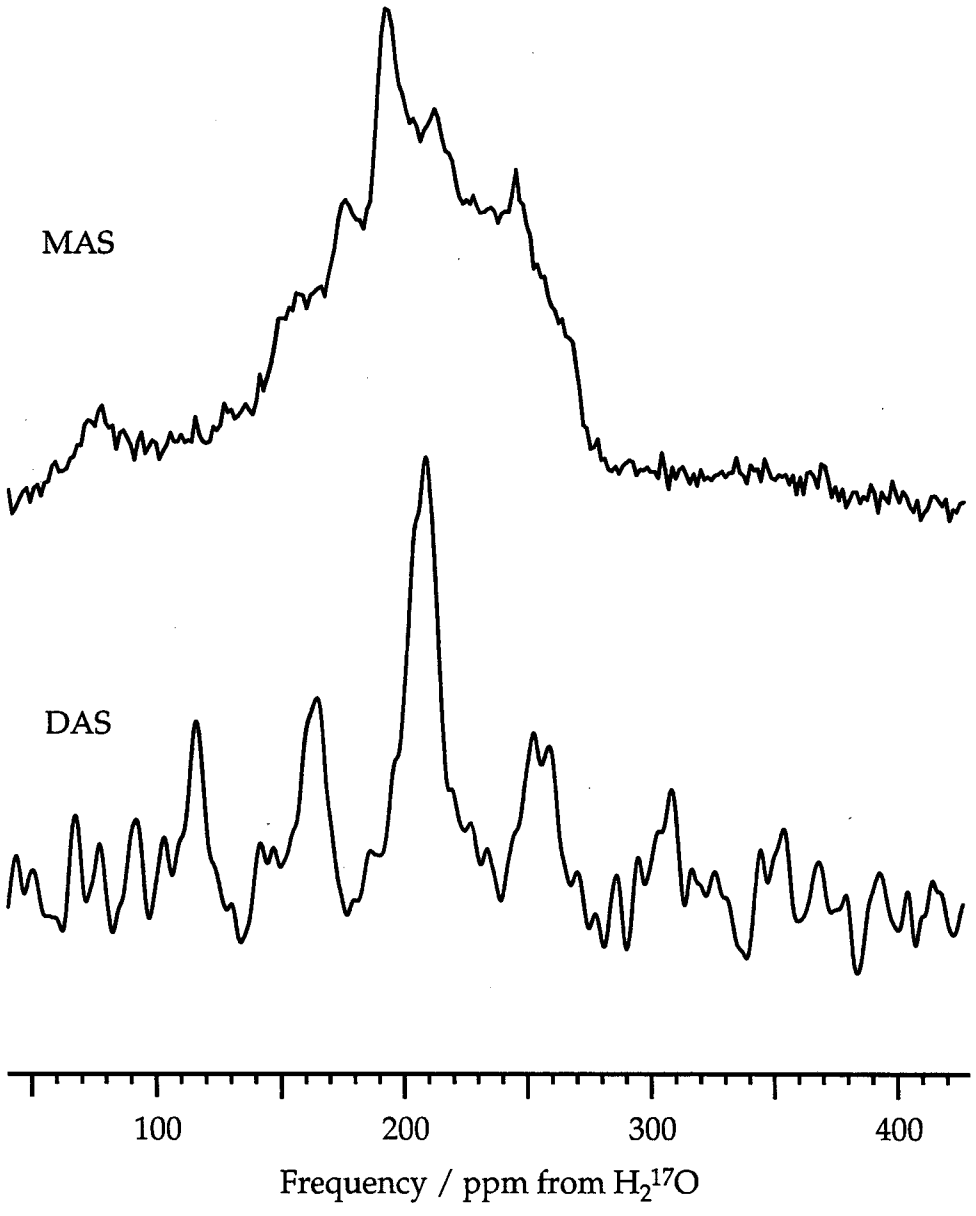

Figure 4.10 Magic-angle spinning (MAS) and dynamic-angle spinning (DAS) spectra of ^{17}O in L-alanine at 11.7 T (67.797 MHz), without proton spin decoupling. The spectra are referenced to ^{17}O labeled H_2O.

coupling of ^1H resulted in lines significantly narrower than that of the experiment without decoupling in Fig. 4.10. The two sites are clearly resolved and are assigned to 51 ± 4 and 80 ± 4 ppm by comparison to a spectrum taken at a different spinning speed. The advantages of using cross polarization are that the signal intensity per scan is approximately twice that seen in an experiment without cross polarization, and the recycle time is determined by the T_1 of ^1H rather than that of ^{17}O, resulting in an increase in the signal-to-noise ratio by a factor of two, giving an overall four-fold increase in the signal-to-noise ratio. As mentioned above, cross polarizing from ^1H to ^{17}O can result in an increase in intensity by a factor of 7.3, so with favorable relaxation times the enhancement of the signal-to-noise ratio can be considerable and in fact could be crucial in rendering an experiment feasible. Even with the enhancement provided by cross polarization and decreased recycle time, the CPDAS experiment in Fig. 4.11 required approximately 400 hours; a decoupled CPDAS spectrum without cross polarization could not be acquired for this reason.

Using the results of the experiments at the two different fields, the isotropic chemical shifts and quadrupolar coupling products can be calculated by solving a system of simultaneous linear equations as described in Chapter 2, using eqn (2.30), the results given in Table 4.1. The values for the quadrupolar coupling product, P_Q, are in good agreement with the quadrupolar coupling constant measured for the carboxyl oxygen atoms in similar compounds using NQR [92]. Due to the similarities of the sites, it is not possible to assign the spectra to particular ^{17}O sites. However, further work on amino acids might reveal trends in isotropic chemical shift and quadrupolar coupling products which allow for the assignment of sites.

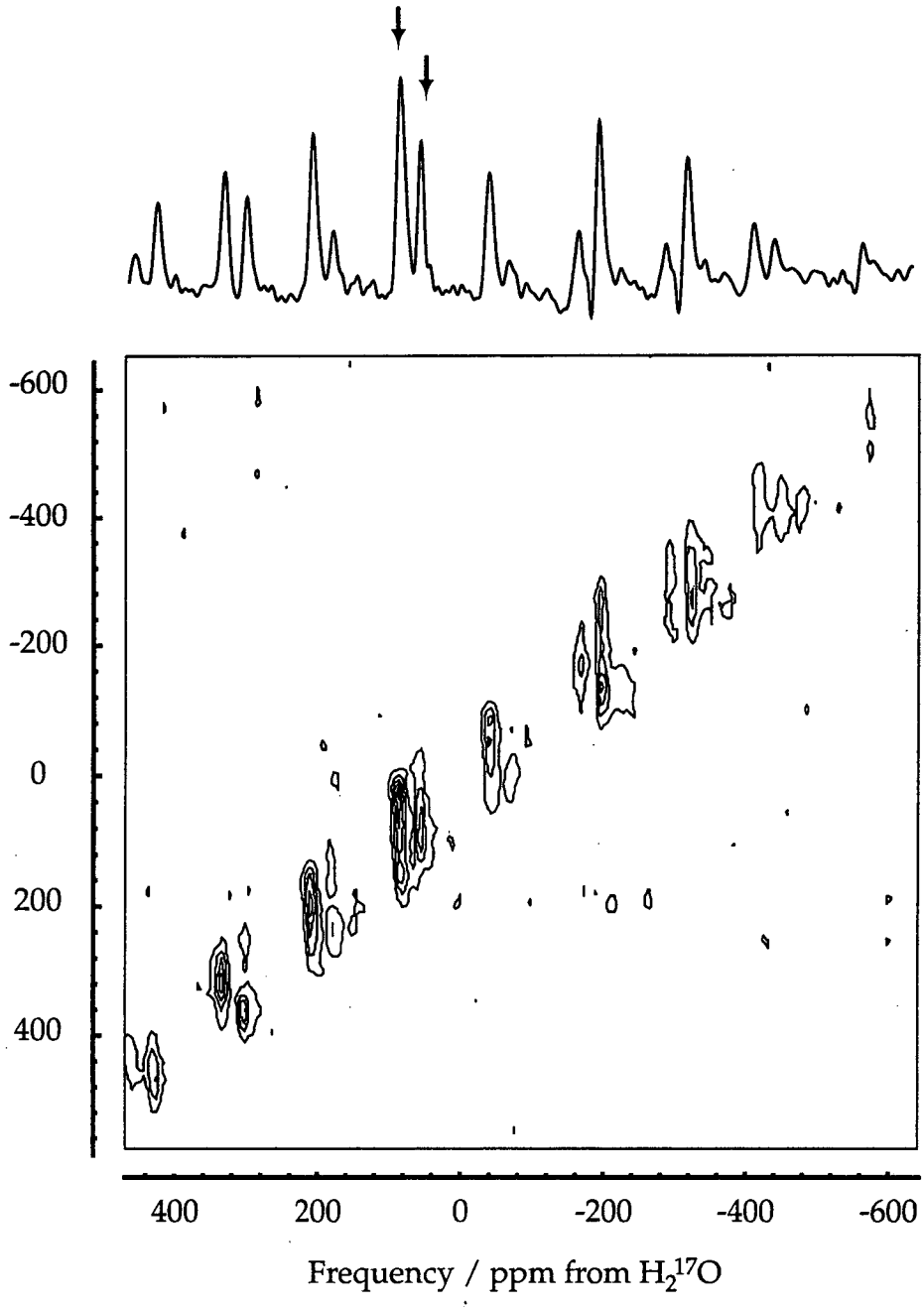

Figure 4.11 Two-dimensional DAS with cross polarization (CPDAS) and proton spin decoupling spectrum of ^{17}O in L-alanine at 7.04 T (40.832 MHz). The projection of the isotropic shift dimension is shown at the top with the isotropic peak positions indicated. The spectrum is referenced to ^{17}O labeled H_2O. The spinning frequency was 6 kHz.

Table 4.1 Isotropic shifts and quadrupolar coupling product, P_Q, for L-alanine.

$\delta_{obs}^{7.0T}$/ppm	$\delta_{obs}^{11.7T}$/ppm	P_Q / MHz	δ_{iso}^{CS}/ppm
51 ± 4	200 ± 7	8.1 ± 0.3	285 ± 8
80 ± 4	100 ± 7	7.1 ± 0.3	268 ± 8

NMR of ^{17}O in L-alanine has been performed previously by Goc, *et al.* [93], in which the static lineshape of a polycrystalline sample was simulated. Their simulation assumed that there was only a single ^{17}O site, while our work and the crystal structure are consistent with two inequivalent sites. The reported values for e^2qQ/h of 6.6 MHz and for η_Q of 0.55, which were reported to be precise to 20% [93], give a P_Q from their data of 6.9 MHz, which agrees (to within 20%) with our calculations for either site.

Both Figs. 4.10 and 4.11 show the disadvantages of insufficient spinning speeds. While the sidebands are clearly separated from the isotropic peaks in these spectra, in general, the large number of sidebands normally present in ^{17}O NMR of organic compounds can be a considerable problem. The types of compounds one would like to study with solid-state NMR, such as small peptides or carbohydrates, will typically have numerous inequivalent sites. However, fast spinning speeds are becoming easier to achieve in DAS experiments resulting in fewer sidebands. In addition, such techniques as dynamic-angle hopping (DAH), described in Chapter 3, can eliminate sidebands altogether in cases where adequate spinning speeds cannot be obtained.

Chapter 5
Variable-Effective-Field Cross Polarization

5.1 Introduction

Cross-polarization (CP) combined with magic angle spinning (CPMAS) is a powerful technique in modern solid state NMR to obtain high resolution, high sensitivity spectra of dilute spin nuclei (S) in the presence of an abundant spin species (I). The advantages of cross-polarization are both enhanced polarization, from the higher gyromagnetic ratio of the abundant spin species, and an enhanced repetition rate, as the experiment may be repeated at the abundant spin relaxation rate, which may be an order of magnitude faster than the rare spin relaxation rate.

Magic-angle spinning, at speeds comparable to the homonuclear I-spin dipolar interaction, converts the Hartmann-Hahn matching condition [71] for most efficient cross-polarization, $\omega_{1I} = \omega_{1S}$, into a series of sidebands at $\omega_{1I} = \omega_{1S} + n\omega_r$ [81] where ω_r is the spinning frequency and n is an integer. The sidebands can be very sharp and small deviations from the center of a peak, either due to spinning speed fluctuations or amplifier drift, can lead to dramatically decreased transfer rates as well as smaller equilibrium polarizations. Furthermore, the exact Hartmann-Hahn match ($n = 0$) exhibits kinetics that are several times slower than on the $n = \pm 1$ or ± 2 sidebands [81]. The sidebands, however, are quite sensitive to rf inhomogeneity as the condition $\omega_{1I} = \omega_{1S} + n\omega_r$

may not be satisfied for different regions of the sample, though ω_{1I} and ω_{1S} are scaled together.

These problems have attracted some attention recently as an increasing number of solid state NMR experiments require very rapid spinning rates which cause polarization sidebands even for strongly coupled ^{1}H spin systems [94-96]. As a result, several methods have been proposed to broaden the matching condition under MAS. Mechanical methods such as slowing [97] or stopping [98] the sample rotation, or hopping away from the magic angle during cross-polarization [99] are difficult to implement as well as costing an average factor of 2 in signal intensity, as the coherence must be stored along the z-axis during the motion. Barbara *et al.* [100], Zilm and coworkers [101], and Ernst and coworkers [102] have proposed pulse sequences which require synchronization with the sample rotation. As such the experiments are as sensitive to spinning speed instabilities as conventional CP, though they are well compensated for minor amplifier drift, as the match condition is substantially broadened. Smith and coworkers [103,104] have proposed the most promising variation to date, variable amplitude cross-polarization (VACP) which utilizes an amplitude modulated ^{1}H spin-locking field to cross-polarize under different matching conditions for different parts of the contact time. Unlike the sequences of Ernst and coworkers [102], which also employ amplitude modulation of the pulse train, VACP requires no rotor synchronization, however does require rapid switching of the rf amplitude while maintaining phase coherence.

In this chapter a new method is described to broaden the cross-polarization condition under MAS, variable effective field cross-polarization (VEFCP). VEFCP, like VACP, employs periods of differing *I*-spin nutation frequencies with the difference that VEFCP is performed at a constant rf amplitude. The varying

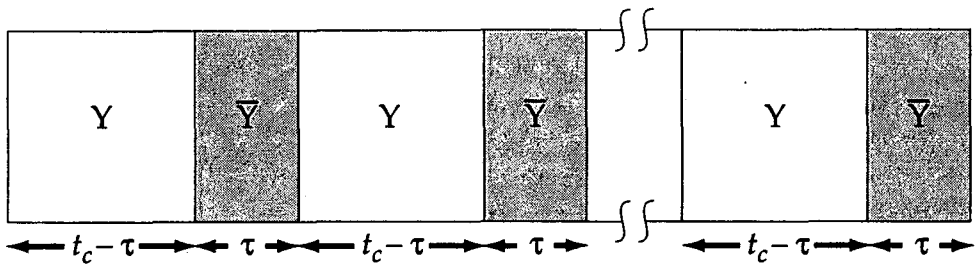

Figure 5.1 Schematic of the time-averaged precession frequency (TAPF) pulse sequence, a windowless two-pulse cycle consisting of a y pulse of length $t_c - \tau$ followed by a $-y$ pulse of duration τ, resulting in a net nutation of $(t_c - 2\tau)\omega_1$. Assuming a short t_c compared to the dipolar correlation time, the rf field is scaled over the cycle, resulting in an effective rf field of amplitude $\kappa\omega_1 = \left[(t_c - 2\tau)/t_c\right]\omega_1$.

nutation frequencies are achieved by changing the timing conditions of a time-averaged precession frequency (TAPF) pulse sequence [105]. A comparison of the polarization transfer *versus* the ^{13}C rf field for VEFCP and conventional CP will be made for adamantane and bisphenol-A polycarbonate. Further, the kinetics of cross-polarization under conventional CP and VEFCP will be compared.

5.2 Theory

The time-averaged precession frequency (TAPF) pulse sequence, shown in Fig. 5.1, is a windowless two pulse cycle with alternating π phase shifts, resulting in an effective scaling of the rf by a factor κ over the cycle. The scaling factor, κ, can be adjusted between $0 < \kappa < 1$, thus achieving a low nutation frequency for CP, while maintaining effective spin-locking due to the strong actual rf field. The TAPF pulse consists of a y pulse of duration $t_c - \tau$, followed by a $-y$ pulse of duration τ. The net nutation, around the y-axis, over the cycle time, t_c, is given by $(t_c - 2\tau)\omega_1$. The scaling factor, κ, is given by

$$\kappa = \frac{t_c - 2\tau}{t_c}. \tag{5.1}$$

Provided that t_c is small compared to the dipolar correlation time of the protons in the solid, the effective nutation is equivalent to a nutation about the y-axis at an effective rf field $\omega_{1,eff}$ of amplitude

$$\omega_{1,eff} = \kappa\omega_1 = \frac{t_c - 2\tau}{t_c}\omega_1. \tag{5.2}$$

The pulse sequence for VEFCP is illustrated in Fig. 5.2. After a $\pi/2$ pulse of phase x or $-x$, the protons are spin locked with a TAPF sequence of phase y. Adjusting the scaling factor by incrementing τ over the duration of the spin lock, leads to varying effective fields during the contact time which serve to broaden the matching conditions and average the kinetics of the polarization transfer.

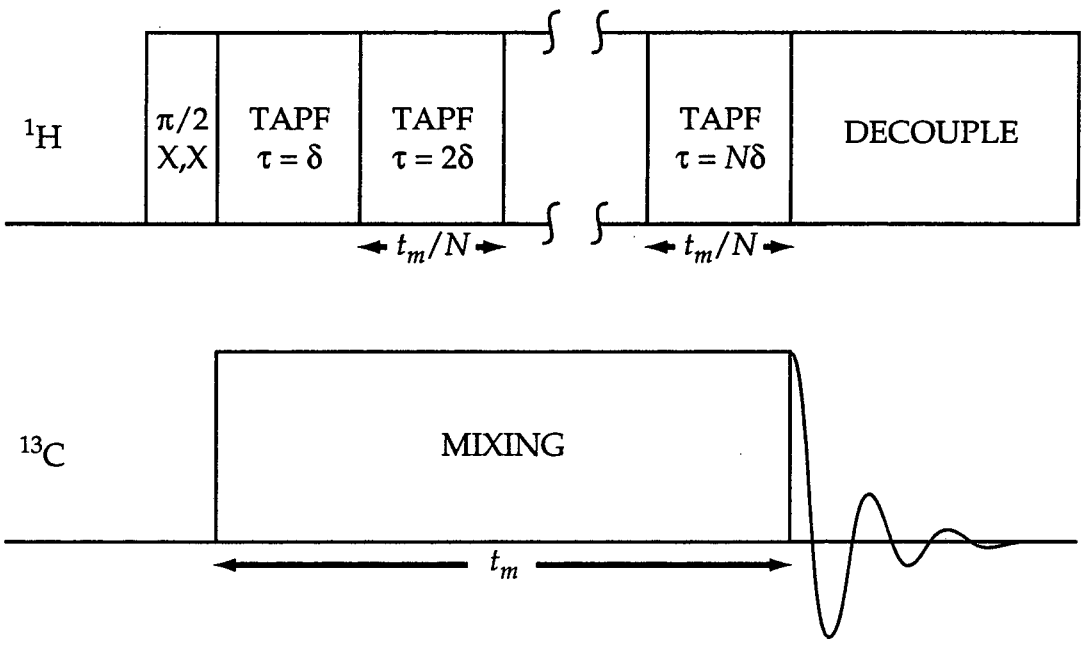

Figure 5.2 Schematic of the pulse sequence for variable-effective field cross polarization (VEFCP). Following a $\pi/2$ pulse of alternating phase of x and –x, the protons are spin-locked with a series of TAPF sequences, which give rise to an effective rf amplitude of $\kappa\omega_1 = \left[\left(t_c - 2\tau\right)/t_c\right]\omega_1$. Varying effective fields are generated by incrementing τ over the duration of the spin lock.

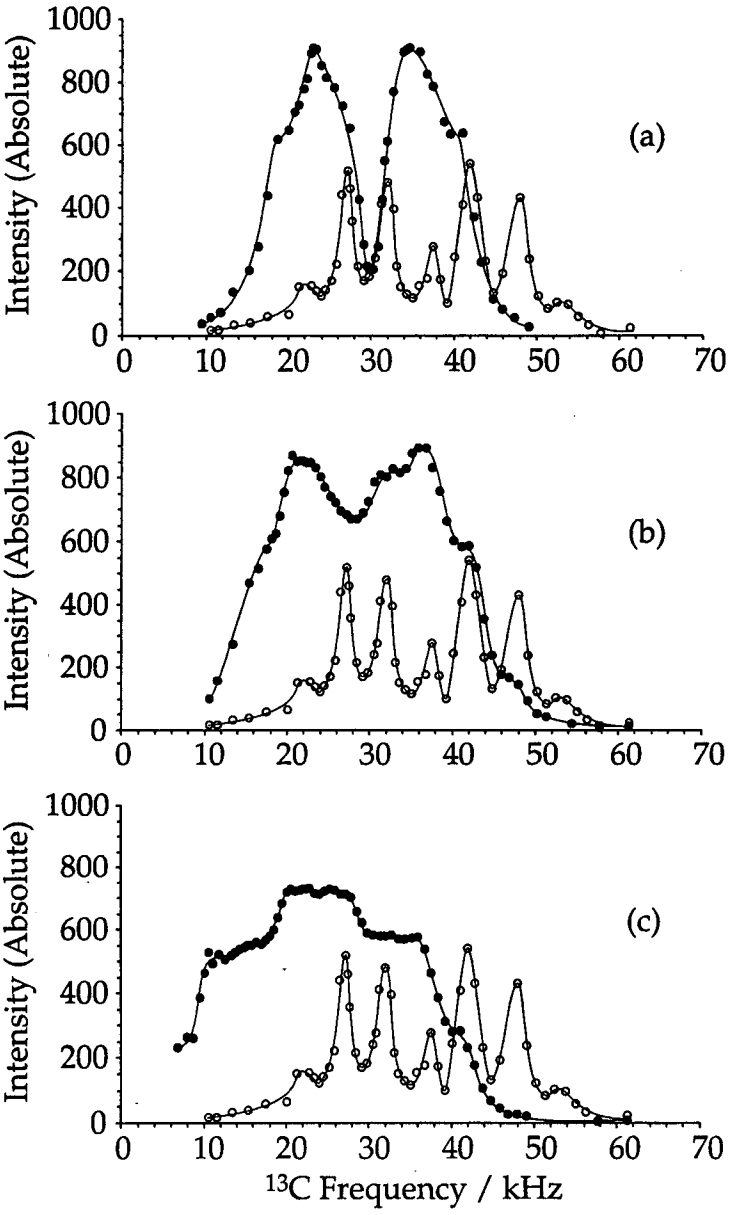

Figure 5.3 Cross-polarized intensity (in absolute units) *vs.* ^{13}C rf field strength for VEFCP (solid dots, solid lines) and conventional CP (open dots, dashed lines) of the CH line of adamantane spinning at $\omega_r/2\pi$ = 5.2 kHz. The total contact time in all cases is 6 ms, and the TAPF pulses used t_c = 10 ms. Lines are guides to the eye. The VEFCP parameters are (a) 8 intervals, 750 ms each, with scaling factors k = 0.90 to 0.76 in steps of 0.02, (b) 14 intervals, 430 ms each, with κ = 1, and .90 to 0.66 in steps of 0.02, and (c) 26 intervals, 230 ms each, with κ = 0.90 to 0.40 in steps of 0.02.

5.3 Results and Discussion

Fig. 5.3 demonstrates the polarization transfer *vs.* rf field strength for VEFCP (solid dots) and conventional CP (open circles) for a sample of adamantane spinning at $\omega_r/2\pi$ = 5.2 kHz. Note the polarization sidebands present in the conventional CP curve are centered around 37.5 kHz, the Hartmann-Hahn match, and spaced at integral multiples of ω_r. Although the thermodynamic limit at long contact times is identical for all of the polarization sidebands, a 6 ms contact time results in the slower kinetics at the Hartmann-Hahn match leading to a severely depressed signal strength at that position. The solid dots in Fig. 5.3 a represent the polarization transfer curve for an eight step VEFCP cycle in which the scaled rf fields vary over a range from $0.9\omega_1$ to $0.76\omega_1$, which spans a region 5 kHz wide around the Hartmann-Hahn condition. The frequency profile is somewhat lower at lower rf fields and correspondingly higher at higher rf fields. The entire VEFCP curve is shifted due to the rf scaling and is centered at $\langle\omega_{1I,eff}\rangle = 0.83\omega_{1I}$. The hole at $\langle\omega_{1I,eff}\rangle = \omega_{1S}$, the average scaled Hartmann-Hahn condition, occurs because the scaling profile does not encompass the $\pm\omega_r$ sidebands. At the average scaled Hartmann-Hahn match, the kinetics are comparable to that which would be obtained with conventional CP at the actual Hartmann-Hahn match, therefore, a contact time of 6 ms, the polarizations obtained are less than those for VEFCP with a profile centered about the $\pm\omega_r$ or $\pm2\omega_r$ sidebands. Fig. 5.3b illustrates the VEFCP curve (solid dots) versus conventional CP for a 14 step cycle with $\kappa\omega_1$ spanning the range ω_1 to $0.66\omega_1$. As the rf profile is now greater than ω_r at the scaled Hartmann-Hahn match, the depression is much less pronounced. Fig. 5.3c, which demonstrates a 26 interval VEFCP cycle with $\kappa\omega_1$ ranging from $0.4\omega_r$ to $0.9\omega_r$ in steps of 0.02, shows an enhancement at the average scaled Hartmann-Hahn match condition. The profile

for this sequence is over 12 kHz wide at the average scaled Hartmann-Hahn condition of 24.4 kHz, so at least 2 sidebands are covered over most of the rf range. The polarization curve displays shoulders as the rf profile moves through the range of the first and second order sidebands on either side of the match. The overall polarizations obtained are somewhat lower in Fig. 5.3c than in the VEFCP curves of Fig. 5.3a and 5.3b, due to the large nutation frequency spread for the 26 interval VEFCP (Fig. 2c). Clearly, the flattening of the matching condition to this extent has come with a price since some intervals at the edges of the profile have a very low efficiency per unit time.

VEFCP also has the effect of reducing the sensitivity of the kinetics to the matching conditions. Fig. 5.4a illustrates the kinetics of polarization transfer for conventional CP at $\omega_{1I} = \omega_{1S} \pm \omega_r$, (solid circles) and Hartmann-Hahn match, $\omega_{1I} = \omega_{1S}$ (open circles). The polarization rise with increasing contact time is several times more rapid for the sideband than it is for the Hartmann-Hahn match, though the thermodynamic limit is approximately the same for both. The decay of polarization at long times for the $n = -1$ sideband is not due to rotating frame relaxation, but is instead due to the extreme sharpness of the polarization sidebands for adamantane and a combination of coil detuning due to rf heating and a very slight amplifier drift over the course of the 2D experiment required for this measurement.

The polarization transfer *vs.* contact time for the 14-interval VEFCP sequence is illustrated in Fig. 5.4b. The solid dots represent transfer under the condition $\omega_{1I} += \omega_{1S} + \omega_r$, while the open dots represent the Hartmann-Hahn matching condition. The transfer rates are rather insensitive to the matching conditions, and are intermediate between the sideband and center band rates in conventional CP. Even in the thermodynamic limit, VEFCP seems to yield sub-

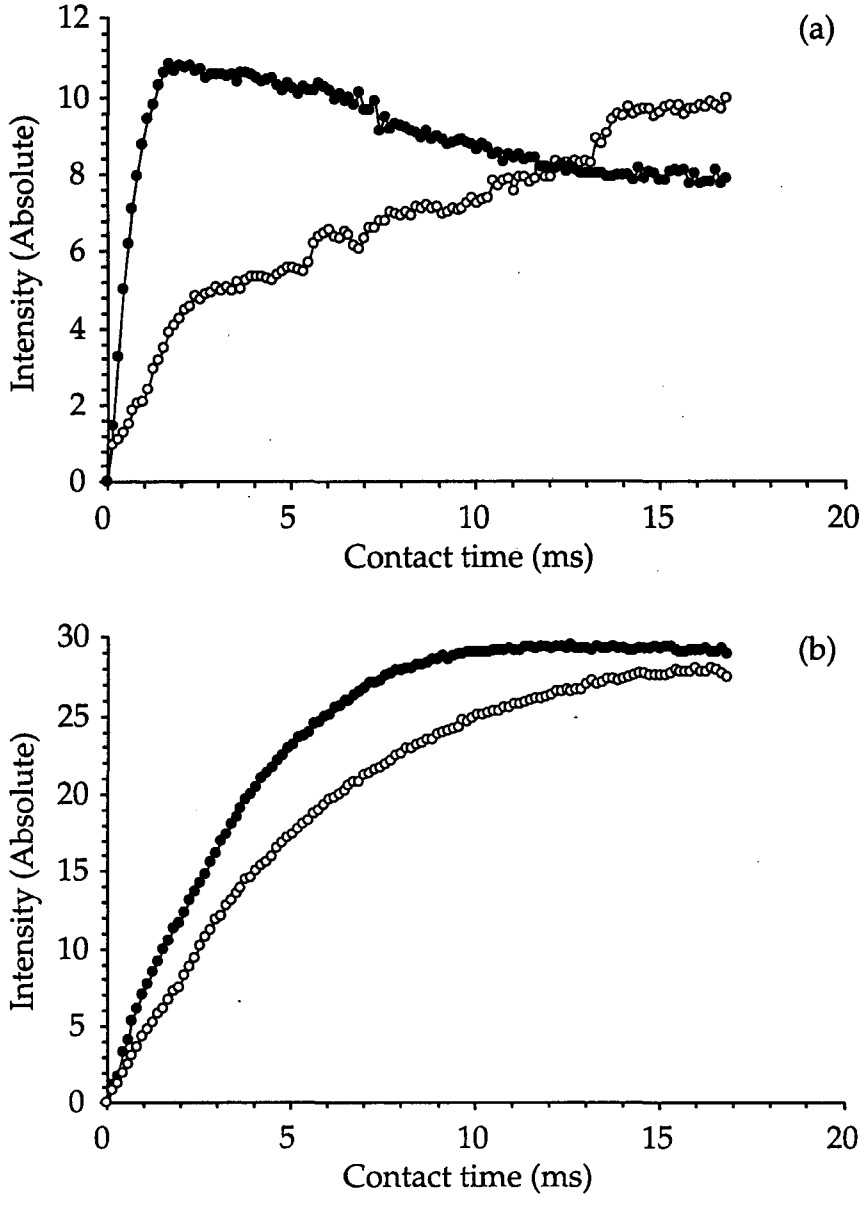

Figure 5.4 Cross-polarized intensity *vs.* contact time for the CH resonance of adamantane. The spinning frequency is $\omega_r/2\pi$ = 5.2 kHz. The open circles represent data acquired on the Hartmann-Hahn match, while the solid circles represent data acquired at either $+\omega_r$ or $-\omega_r$ away from match. The data was acquired in a two-dimensional fashion, with a read pulse following a variable spin-lock period. (a) Conventional CP where the solid dots are the intensity of the n = –1 sideband, and (b) VEFCP where the solid dots are the intensity of the n = +1 sideband, and taken over 14 intervals with t_c = 10 ms, κ = 1, and 0.90 to 0.66 in steps of 0.02.

stantially more polarization than conventional CP. This is likely to have resulted from the extreme sensitivity of adamantane to the matching conditions in conventional CP, which made a precise and stable match to a center- or sideband condition difficult. As VEFCP employs a range of different *I*-spin nutation frequencies, the effect of rf inhomogeneity is minimal, and this may contribute to larger equilibrium polarizations, relative to conventional CP, though, for conventional CP, the contribution of rf inhomogeneity is unimportant for the center band (Hartmann-Hahn) condition [102,104]. The experimental results reported here were acquired with a 7mm diameter, 10mm long sample centered in a 15 mm long solenoid coil wrapped with flat wire. The rf inhomogeneity was estimated, from a two-dimensional nutation experiment [106], to be 6.5% over the sample volume. A detailed study of the effects of rf inhomogeneity on CPMAS intensities has been recently reported by Smith and coworkers [104].

Fig. 5.5 illustrates the polarization profiles for bis-phenol-A polycarbonate. Some of the homonuclear dipolar couplings in polycarbonate are averaged by molecular motion leading to polarization sidebands for several sites at moderate spinning speeds ($\omega_r/2\pi$ = 5.3 kHz for the data shown in Fig. 5.5. Fig. 5.5a shows the profiles for VEFCP (solid dots) and conventional CP (open circles) for the ^{13}C line at 129.5 ppm from TMS, which is a superposition of a quaternary aromatic and a protonated carbon. In this case, the modulations are barely present, though VEFCP seems to perform marginally better. The situation is different, however, in Fig. 5.5b, which shows the intensity of the line at 151 ppm, which is due to a superposition of two quaternary carbons. Here the polarization sidebands are pronounced, and VEFCP results in a much smoother profile. At this contact time (0.52 ms), the rapid kinetics of the ±1 and ±2 sidebands yields higher polarizations for conventional CP, though for longer contact times

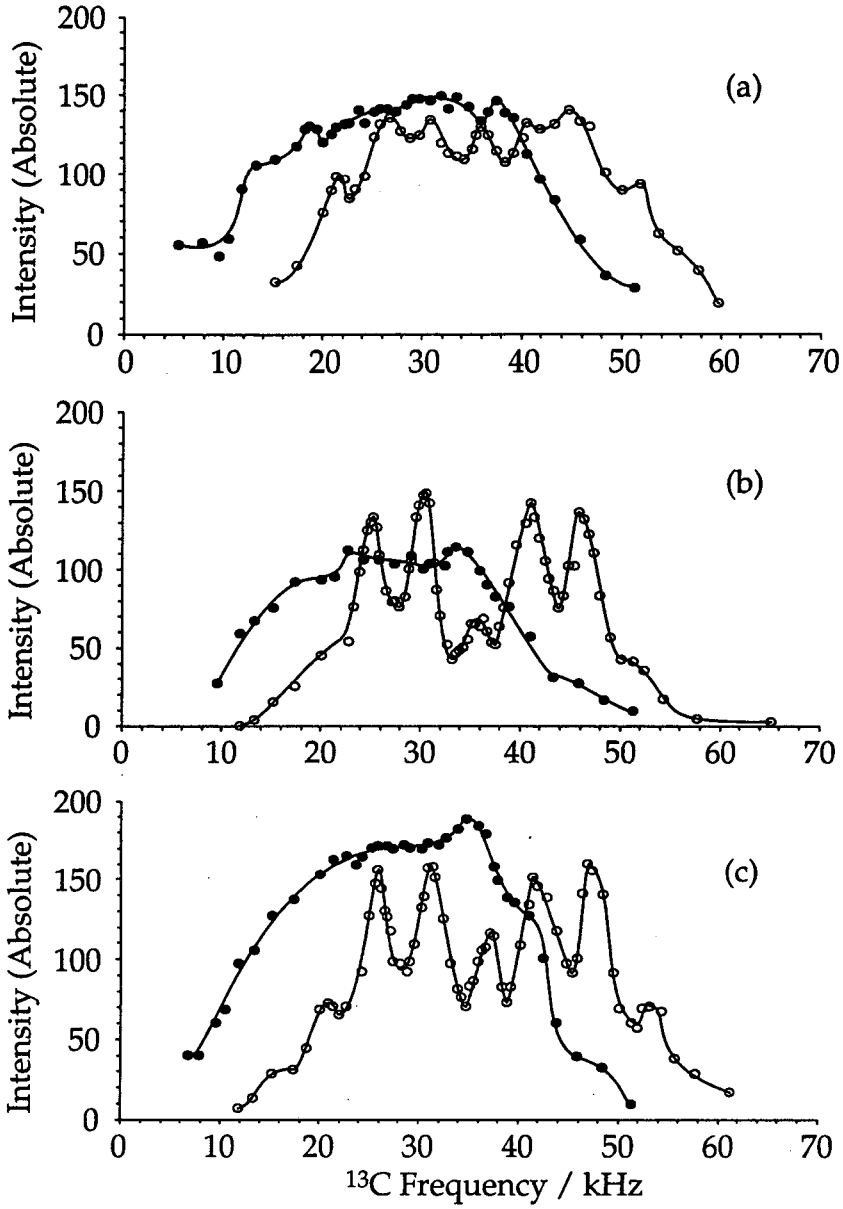

Figure 5.5 Cross-polarized intensity *vs.* ^{13}C rf field for VEFCP (solid circles) and conventional CP (open circles) of polycarbonate spinning at $\omega_r/2\pi$ = 5.3 kHz. The VEFCP experiment used a 26-interval sequence with t_c = 10 μs and scaling factor κ between 0.9 and 0.4 in steps of 0.02. Lines are guides to the eye. (a) The resonance at 129.5 ppm, a superposition of a protonated carbon, with a quaternary carbon with a contact time of 520 μs. (b) The purely quaternary carbon resonance at 151 ppm with a contact time of 520 μs. (c) The same purely quaternary carbon line at 151 ppm but with a contact time of 1.56 ms.

(Fig. 5.5c) VEFCP results in higher polarizations.

Fig. 5.6 shows the increase in signal strengths for VEFCP *vs.* conventional CP for polycarbonate. Note that the VEFCP signal intensities are, for all lines, at least as intense as in the conventional CP spectrum, and some lines are substantially more intense.

A comment should be made as to the performance of VEFCP for a strongly coupled spin system. Though the need for broadband matching would be reduced, there are some samples in which strong and weak couplings coexist. For strong couplings the performance of VEFCP is slightly inferior to that of conventional CP due to two effects. First the effects of all the phase shifts, including switching transients, lead to a 7% reduction in signal intensity after 200 phase shifts for a sample of L-glycine, which is strongly coupled due to the presence of methylene protons. Second, if the matching condition is already broad, VEFCP suffers by containing intervals which may have a very low CP efficiency. On Hartmann-Hahn match, VEFCP with 400 phase shifts yielded, for a sample of L-glycine, intensities of 87% and 81% of the conventional CP intensity for the 8 and 14 interval sequences, respectively.

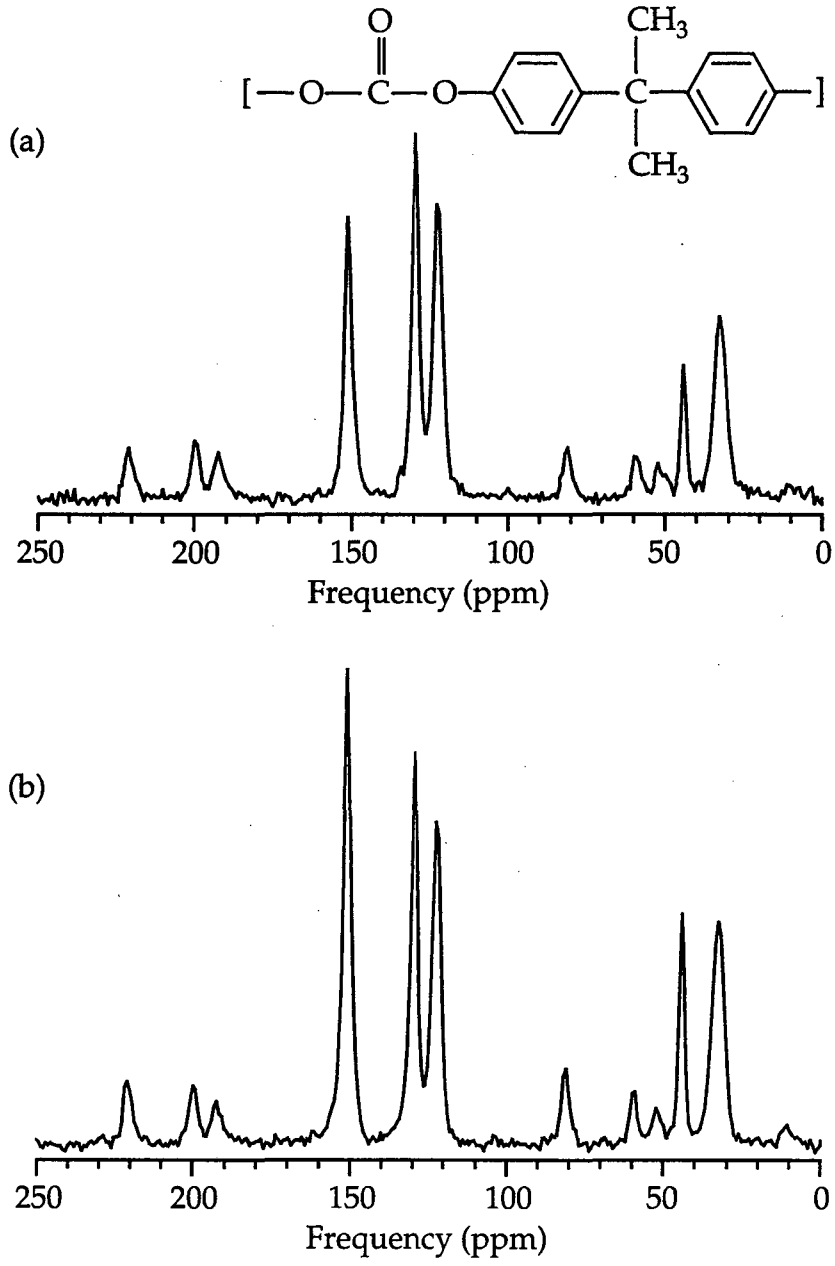

Figure 5.6 CPMAS spectra of polycarbonate with $\omega_r/2\pi$ = 5.3 kHz acquired under (a) conventional CP with a contact time of 1.56 ms and (b) VEFCP with 26 intervals, t_c = 10 ms, a total contact time of 1.56 ms, and scaling factors from 0.9 to 0.4 in steps of 0.02. 64 scans were averaged and 30 Hz line broadening was applied to both FID's before Fourier transformation.

Appendix

A.1 Commutation Rules for Fictitious Spin-1/2 Operators

The commutation rules within a *rs* sub-manifold and between different sub-manifolds are as follows:

$$\left[I_\alpha^{rs}, I_\beta^{rs}\right] = iI_\gamma^{rs} \tag{A.1}$$

$$\left[I_x^{rs}, I_x^{qs}\right] = \left[I_y^{rs}, I_y^{qs}\right] = \frac{i}{2} I_\gamma^{rq} \tag{A.2}$$

$$\left[I_z^{rs}, I_z^{qs}\right] = 0 \tag{A.3}$$

$$\left[I_x^{rs}, I_y^{qs}\right] = \frac{i}{2} I_x^{rq} \tag{A.4}$$

$$\left[I_x^{rs}, I_z^{qs}\right] = -\frac{i}{2} I_y^{rs} \tag{A.5}$$

$$\left[I_y^{rs}, I_z^{qs}\right] = \frac{i}{2} I_x^{rs} \tag{A.6}$$

$$\left[I_\alpha^{rs}, I_\beta^{qt}\right] = 0 \tag{A.7}$$

A.2 Reduced Wigner Rotation Matrices

The reduced Wigner rotation matrices are given by

$$\begin{aligned} d_{m'm}^{(l)}(\theta) = & \sqrt{(l+m)!(l-m)!(l+m')!(l-m')!} \\ & \times \sum_\upsilon \left\{ \frac{(-1)^\upsilon}{(l-m'-\upsilon)!(l+m-\upsilon)!(\upsilon+m'-m)!\upsilon!} \right. \\ & \left. \times \left[\cos\frac{\theta}{2}\right]^{2l+m-m'-2\upsilon} \left[-\sin\frac{\theta}{2}\right]^{m'-m+2\upsilon} \right\} \end{aligned} \tag{A.8}$$

where the sum over υ is performed over all integers for which the factorial are non-negative. Some useful identities involving the reduced rotation matrices are given in Table A.1. The explicit values for $d^{(2)}_{m'm}$ are given in Table A.2

A.3 Matrix Elements of T_{lm}

If the components of T_{lm} given by

Table A.1 Identities involving the reduced Wigner rotation matrices, $d^{(l)}_{m'm}(\theta)$.

$d^{(l)}_{m'm}(\theta) = d^{(l)}_{-m-m'}(\theta) = (-1)^{m'-m} d^{(l)}_{mm'}(\theta) = (-1)^{m'-m} d^{(l)}_{-m'-m}(\theta)$
$d^{(l)}_{m'm}(-\theta) = (-1)^{m'-m} d^{(l)}_{m'm}(\theta) = d^{(l)}_{mm'}(\theta) = \left[d^{(l)}_{m'm}(\theta)\right]^{-1} = \left[d^{(l)}_{m'm}(\theta)\right]^{\dagger}$
$d^{(l)}_{m'm}(0) = \delta_{m'm}$
$d^{(l)}_{m'm}(\pi) = (-1)^{l+m'} \delta_{m'-m}$
$d^{(l)}_{m'm}(-\pi) = (-1)^{l-m'} \delta_{m'-m}$
$d^{(l)}_{m'm}(\pi+\theta) = (-1)^{l+m'} d^{(l)}_{-m'm}(\theta)$
$d^{(l)}_{m'm}(\pi-\theta) = (-1)^{l+m'} d^{(l)}_{m-m'}(\theta)$
$d^{(l)}_{m'm}(2\pi) = (-1)^{2l} \delta_{m'm}$

Table A.2 Second-rank reduced Wigner rotation matrix elements, $d^{(2)}_{nm}(\beta)$.

	m				
n	2	1	0	-1	-2
2	$\left(\frac{1+\cos\beta}{2}\right)^2$	$-\frac{1+\cos\beta}{2}\sin\beta$	$\sqrt{\frac{3}{8}}\sin^2\beta$	$-\frac{1-\cos\beta}{2}\sin\beta$	$\left(\frac{1-\cos\beta}{2}\right)^2$
1	$\frac{1+\cos\beta}{2}\sin\beta$	$\cos^2\beta - \frac{1-\cos\beta}{2}$	$-\sqrt{\frac{3}{8}}\sin 2\beta$	$\frac{1+\cos\beta}{2} - \cos^2\beta$	$-\frac{1-\cos\beta}{2}\sin\beta$
0	$\sqrt{\frac{3}{8}}\sin^2\beta$	$\sqrt{\frac{3}{8}}\sin 2\beta$	$\frac{3\cos^2\beta - 1}{2}$	$-\sqrt{\frac{3}{8}}\sin 2\beta$	$\sqrt{\frac{3}{8}}\sin^2\beta$
1	$\frac{1-\cos\beta}{2}\sin\beta$	$\frac{1+\cos\beta}{2} - \cos^2\beta$	$\sqrt{\frac{3}{8}}\sin 2\beta$	$\cos^2\beta - \frac{1-\cos\beta}{2}$	$-\frac{1+\cos\beta}{2}\sin\beta$
2	$\left(\frac{1-\cos\beta}{2}\right)^2$	$\frac{1-\cos\beta}{2}\sin\beta$	$\sqrt{\frac{3}{8}}\sin^2\beta$	$\frac{1+\cos\beta}{2}\sin\beta$	$\left(\frac{1+\cos\beta}{2}\right)^2$

$$T_{20} = \frac{1}{\sqrt{6}}\left(3I_0^2 - I^2\right), \tag{A.9}$$

$$T_{2\pm1} = \frac{1}{\sqrt{2}}\left(I_0 I_{\pm1} + I_{\pm1} I_0\right), \tag{A.10}$$

and

$$T_{2\pm2} = I_{\pm1}^2, \tag{A.11}$$

the corresponding matrix elements are

$$\left\langle I \pm 1/2 \middle| T_{20} \middle| I \pm 1/2 \right\rangle = \frac{1}{\sqrt{6}}\left(\frac{3}{4} - I(I+1)\right), \tag{A.12}$$

$$\left\langle I \mp 1/2 \middle| T_{2\pm1} \middle| I \pm 1/2 \right\rangle = 0, \tag{A.13}$$

$$\left\langle I \pm 3/2 \middle| T_{2\pm1} \middle| I \pm 1/2 \right\rangle = \sqrt{(I-1/2)(I+3/2)}, \tag{A.14}$$

$$\left\langle I \mp 3/2 \middle| T_{2\pm2} \middle| I \pm 1/2 \right\rangle = \frac{2I+1}{4}\sqrt{(I-1/2)(I+3/2)}, \tag{A.15}$$

and

$$\left\langle I \pm 5/2 \middle| T_{2\pm2} \middle| I \pm 1/2 \right\rangle = \frac{1}{2}\sqrt{(I-1/2)(I-3/2)(I+5/2)}. \tag{A.16}$$

References

[1] R. R. Ernst, G. Bodenhausen, and A. Wokaun, *Principles of Nuclear Magnetic Resonance in One and Two Dimensions* (Clarendon Press, Oxford, England, 1987).

[2] A. Abragam, *Principles of Nuclear Magnetism* (Clarendon Press: Oxford, England, 1961).

[3] T. C. Farrar and E. D. Becker, *Pulse and Fourier Transform NMR: Introduction to Theory and Methods*, 1st ed., (Academic Press: New York, 1971).

[4] M. Mehring, *Principles of High-Resolution NMR in Solids*, 2nd ed., (Springer-Verlag, Berlin, 1976).

[5] C. P. Slichter, *Principles of Magnetic Resonance*, 3rd ed., (Springer-Verlag, Berlin, 1990).

[6] A. Wokaun and R. R. Ernst, *J. Chem. Phys.* **67**, 1752-1758 (1977).

[7] S. Vega and A. Pines, *J. Chem. Phys.* **66**, 5624-5644 (1977).

[8] S. Vega, *J. Chem. Phys.* **68**, 5518-5527 (1978).

[9] M. E. Rose, *Elementary Theory of Angular Momentum* (John Wiley & Sons: New York, 1957).

[10] A. R. Edmonds, *Angular Momentum in Quantum Mechanics* (Princeton University Press, Princeton, NJ, 1960).

[11] R. N. Zare, *Angular Momentum: Understanding Spatial Aspects in Chemistry and Physics* (John Wiley & Sons: New York, 1988).

[12] A. D. Bain, *J. Magn. Reson.* **56**, 418-427 (1984).

[13] G. Bodenhausen, H. Kogler, and R. R. Ernst, *J. Magn. Reson.* **58**, 370-388 (1984).

[14] A. Wokaun and R. R. Ernst, *J. Chem. Phys.* **67**, 1752-1758 (1977).

[15] J. J. Sakurai, *Modern Quantum Mechanics*, (Benjamin/Cummings, Menlo Park, California, 1985).

[16] G. Baym, *Lectures on Quantum Mechanics*, (The Benjamin/Cummings Publishing Company: Menlo Park, California, 1969).

[17] J. J. Sakurai, *Advanced Quantum Mechanics*, 10*th* ed., (Addison-Wesley Publishing Company: Menlo Park, California, 1967).

[18] J. H. Smith, E. M. Purcell, and N. F. Ramsey, *Phys. Rev.* **108**, 120 (1957).

[19] J. H. Van Vleck, *Phys. Rev.* **74**, 1168 (1948).

[20] C. H. Townes and B. P. Dailey, *J. Chem. Phys.* **17**, 782-796 (1949).

[21] C. H. Townes and B. P. Dailey, *J. Chem. Phys.* **20**, 35-40 (1952).

[22] C. H. Townes and B. P. Dailey, *J. Chem. Phys.* **23**, 118-123 (1955).

[23] R. J. Kirkpatrick, *Spectroscopic Methods in Mineralogy and Geology*, F. C. Hawthorne, Ed., (Mineralogical Society of America: Washington, D.C., 1988).

[24] J. A. Tossell and P. Lazzeretti, *Phys. Chem. Miner.* **15**, 564-569 (1988).

[25] E. R. Andrew, A. Bradbury, and R. G. Eades, *Nature* **182**, 1659 (1958).

[26] I. J. Lowe, *Phys. Rev. Lett.* **2**, 285 (1959).

[27] B. F. Chmelka, K. T. Mueller, A. Pines, J. Stebbins, Y. Wu, and J. W. Zwanziger, *Nature* **339**, 42-43 (1989).

[28] K. T. Mueller, Y. Wu, B. F. Chmelka, J. Stebbins, and A. Pines, *J. Am. Chem. Soc.* **113**, 32-38 (1991).

[29] I. Farnan, P. J. Grandinetti, J. H. Baltisberger, J. F. Stebbins, U. Werner, M. A. Eastman, and A. Pines, *Nature* **358**, 31-35 (1992).

[30] K. T. Mueller, J. H. Baltisberger, E. W. Wooten, and A. Pines, *J. Am. Chem. Soc.* **96**, 7001-7004 (1992).

[31] R. E. Youngman and J. W. Zwanziger, *J. Non-Cryst. Solids* **168**, 293-297 (1994).

[32] P. J. Grandinetti, J. H. Baltisberger, I. Farnan, J. F. Stebbins, U. Werner, and A. Pines, *J. Phys. Chem.* **99**, 12341-12348 (1995).

[33] J. H. Baltisberger, S. L. Gann, E. W. Wooten, T. H. Chang, K. T. Mueller, and A. Pines, *J. Am. Chem. Soc.* **114**, 7489-4793 (1992).

[34] A. Samoson, E. Lippmaa, and A. Pines, *Mol. Phys.* **65**, 1013-1018 (1988).

[35] A. Samoson and E. Lippmaa, *J. Magn. Reson.* **84**, 410-416 (1989).

[36] D. J. States, R. A. Haberkorn, and D. J. Ruben, *J. Magn. Reson.* **48**, 286-292 (1982).

[37] G. Drobny, A. Pines, S. Sinton, D. Weitekamp, and D. Wemmer, *Symp. Faraday Soc.* **13**, 49 (1979).

[38] D. Marion and K. Wüthrich, *Biochem. Biophys. Res. Commun.* **113**, 967 (1983).

[39] A. Bax, A. F. Mehlkopf, and J. Smidt, *J. Magn. Reson.* **35**, 373-377 (1979).

[40] K. T. Mueller, B. Q. Sun, G. C. Chingas, J. W. Zwanziger, T. Terao, and A. Pines, *J. Magn. Reson.* **86**, 470-487 (1990).

[41] K. T. Mueller, E. W. Wooten, and A. Pines, *J. Magn. Reson.* **92**, 620-627 (1991).

[42] P. J. Grandinetti, J. H. Baltisberger, A. Llor, Y. K. Lee, U. Werner, M. A. Eastman, and A. Pines, *J. Magn. Reson. A* **103**, 72-81 (1993).

[43] T. Hikita, K. I. Aika, and T. Onishi, *Cat. Lett.* **4**, 157-162 (1990).

[44] K. Aika, N. Fujimoto, M. Kobayashi and E. Iwamatsu, *J. Catal.* **127**, 1-8 (1991).

[45] N. P. Bansal and R. H. Doremus, *Handbook of Glass Properties* (Academic Press: Orlando, Florida, 1986).

[46] M. J. Rosseinsky, A. P. Ramirez, S. H. Glarum, D. W. Murphy, R. C. Haddon, A. F. Hebasrd, T. T. M. Palstra, A. R. Kortan, S. M. Zahurak, and A. V. Makhija, *Phys. Rev. Lett.* **66**, 2830-2832 (1991).

[47] J. T. Cheng, J. C. Edwards, and P. D. Ellis, *J. Phys. Chem.* **94**, 553-561 (1990).

[48] V. T. Deshpande and D. B. Sirdeshmukh, *Acta Cryst.* **14**, 353-355 (1961).

[49] H. Braeken, L. Harang, *Z. Krist.* **75**, 538-549 (1930).

[50] H. W. Smith, Jr. and M. Y. Colby, *Z. Krist.* **103**, 90-95 (1940).

[51] A. G. Nord, *Acta Cryst.* **B30**, 1640-1641 (1974).

[52] M. Shamsuzzoha and B. W. Lucas, *Acta Cryst.* **B38**, 2353-2357 (1982).

[53] C. Dean, T. W. Hambley, and M. R. Snow, *Acta Cryst.* **C40**, 1512-1515 (1984).

[54] K. T. Mueller, G. C. Chingas, and A. Pines, *Rev. Sci. Instrum.* **62**, 1445-1452 (1991).

[55] J. H. Baltisberger, *Advances and Applications of Dynamic-Angle Spinning Nuclear Magnetic Resonance*, PhD. Thesis, (University of California, Berkeley, 1993).

[56] J. H. Baltisberger, S. L. Gann, P. J. Grandinetti, and A. Pines, *Mol. Pys.* **81**, 1109-1124 (1994).

[57] S. L. Segel, *J. Chem. Phys.* **73**, 4146-4147 (1980).

[58] M. M. Maricq and J. S. Waugh, *J. Chem. Phys.* **70**, 3300-3316 (1979).

[59] W. T. Dixon, J. Schaefer, M. D. Sefcik, E. O. Stejskal, and R. A. McKay, *J. Magn. Reson.* **49**, 341-345 (1982).

[60] N. M. Szeverenyi, A. Bax, and G. E. Maciel, *J. Magn. Reson.* **61**, 440-447 (1985).

[61] Z. Gan, *J. Am. Chem. Soc.* **114**, 8307-8309 (1992).

[62] S. L. Gann, J. H. Baltisberger, and A. Pines, *Chem. Phys. Lett.* **210**, 405-410 (1993).

[63] A. Bax, A. F. Mehlkopf, and J. Smidt, *J. Magn. Reson.* **35**, 373-377 (1979).

[64] B. Q. Sun, *Scalar Operators in Solid-State NMR*, PhD. Thesis, (University of California, Berkeley, 1991).

[65] B. Q. Sun, J. H. Baltisberger, Y. Wu, A. Samoson, and A. Pines, *Solid State NMR* **1**, 267-295 (1992).

[66] Y. Wu, B. Q. Sun, and A. Pines, *J. Magn. Reson.* **89**, 297-309 (1990).

[67] Y. Wu, B. F. Chmelka, A. Pines, M. E. Davis, P. J. Grobet, and P. A. Jacobs, *Nature* **346**, 550-552 (1990).

[68] Y. Wu, D. Lewis, J. S. Frye, A. R. Palmer, and R. A. Wind, *J. Magn. Reson.* **100**, 425-430 (1992).

[69] A. Samoson, B. Q. Sun, and A. Pines, In *Pulsed Magnetic Resonance: NMR, ESR and Optics — A Recognition of E.L. Hahn*, D. M. S. Bagguley, Ed. (Clarendon Press: Oxford, 1992).

[70] A. Samoson and J. Tegenfeldt, *J. Magn. Reson. A* **110**, 293-297 (1994).

[71] S. R. Hartmann and E. L. Hahn, *Phys. Rev.* **128**, 2042-2053 (1962).

[72] A. Pines, M. G. Gibby, and J. S. Waugh, *J. Chem. Phys.* **59**, 569-590 (1973).

[73] M. Alla and E. Lippmaa, *Chem. Phys. Lett.* **37**, 260 (1976).

[74] E. F. Rybaczewisky, B. L. Neff, J. S. Waugh, and J. S. Sherfinski, *J. Chem. Phys.* **67**, 1231 (1977).

[75] G. G. Webb and K. W. Zilm, *J. Am. Chem. Soc.* **111**, 1455 (1989).

[76] D. L. VanderHart and G. C. Campbell, *31st Experimental Nuclear Magnetic Resonance Conference*, unpublished (Asilomar, California, 1990).

[77] N. K. Sethi, *J. Magn. Reson.* **94**, 352 (1991).

[78] D. P. Burum and A. Belecki, *J. Magn. Reson.* **95**, 184 (1991).

[79] C. A. Fyfe, H. Grondey, K. T. Mueller, K. C. Wong-Moon, and T. Markus, *J. Am. Chem. Soc.* **114**, 5876-5878 (1992).

[80] X. Wu and K. W. Zilm, *J. Magn. Reson. A* **102**, 205-213 (1993).

[81] E. O. Stejskal, J. Schaefer, and J. S. Waugh, *J. Magn. Reson.* **28**, 105-112 (1977).

[82] A. J. Vega, *J. Magn. Reson.* **96**, 50-68 (1992).

[83] A. J. Vega, *Solid State NMR* **1**, 17-32 (1992).

[84] A. Wokaun and R. R. Ernst, *J. Chem. Phys.* **67**, 1752-1758 (1977).

[85] S. Vega and Y. Naor, *J. Chem. Phys.* **75**, 75-86 (1981).

[86] S. Vega, *Phys. Rev. A* **23**, 3152-3172 (1981).

[87] F. D. Doty, R. R. Inners, and P. D. Ellis, *J. Magn. Reson.* **43**, 399-416 (1981).

[88] F. D. Doty, T. J. Connick, X. Z. Ni, and M. N. Clingan, *J. Magn. Reson.* **77**, 536-549 (1988).

[89] S. L. Gann, J. H. Baltisberger, E. W. Wooten, H. Zimmermann, and A. Pines, *Bull. Magn. Reson.* **16**, 69-72 (1994).

[90] H. J. Simpson, Jr., and R. E. Marsh, *Acta Cryst.* **20**, 550-555 (1966).

[91] M. S. Lehmann, T. F. Koetzle and W. C. Hamilton, *J. Am. Chem. Soc.* **94**, 2657-2660 (1972).

[92] H. Chihara and N. Nakamura, *Nuclear Quadrupolar Resonance Spectroscopy Data*, New Series, Group III, Vol. 20a of *Landolt-Bornstein Numerical Data and Functional Relationships in Science and Technology*, K.-H. Hellwege and A. M. Hellwege (Eds.), O. Madelung (Editor in Chief), (Springer-Verlag: Berlin, 1987).

[93] R. Goc, E. Ponnusamy, J. Tritt-Goc, and D. Fiat, *Int. J. Peptide Protein Res.* **31**, 130-136 (1988).

[94] F. Creuzet, A. McDermott, R. Gebhard, K. VanderHoef, M.B. Spijker-Assink, J. Herzfeld, J. Lugtenburg, M. H. Levitt, and R. G. Griffin, *Science* **251**, 783-786 (1991).

[95] R. G. S. Spencer, K. J. Halverson, M. Auger, A. E. McDermott, R. G. Griffin, and P. T. Lansbury, Jr., *Biochemistry* **30**, 10382-10387 (1991).

[96] O. B. Peersen, S. Yoshimura, H. Hojo, S. Aimoto, and S. O. Smith, *J. Am. Chem. Soc.* **114**, 4332-4335 (1992).

[97] A. C. Kolbert, H. J. M. de Groot, and R. G. Griffin, *J. Magn. Reson.* **85**, 60-68 (1989).

[98] R. C. Zeigler, R. A. Wind, and G. E. Maciel, *J. Magn. Reson.* **79**, 299-306 (1988).

[99] M. Sardashti and G. E. Maciel, *J. Magn. Reson.* **72**, 467-474 (1987).

[100] T. M. Barbara and E. H. Williams, *J. Magn. Reson.* **99**, 439-442 (1992).

[101] X. Wu and K. W. Zilm, *J. Magn. Reson.* **93**, 265-278 (1991).

[102] S. Hediger, B. H. Meier, and R. R. Ernst, *Chem. Phys. Lett.* **213**, 627-635 (1993).

[103] O. B. Peersen, X. L. Wu, I. Kustanovich, and S. O. Smith, *J. Magn. Reson. A* **104**, 334 (1993).

[104] O. B. Peersen, X. L. Wu, and S. O. Smith, *J. Magn. Reson. A* **106**, 127 (1994).

[105] K. Takegoshi and C. A. McDowell, *J. Magn. Reson.* **67**, 356-361 (1986).

[106] A. Bax, *Two-Dimensional NMR in Liquids*, (Delft University Press: Delft, 1984).

Ernest Orlando Lawrence Berkeley National Laboratory
One Cyclotron Road | Berkeley, California 94720

Prepared for the U.S. Department of Energy under Contract No. DE-AC03-76SF00098